

ADVANCES IN THE PERFECTLY MATCHED LAYER
ABSORBING BOUNDARY CONDITION AND A TECHNIQUE
FOR EFFICIENTLY MODELING LONG PATH PROPAGATION
WITH APPLICATIONS TO FINITE-DIFFERENCE GRID
TECHNIQUES

A DISSERTATION
SUBMITTED TO THE DEPARTMENT OF ELECTRICAL
ENGINEERING
AND THE COMMITTEE ON GRADUATE STUDIES
OF STANFORD UNIVERSITY
IN PARTIAL FULFILLMENT OF THE REQUIREMENTS
FOR THE DEGREE OF
DOCTOR OF PHILOSOPHY

Michael William Chevalier

December 2006

© Copyright by Michael William Chevalier 2007
All Rights Reserved

I certify that I have read this dissertation and that, in my opinion, it is fully adequate in scope and quality as a dissertation for the degree of Doctor of Philosophy.

Umran S. Inan Principal Adviser

I certify that I have read this dissertation and that, in my opinion, it is fully adequate in scope and quality as a dissertation for the degree of Doctor of Philosophy.

Timothy F. Bell

I certify that I have read this dissertation and that, in my opinion, it is fully adequate in scope and quality as a dissertation for the degree of Doctor of Philosophy.

Antony Fraser-Smith

Approved for the University Committee on Graduate Studies.

Abstract

The Perfectly Matched Layer (PML) absorbing boundary condition was introduced by Berenger (1993) and Chew and Weedon (1994) as a means for truncating Finite-Difference Time-Domain (FDTD) and Finite-Difference Frequency Domain (FDFD) lattices in order to accurately simulate electromagnetic antenna and scattering problems in isotropic media. In the ionosphere and magnetosphere, where the dominant medium is a magnetized plasma, numerous interesting electromagnetic wave phenomena occur. Many of these would be well suited for analysis by the FDTD and/or FDFD methods, however, until recent developments, including contributions in this dissertation, the PML had not been efficiently extended nor capable, in some cases, to truncate domains containing magnetized plasma. In this dissertation, we develop two methods for extending Chew's formulation to robustly and efficiently truncate any linear magnetized plasma as well as any linear media.

The first PML method developed in this dissertation is a novel approach to the general time domain representation of the Chew and Weedon (1994) PML. This new approach mathematically operates on the spatial field derivatives by convolving them with causal decaying exponential functions. The approach allows the PML update equations to be trivially derived from any set of general linear medium update equations.

The development of the second PML method in this dissertation is motivated by shortcomings of the Perfectly Matched Layer in certain cases involving propagation in anisotropic media, such as whistler-mode propagation in a magnetized plasma, for which the vector component normal to the PML of the group velocity vector and the \mathbf{k} -vector are anti-parallel with each other. This new type of PML utilizes information

on the k -vector direction by applying relevant spatial derivatives to the PML update equations. We demonstrate the numerical stability and performance of the new PML for whistler-mode propagation in a magnetized plasma with respect to the traditional PML.

A method for calculating the numerical reflection coefficient for the PMLs introduced in this dissertation is developed for general linear media. The derived expressions for the numerical reflection coefficient are used to quantify the performance of the PML for incident plane waves at any incident angle, frequency and polarization. Two and three dimensional numerical test results, which validate the calculation of the numerical reflection coefficient, are presented. For the case of the PML truncating free space, values of up to -100 dB for the numerical reflection coefficient are realized. For the case of the PML truncating a magnetized plasma, values from -40 dB up to -90 dB are realized, depending on the orientation of the ambient magnetic field.

Finally, a technique is developed for the efficient modeling of propagation over long paths (hundreds of wavelengths) by breaking the path up into segments and appropriately applying the PML and the total-field/scattered-field method. For FDTD simulations the new technique is well suited to model both slow and fast wave modes as well as scattering inhomogeneities along the path. In addition, the new technique is directly applicable to FDFD simulations. Both FDTD and FDFD numerical simulations of propagation within the Earth-ionosphere waveguide are performed to validate the new technique.

This dissertation is dedicated to my family

Acknowledgements

I am grateful to my adviser, Professor Umran Inan, for giving me the opportunity to study and conduct research as a member of the Very Low Frequency (VLF) Group at Stanford. I appreciate his patience, understanding and encouragement throughout my research career here. As a mentor his level of commitment to research and teaching, as well as his energy, creativity, and enthusiasm are inspirational.

Next, I would like to thank Dr. Timothy Bell, my second research advisor, for his support, encouragement and the many scientific and non-scientific conversations that we've had over the years. I also thank him for being a reader of this dissertation. And to Professor Tony Fraser-Smith for always having an ear to listen and an openness to communicate. I also thank him for being a reader of this dissertation.

I would like to thank Shanhui Fan for agreeing to chair my orals.

I thank Shaolan Min for her administrative help over the years especially during the complicated processing of having two different fellowships/assistanships in one quarter. I also thank her for the great holiday portrait drawings of the STARLab senior members. Thanks also to Helen Nui for administrative assistance.

I thank Martin Walt, for the fun research collaboration we've had in recent years and to Don Carpenter and Bob Helliwell as well.

And huge thank you to all the VLF group members, current and old, for their friendship and collaboration and companionship throughout this journey in graduate school life. To name a few: Bill Peter, Robert Marshall, Ryan Said, Joseph Payne, Robb Moore, Dr. Maria Spasojevic, Dr. Elizabeth Kendall, Dr. Troy Wood, Dr. Jacob Bortnik, Dr. Mehmet Demirkol, etc. etc.

I owe special recognition to Dr. Michael Johnson who was my tour guide on my

visit to check out Stanford. He showed me the labs and the great things VLF group members were doing, drove me up to the Dish in the VLF van (a group having its own van was cool) to check out the Dish and site 522. His contagious enthusiasm helped seal the deal of my joining the group.

I would like to thank my parents and the rest of my family for their support throughout the years, and especially to my brother, Tim, who also being a group member, has made the VLF experience a 'family' experience as well.

Finally, I owe sincere thanks, love, and gratitude to my girlfriend, JoJo, for being loving and supportive this whole time. Thank you.

Michael W Chevalier

Stanford, CA

December 2006

This work in this dissertation was supported, all in part, by a NASA Graduate Student Research Program Fellowship, by the National Science Foundation (NSF) under grant number ATM-9819936-002, support from the Air Force Office of Scientific Research (AFOSR) under grant F49620-03-1-0338, and by the Office of Polar Programs of NSF under grant OPP-0093381-001.

Contents

Abstract	v
	vii
Acknowledgements	viii
1 Introduction	1
1.1 The Finite-Difference Techniques	2
1.2 The Perfectly Matched Layer	4
1.3 Thesis Contributions	6
2 A PML Using a Convolutional Curl Operator	8
2.1 General Frequency Domain PML Equations	9
2.2 First Order CCO-PML	11
2.3 General Nth Order CCO-PML	13
2.4 Error due to the PML in an FDTD grid	16
2.5 Numerical Tests	18
2.5.1 Plane Waves Incident onto the PML from Free Space	22
2.5.2 Plane Waves Incident onto the PML from a Magnetoplasma	25
2.5.3 Waveguide Modes Incident onto the PML	26
3 A PML Utilizing k-Vector Information	28
3.1 Derivation of k-Vector Dependent PML	29
3.2 Numerical Results	35

3.2.1	Free space and free space waveguide	36
3.2.2	Magnetized plasma	38
4	General Numerical Reflection Coefficient	42
4.1	Incident/Scattered Fields at $i=0$ Boundary	43
4.1.1	Incident fields	44
4.1.2	Scattered fields	50
4.2	PML equations and Termination Boundary Conditions	54
4.2.1	$E_x, T + 1$ equations	55
4.2.2	E_y, T equations	55
4.2.3	E_z, T equations	55
4.2.4	H_x, T equations	56
4.2.5	$H_y, T + 1$ equations	56
4.2.6	$H_z, T + 1$ equations	57
4.2.7	$J_x, T+1$ equations	58
4.2.8	J_y, T equations	58
4.2.9	J_z, T equations	59
4.2.10	$\Psi_{Eyt}^{x,m}, \Psi_{Ezt}^{x,m}, \Psi_{Hyt}^{x,m}, \Psi_{Hzt}^{x,m}$ for CCO-PML	59
4.2.11	$\Psi_{Eyt}^x, \Psi_{Ezt}^x, \Psi_{Hyt}^x, \Psi_{Hzt}^x$ for KPML	60
5	Modeling Long Path Propagation	63
5.1	A Segmented Long Path Propagation Technique	65
5.2	Numerical Results and Discussion	67
6	Summary and Suggested Future Work	75
6.1	Summary of PML work	75
6.1.1	Suggested Future Work for PML	76
6.2	Summary of SLP work	77
6.2.1	Future Work for SLP technique	77
A	Finite Difference Equations	78
A.1	Finite-Difference Time Domain equations	78

A.2	Finite-Difference Frequency Domain equations	81
B	Proof of generality of CCO-PML equations	84
B.1	Proof of the delta function	85
C	Some Mathematical Properties of Γ	89
	Bibliography	92

List of Tables

2.1	Numerical values of the CCO-PML coefficient profile, Profile A. . . .	22
-----	---	----

List of Figures

1.1	Transforming from continuous to discrete.	3
1.2	Yee cell	4
1.3	Truncating the space with an absorbing boundary condition	5
2.1	Configuration of the complex stretched coordinate equations	11
2.2	Illustration of plane waves travelling within an FDTD grid	16
2.3	Typical reflection coefficient with design constraints	17
2.4	Orthographic projection representation	19
2.5	Reflection coefficient for free space	23
2.6	Reflection coefficient for magnetoplasma	24
2.7	Reflection coefficient for waveguide	25
3.1	Index of refraction surfaces	31
3.2	Reflection coefficients applying the KPML	36
3.3	Time domain simulations with the KPML	41
4.1	Illustration of plane waves travelling within an FDTD grid	45
5.1	Earth-ionosphere waveguide.	64
5.2	Ionospheric parameters used to model the earth-ionosphere waveguide.	68
5.3	Numerical test 1 results	72
5.4	Numerical test 2 results	73

Chapter 1

Introduction

The application of finite difference grids to model complex radiation and scattering problems in electromagnetics and plasma physics has become increasingly popular due to both the intuitive and robust nature of the technique as well as the ever increasing speed and RAM of computers. The technique itself is very simple. The basic idea is to take a continuous space, e.g., the Earth-ionosphere waveguide of Figure 1.1a, and apply a finite-difference grid, Figure 1.1b, in which the fields and local material properties are sampled at discrete locations on each cell of the grid.

For this dissertation we apply what is known as the Yee cell [Yee (1966)], where the electric fields and electric currents are located on the edges of the cell while the magnetic fields are located on the cell faces as shown in Figure 1.2a. At each field quantity location, the local material properties are specified. Figure 1.2b shows the specific case for the H_z field where the geometric spacing of the Yee cell electric fields yields a natural curl about H_z . One can easily see this is true of all the electric and magnetic fields. Throughout this dissertation the fields are solved for in one of two ways, one of which is to solve for the transient fields as a function of time while the other is to solve for the fields at a single frequency. These two methods are respectively termed the finite-difference time-domain (FDTD) and the finite-difference frequency-domain (FDFD) techniques and are further described in Section 1.1. A key component in any numerical modeling is the boundary condition with which the space is terminated. In this dissertation, we use the so-called Perfectly Matched Layer

(PML) methods, described in Section 1.2 and in later chapters. The contributions of this work are listed in Section 1.3

1.1 The Finite-Difference Techniques

To solve the fields as a function of time, we apply the finite-difference time-domain technique to the electromagnetic Maxwell equations. As an example, we apply it to the \hat{z} -directed Faraday's law

$$\mu_0 \frac{H_{zt} \big|_{i+.5, j+.5, k}^{n+.5} - H_{zt} \big|_{i+.5, j+.5, k}^{n-.5}}{\Delta t} = \frac{E_{xt} \big|_{i+.5, j+1, k}^n - E_{xt} \big|_{i+.5, j, k}^n}{\Delta y} - \frac{E_{yt} \big|_{i+1, j+.5, k}^n - E_{yt} \big|_{i, j+.5, k}^n}{\Delta x} \quad (1.1)$$

where for FDTD the fields are sampled at discrete points in time as well as space. The notation for the fields, taking E_y for example is, $E_{yt} \big|_{i, j+.5, k}^n$, where n is the timestep, and i, j, k is the grid node location. The electric and magnetic fields are sampled half of a timestep, i.e. Δt , apart which yields central-differenced time derivatives about each other. With the Yee cell, the electric and magnetic fields are central-differenced in time and space which results in second-order accuracy. To solve the fields through time, we assume we know the magnetic fields at timestep $n-.5$ and all electric fields at timestep n . For the Hz field, we apply equation (1.1) to yield the Hz field at timestep $n+.5$. This same procedure is then implemented for all magnetic fields throughout the grid using their associated FDTD equation. We then update all the electric fields in the same manner. This technique is known as leapfrogging. When electric currents are present, they are updated with the magnetic fields. More complete descriptions of the FDTD technique are available elsewhere [*Taflov and Hagness (2000)*].

To solve the fields at a single frequency, we apply the finite-difference frequency-domain technique to Maxwell equations. As an example, we apply it to the \hat{z} -directed

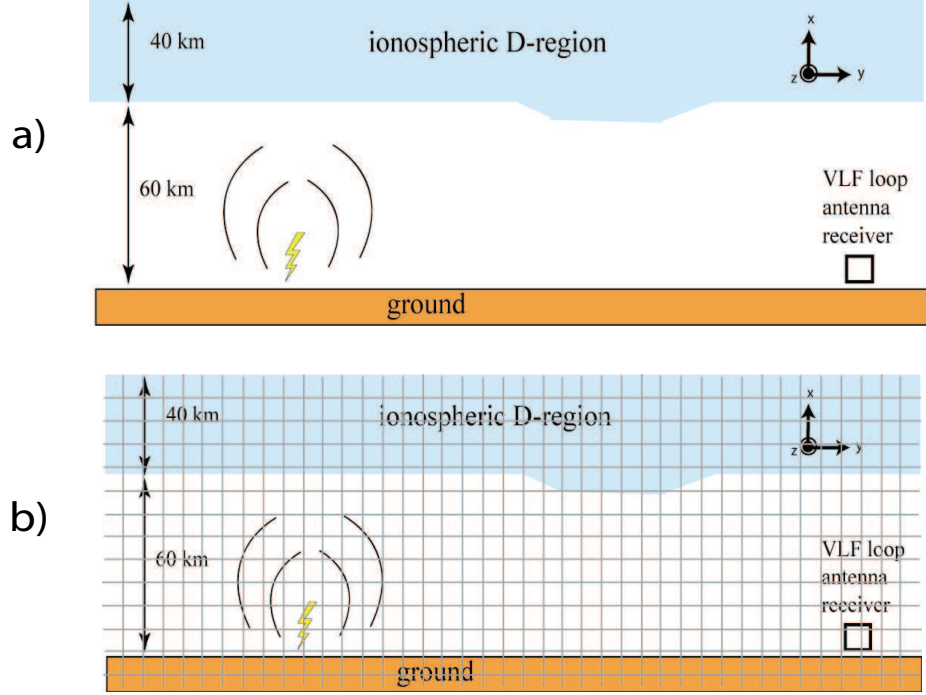


Figure 1.1: a) continuous space of the earth ionosphere waveguide. b) applying a finite difference grid to the space where the fields and material properties are sampled and solved at discrete locations.

Faraday's law

$$j\omega\mu_0 H_{zt} \big|_{i+.5,j+.5,k}^\omega = \frac{E_{xt} \big|_{i+.5,j+1,k}^\omega - E_{xt} \big|_{i+.5,j,k}^\omega}{\Delta y} - \frac{E_{yt} \big|_{i+1,j+.5,k}^\omega - E_{yt} \big|_{i,j+.5,k}^\omega}{\Delta x} \quad (1.2)$$

where the notation for the fields, taking E_y for example is, $E_{yt} \big|_{i,j+.5,k}^\omega$, where ω is the angular frequency, and i, j, k is the grid node location. Unlike FDTD methods, which result in explicit equations, the FDFD equations are all coupled together and all fields throughout the space must be solved together implicitly. As a result, the FDFD method typically requires much more RAM than FDTD. More information on FDFD can be found in *Zhao et al. (2002)*.

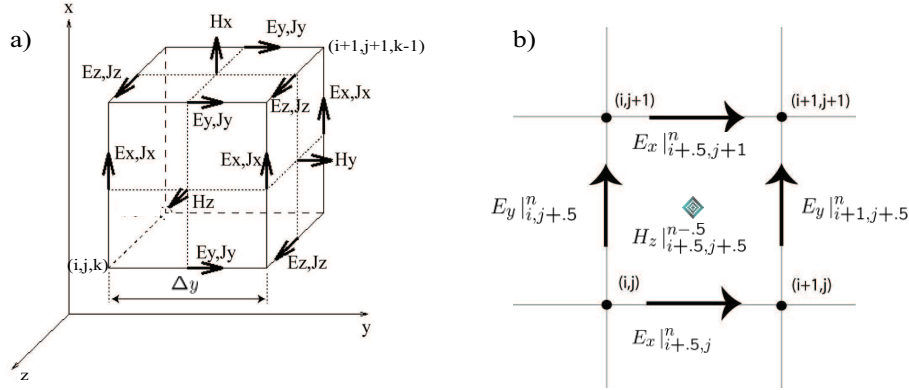


Figure 1.2: a) Yee cell. b) plane of Yee cells depicting the natural geometric curl of the fields.

For a complete list of both the FDTD equations and the FDFD equations used in this dissertation we refer the reader to Appendix A.

1.2 The Perfectly Matched Layer

In many situations the space to be modeled is unbounded in at least one direction. For the case of the Earth-ionosphere waveguide, it is unbounded along the waveguiding direction. Another example is shown in Figure 1.3a where we have an electric dipole antenna in some infinite homogeneous medium. Due to time and memory constraints we must truncate our space such that we solve the fields in the particular region of interest, i.e., within the dashed box. In figure 1.3b we place a special material of finite thickness surrounding the dashed box region. Theoretically, any incident waves, evanescent or propagating, on this material are absorbed by the material such that the fields in the spaces inside the dashed box are identical for both the infinite space and the truncated space. This special material is known as the Perfectly Matched Layer (PML) and was introduced to the computational electromagnetics community by *Berenger* (1994) and *Chew and Weedon* (1994). In practice, however, for both FDTD and FDFD the PML can reflect some waves back into the space depending on the the types of waves incident. Since both the capabilities and optimization

of the PML as well as the introduction of new forms of it, are central topics of this dissertation, the PML is further described and discussed in great detail in the chapters that follow.

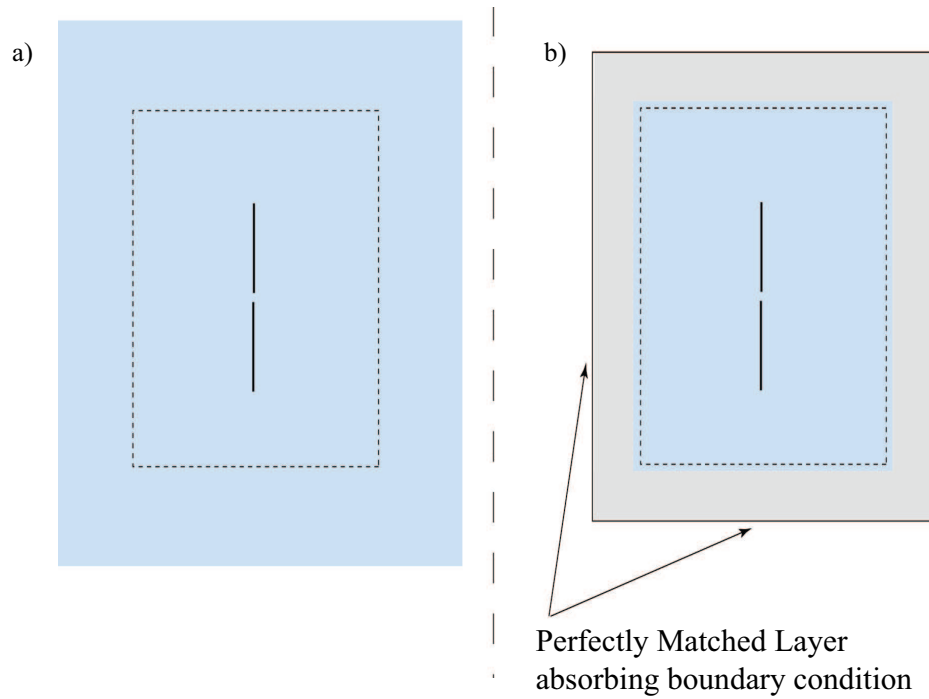


Figure 1.3: a) Infinite domain. b) truncated domain with absorbing boundary condition.

1.3 Thesis Contributions

One of the important limitations of both the FDTD and FDFD techniques is the requirement to retain information about all of the field quantities at all grid points. This requirement significantly limits their applicability involving long distance (many hundreds of wavelengths) propagation. In this dissertation we develop a new Segmented-Long-Path (SLP) method which facilitates the use of finite-difference methods for long propagation paths. This method is described in Chapter 5.

Another important limitation of the FDTD and FDFD techniques is the need to efficiently truncate the numerical space so as to avoid unwanted reflections from its edges. In this dissertation we develop and introduce two new methodologies for application of the so-called Perfectly Matched Layer absorbing boundary condition for general linear and anisotropic media. These contributions are discussed in Chapters 2, 3, and 4.

The original contributions of this thesis are as follows

1. Introduction of a general time domain representation of the Chew and Weedon [1994] stretched coordinate Perfectly Matched Layer (PML) absorbing boundary condition is described. This new approach mathematically operates on the spatial field derivatives and allows the PML update equations to be trivially derived from any set of general linear medium update equations. The method provides a more robust method for reducing the error of the PML over a desired frequency range. The results were published in *Chevalier and Inan* (2004)
2. Development of a new type of PML that utilizes information on the k-vector direction by applying relevant spatial derivatives to the PML update equations. This new PML, deemed the KPML, allows the decay of single frequency whistler mode waves within the PML for which the vector component normal to the PML of the group velocity vector and the k-vector can be parallel or anti-parallel, depending on the incidence angle. All other PML's used prior to the KPML would instead amplify these types of waves and render the simulation unstable. The KPML is described in a paper by *Chevalier et al.* (2006)

3. Development of an analytical method for the calculation of the numerical reflection coefficient for all the PMLs described in this thesis. The method is suitable for any incident wave, propagating or evanescent. The majority of these results are presented in *Chevalier and Inan (2004)* and *Chevalier et al. (2006)*.
4. Development of a new technique for efficient modeling of propagation over long paths (hundreds of λ) by breaking the path up into segments and appropriately applying the Perfectly Matched Layer absorbing boundary condition and the total field/scattered field boundary condition. The technique is applicable to both FDTD and FDFD, and is described in *Chevalier and Inan (2007)*.

Chapter 2

A PML Using a Convolutional Curl Operator

The introduction of the Perfectly Matched Layer (PML) by *Berenger* (1994) and *Chew and Weedon* (1994) has revolutionized the absorbing boundary condition for the finite-difference time-domain (FDTD) technique as well as for other methods of numerical electromagnetic modeling. Although both approaches were originally derived to truncate domains of lossless dielectric media, there has since been efforts by other researchers to advance the PML to truncate domains of general linear media, including linear anisotropic media. These advancements include the approach by *Gedney* (1996), the uniaxial PML, which is Maxwellian and which does not require the field splitting technique employed by *Berenger* (1994) and *Chew and Weedon* (1994), and which has been derived to match linear isotropic media. *Fang* (1995) describes the Generalized Perfectly Matched Layer to match lossy isotropic media, using the field splitting technique. Finally, *Teixeira* (1998) recognizes that the methods of *Berenger* (1994) and *Chew and Weedon* (1994) are applicable to general linear media, including anisotropic media, while continuing to employ the field splitting technique. In this chapter we build upon and extend this past work starting from *Teixeira* (1998).

Section 2.2 represents the contents of *Chevalier* (1999), a presentation given at the URSI conference in Boulder, CO in 1999. We reference *Roden and Gedney* (2000) which involved the CPML (convolutional PML), a method similar to that presented

here (both apply the recursive convolution technique) and whose work was also carried out during an overlapping time period. In Section 2.3 we mathematically compare the CPML of *Roden and Gedney* (2000) with the PML presented in *Chevalier and Inan* (2004) to show that the latter has a more general form. *Gedney* (1996) applied the CPML technique to establish an unconditionally stable ADI-FDTD method. Since the introduction of the CPML, there have been other unsplit time domain formulations developed. For example, *Ramadan and Oztoprak* (2002) used the unsplit formulation to derive a time domain formulation using DSP techniques.

2.1 General Frequency Domain PML Equations

We express the *Chew and Weedon* (1994) equations in a different form, which is more easily adapted to the time domain PML technique introduced here. We start with the general 3D PML equations

$$\begin{aligned} \nabla_{\text{PML}} = & \frac{1}{1 + g_x(j\omega)} \frac{\partial}{\partial x} \hat{a}_x + \frac{1}{1 + g_y(j\omega)} \frac{\partial}{\partial y} \hat{a}_y \\ & + \frac{1}{1 + g_z(j\omega)} \frac{\partial}{\partial z} \hat{a}_z \end{aligned} \quad (2.1a)$$

$$\nabla_{\text{PML}} \times \vec{H} = j\omega\epsilon \vec{E} + \vec{J} \quad (2.1b)$$

$$\nabla_{\text{PML}} \times \vec{E} = -j\omega\mu_0 \vec{H} \quad (2.1c)$$

$$\vec{J} = \sigma \vec{E} \quad (2.1d)$$

where $g_x(j\omega), g_y(j\omega), g_z(j\omega)$ are complex, frequency dependent functions. The form of the plane wave solution for the field quantities described by (2.1a)-(2.1d) is written:

$$e^{-jk[x \sin(\theta) \cos(\phi) + y \sin(\theta) \sin(\phi) + z \cos(\theta)]} e^{-jk[g_x(j\omega)x \sin(\theta) \cos(\phi) + g_y(j\omega)y \sin(\theta) \sin(\phi) + g_z(j\omega)z \cos(\theta)]}$$

where ε is isotropic permittivity, μ_0 is the free space permeability, σ is the conductivity and can be a tensor, and k is the wavenumber which can be a function of both ω , θ and ϕ . We define ω as the radial frequency. θ is the angle with respect to the z-axis, and ϕ is the azimuthal angle in the xy plane with respect to the x-axis. These are the typical representation of the spherical coordinate angles. The form of the solution can be verified by direct substitution into the equations. Maxwell's equations and their traditional plane wave solution can be obtained from (2.1a)-(2.1d) by setting $g_x(j\omega) = g_y(j\omega) = g_z(j\omega) = 0$. The plane wave solution of the PML is the same as that of Maxwell equations except that it is multiplied by a second exponential function, which represents the adjustable dissipation of the PML and which can in general be a complex and frequency-dependent function. The various impedance relationships inherent in (2.1a)-(2.1d), i.e., the ratio of electric and magnetic field quantities such as, E_x/H_y , can easily be shown to be identical to those obtained from Maxwell's Equations. Figure 2.1 illustrates in 2D the necessary mathematical relationships of $g_x(j\omega)$ and $g_y(j\omega)$ within the FDTD space in order to realize the Perfectly Matched Layer conditions, i.e., the condition of no reflection for an incident plane wave (at any angle) on any of the PML interfaces. The extension to 3D follows the same type of relationships. We refer the reader to [Berenger (1994); Chew and Weedon (1994)] for a rigorous derivation of the necessary conditions for zero reflection at the PML interface.

We can rewrite the ∇_{PML} operator as

$$\begin{aligned} \nabla_{\text{PML}} = & \left[\frac{\partial}{\partial x} - \frac{g_x(j\omega)}{1 + g_x(j\omega)} \frac{\partial}{\partial x} \right] \hat{a}_x + \left[\frac{\partial}{\partial y} - \frac{g_y(j\omega)}{1 + g_y(j\omega)} \frac{\partial}{\partial y} \right] \hat{a}_y \\ & + \left[\frac{\partial}{\partial z} - \frac{g_z(j\omega)}{1 + g_z(j\omega)} \frac{\partial}{\partial z} \right] \hat{a}_z \end{aligned} \quad (2.2)$$

a form which allows the PML to be implemented without the need for the field splitting technique.

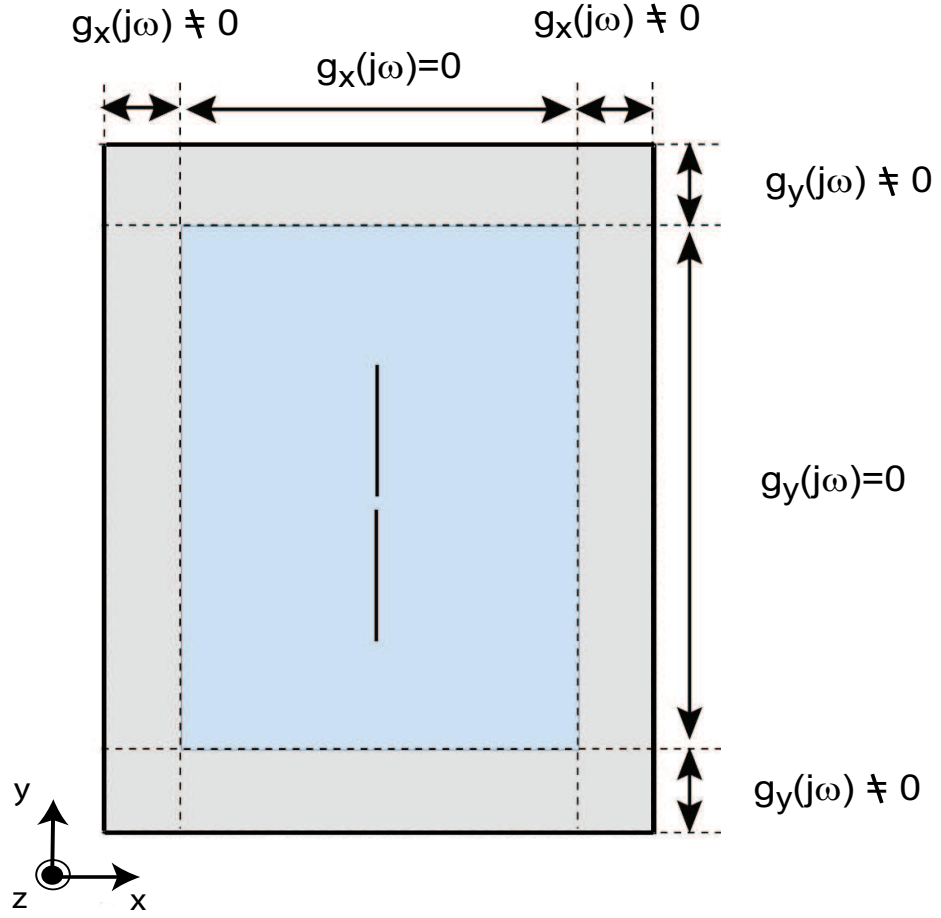


Figure 2.1: Configuration of the complex stretched coordinate equations to ensure a Perfectly Matched Layer.

2.2 First Order CCO-PML

If we let $g_x(j\omega) = \alpha_x/j\omega$, $g_y(j\omega) = \alpha_y/j\omega$, and $g_z(j\omega) = \alpha_z/j\omega$, where α_x , α_y , and α_z are positive real constants, the time domain ∇_{PML} operator becomes:

$$\begin{aligned} \nabla_{\text{PML}} = & \left[\frac{\partial}{\partial x} - u(t)\alpha_x e^{-\alpha_x t} * \frac{\partial}{\partial x} \right] \hat{a}_x + \left[\frac{\partial}{\partial y} - u(t)\alpha_y e^{-\alpha_y t} * \frac{\partial}{\partial y} \right] \hat{a}_y \\ & + \left[\frac{\partial}{\partial z} - u(t)\alpha_z e^{-\alpha_z t} * \frac{\partial}{\partial z} \right] \hat{a}_z \end{aligned} \quad (2.3)$$

where "\$*\$" represents convolution and $u(t)$ is the unit step function. This form of the PML has a temporal/spatial operation which involves a convolution between a decaying (in time) exponential and the function that the spatial derivative operates on. It is hereafter referred to as the 1st order CCO-PML (convolutional curl operation PML) or sometimes just as CCO-PML. Mathematically, the 1st order CCO-PML yields the same solutions as the final time domain representations of *Berenger* (1994) and *Chew and Weedon* (1994). In the form represented by (2.3), the 1st order CCO-PML trivially matches any general linear medium, including anisotropic media. Invoking linearity we can arrange the CCO-PML equations which apply (2.3) into

$$[\nabla_{\text{PML}} - \nabla] \times \vec{H} + \nabla \times \vec{H} = \frac{\partial \varepsilon * \vec{E}}{\partial t} + \vec{J} \quad (2.4a)$$

$$[\nabla_{\text{PML}} - \nabla] \times \vec{E} + \nabla \times \vec{E} = -\mu_0 \frac{\partial \vec{H}}{\partial t} \quad (2.4b)$$

where

$$\begin{aligned} [\nabla_{\text{PML}} - \nabla] \times \vec{H} = & \\ & - \left[u(t) \alpha_y e^{-\alpha_y t} * \frac{\partial H_z}{\partial y} - u(t) \alpha_z e^{-\alpha_z t} * \frac{\partial H_y}{\partial z} \right] \hat{a}_x \\ & - \left[u(t) \alpha_z e^{-\alpha_z t} * \frac{\partial H_x}{\partial z} - u(t) \alpha_x e^{-\alpha_x t} * \frac{\partial H_z}{\partial x} \right] \hat{a}_y \\ & - \left[u(t) \alpha_x e^{-\alpha_x t} * \frac{\partial H_y}{\partial x} - u(t) \alpha_y e^{-\alpha_y t} * \frac{\partial H_x}{\partial y} \right] \hat{a}_z \end{aligned} \quad (2.5)$$

and the corresponding curl of the electric field, i.e., $[\nabla_{\text{PML}} - \nabla] \times \vec{E}$, has the same form as above and can be obtained simply by replacing \vec{H} 's with \vec{E} 's. The Maxwell update equations and the CCO-PML update equations are identical except for the extra convolution terms included in the CCO-PML updates. The convolutions can be efficiently calculated using the piecewise linear recursive convolution technique

of *Kelley and Luebbers (1996)*. The memory requirements are larger for the CCO-PML update equations relative to Maxwell's update equations, since at the location of each field component up to 2 convolution sums must be stored. Nevertheless, detailed analysis indicates that the memory requirements are similar to those for the free space PML derived in *Berenger (1994)*. It should further be noted the number of extra variables needed to implement the 1st order CCO-PML does not depend on the complexity of the medium.

2.3 General Nth Order CCO-PML

For complicated dispersive media such as magnetized plasmas the optimized 1st order CCO-PML for a given thickness T may not achieve the desired reflection coefficient over the frequency range of interest. We may, therefore, try to improve the performance of the CCO-PML by including more convolutional terms. We can assume

$$\frac{1}{1 + g_x(j\omega)} = 1 - \sum_{n=1}^N \frac{b_{xn}\alpha_{xn}}{j\omega + \alpha_{xn}} \quad (2.6)$$

with $[1 + g_y(j\omega)]^{-1}$ and $[1 + g_z(j\omega)]^{-1}$ also having the same forms. In this case the frequency domain ∇_{PML} operator becomes

$$\begin{aligned} \nabla_{\text{PML}} = & \left[\frac{\partial}{\partial x} - \left(\sum_{n=1}^N \frac{b_{xn}\alpha_{xn}}{j\omega + \alpha_{xn}} \right) \frac{\partial}{\partial x} \right] \hat{a}_x + \left[\frac{\partial}{\partial y} - \left(\sum_{n=1}^N \frac{b_{yn}\alpha_{yn}}{j\omega + \alpha_{yn}} \right) \frac{\partial}{\partial y} \right] \hat{a}_y \\ & + \left[\frac{\partial}{\partial z} - \left(\sum_{n=1}^N \frac{b_{zn}\alpha_{zn}}{j\omega + \alpha_{zn}} \right) \frac{\partial}{\partial z} \right] \hat{a}_z \end{aligned} \quad (2.7)$$

It can be easily shown that with this higher order ∇_{PML} operator the PML character of the equation is still mathematically preserved. The time domain $[\nabla_{\text{PML}} - \nabla] \times \vec{H}$ then becomes

$$[\nabla_{\text{PML}} - \nabla] \times \vec{H} =$$

$$\begin{aligned}
& - \left\{ \text{Re} \left\{ \sum_{n=1}^N u(t) b_{yn} \alpha_{yn} e^{-\alpha_{yn} t} \right\} * \frac{\partial H_z}{\partial y} - \text{Re} \left\{ \sum_{n=1}^N u(t) b_{zn} \alpha_{zn} e^{-\alpha_{zn} t} \right\} * \frac{\partial H_y}{\partial z} \right\} \hat{a}_x \\
& - \left\{ \text{Re} \left\{ \sum_{n=1}^N u(t) b_{zn} \alpha_{zn} e^{-\alpha_{zn} t} \right\} * \frac{\partial H_x}{\partial z} - \text{Re} \left\{ \sum_{n=1}^N u(t) b_{xn} \alpha_{xn} e^{-\alpha_{xn} t} \right\} * \frac{\partial H_z}{\partial x} \right\} \hat{a}_y \\
& - \left\{ \text{Re} \left\{ \sum_{n=1}^N u(t) b_{xn} \alpha_{xn} e^{-\alpha_{xn} t} \right\} * \frac{\partial H_y}{\partial x} - \text{Re} \left\{ \sum_{n=1}^N u(t) b_{yn} \alpha_{yn} e^{-\alpha_{yn} t} \right\} * \frac{\partial H_x}{\partial y} \right\} \hat{a}_z
\end{aligned} \tag{2.8}$$

where $b_{xn}(i)$ and $\alpha_{xn}(i)$, also known as the CCO-PML coefficients, can be complex. For complex coefficients we take the real part of the convolution, e.g.,

$$\text{Re} \left\{ u(t) b_{x1} \alpha_{x1} e^{-\alpha_{x1} t} \right\} * \frac{\partial H_z}{\partial x} = \frac{1}{2} \left\{ u(t) b_{x1} \alpha_{x1} e^{-\alpha_{x1} t} + u(t) b_{x1}^* \alpha_{x1}^* e^{-\alpha_{x1}^* t} \right\} * \frac{\partial H_z}{\partial x} \tag{2.9}$$

because the functions that are convolved with the fields must be real. We will apply complex convolutions in Section 2.5. Also note that complex convolutions require twice as much memory, so that if memory is a limitation then real valued coefficients should be used. Note that $[\nabla_{\text{PML}} - \nabla] \times \vec{E}$ has the same form as (2.8); obtained by replacing the \vec{H} 's with \vec{E} 's. The equations for the Nth order CCO-PML are no more difficult to solve than those for the 1st order CCO-PML, except that N times as many convolutions are involved, all of which can be readily computed with the piecewise linear recursive convolution technique of *Kelley and Luebbers* (1996).

One question arises in this context: Why not double the thickness of the PML instead of including extra convolutional terms? By doubling the thickness we increase, within the PML, the computational time and the number of variables by a factor of 2. In most of the PML region we have attenuation in only one direction, except at the corners. Recognizing that such is the case and for a free space grid, if we increase the number of convolutional terms to, say N=2, it can easily be shown that, within the PML, the computational time and the number of extra update variables increase by a factor of 1.4. For N=3, this increase factor is 1.8, still less than 2. The saving would be even greater for grids containing more complex materials where prior values of the fields need to be saved, such as Lorentz or Debye materials.

To demonstrate the generality of the CCO-PML scheme we derive the standard form given in *Roden and Gedney (2000)* from a second order ($N=2$) CCO-PML. We direct our analysis at the term

$$\frac{\partial H_z}{\partial x} - Re \left[\sum_{n=1}^N u(t) b_{xn} \alpha_{xn} e^{-\alpha_{xn} t} \right] * \frac{\partial H_z}{\partial x} \quad (2.10)$$

whose results are easily generalized. Knowing that

$$\frac{\partial H_z}{\partial x} = \delta(t) * \frac{\partial H_z}{\partial x} \quad (2.11)$$

and substituting (2.11) into (2.10) we get

$$\left[\delta(t) - u(t) b_{x1} \alpha_{x1} e^{-\alpha_{x1} t} - u(t) b_{x2} \alpha_{x2} e^{-\alpha_{x2} t} \right] * \frac{\partial H_z}{\partial x} \quad (2.12)$$

It is easily shown that in the limit as $\alpha_{x1} \rightarrow \infty$ we obtain

$$u(t) \alpha_{x1} e^{-\alpha_{x1} t} = \delta(t) \quad (2.13)$$

i.e., the delta function. We refer the reader to Appendix B for the proof both in the continuous domain and for finite difference equations. We then find

$$\left[(1 - b_{x1}) \delta(t) + u(t) b_{x2} \alpha_{x2} e^{-\alpha_{x2} t} \right] * \frac{\partial H_z}{\partial x} \quad (2.14)$$

has the same form as equation (5) from *Roden and Gedney (2000)*, where for equality

$$(1 - b_{x1}) = \frac{1}{k_i} \quad (2.15)$$

$$b_{x2} \alpha_{x2} = \frac{\sigma_i}{k_i^2 \varepsilon_0} \quad (2.16)$$

$$\alpha_{x2} = \frac{\sigma_i}{k_i \varepsilon_0} + \frac{\alpha_i}{\varepsilon_0} \quad (2.17)$$

where $[b_{x1}, b_{x2}, \alpha_{x2}]$ represent three independent parameters of the CCO-PML while

$[k_i, \sigma_i, \alpha_i]$ represent three independent parameters of equation (5) of *Roden and Gedney* (2000).

2.4 Error due to the PML in an FDTD grid

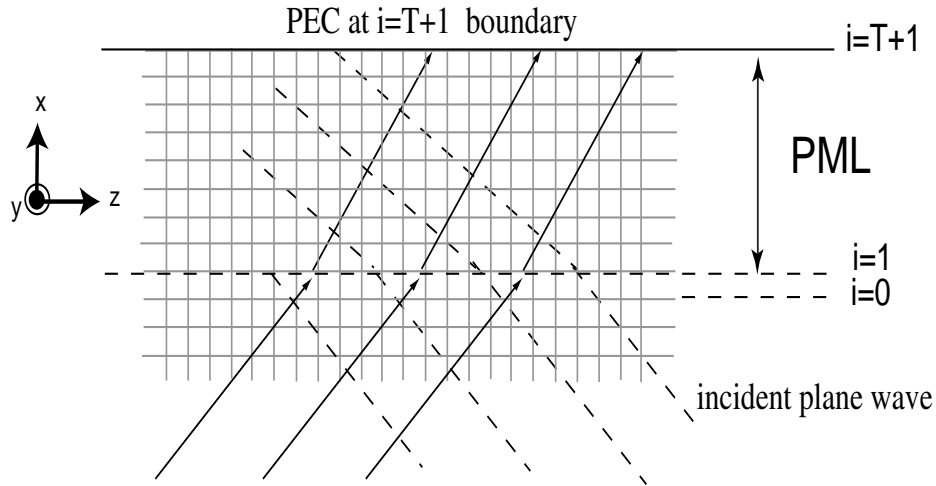


Figure 2.2: Illustration of plane waves travelling within an FDTD grid of a semi-infinite grid of a homogenous medium with a matching PML. Scattered fields are present but are not explicitly shown.

In Chapter 4 a method is developed for calculating the numerical reflection coefficient for a plane wave, in a general linear medium, incident onto an Nth order CCO-PML for a given set of PML coefficients and for a given PML cell thickness T . The calculation procedure is illustrated in Figure 2.2. The incident plane wave is written out in general as a function of incident angle (including complex angles), frequency, and polarization (important for anisotropic media). The reflection coefficient calculation quantifies the time-harmonic scattered plane wave fields, i.e., the error due to the imperfections of the PML. The motivation for this calculation is to quantitatively determine the efficiency of the PML method. The method is quite general, since any general electromagnetic field can be described by a linear superposition of both evanescent and propagating plane waves over incident angle and frequency, so that the PML efficiency for specific types of wave structures can be inferred from

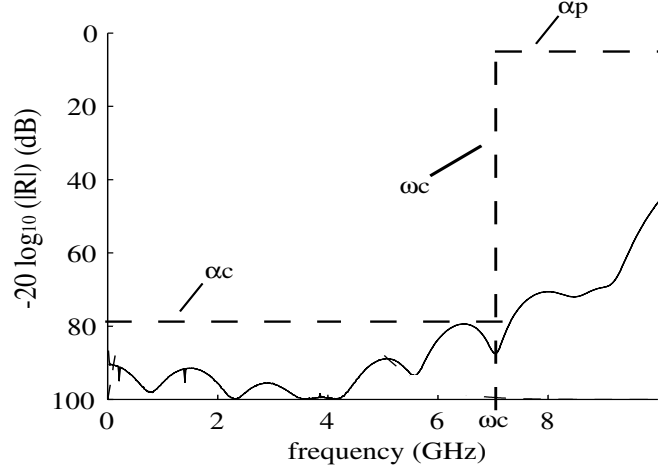


Figure 2.3: Typical reflection coefficient with design constraints.

the plane wave results. The numerical results presented in this Chapter apply this numerical reflection coefficient method developed in Chapter 4.

The method described in Chapter 4 allows one to solve for all fields within the space defined. Moreover we can calculate three important quantities; $H_{xs}|_{i=0,j_0+.5,k_0+.5}^{n+.5,\omega}$, $H_{ys}|_{i=.5,j_0,k_0+.5}^{n+.5,\omega}$ and $H_{zs}|_{i=.5,j=j_0+.5,k_0}^{n+.5,\omega}$, namely the reflected fields just outside the PML. We define the collocated incident fields as: $H_{xi}|_{i=0,j_0+.5,k_0+.5}^{n+.5,\omega}$, $H_{yi}|_{i=.5,j_0,k_0+.5}^{n+.5,\omega}$ and $H_{zi}|_{i=.5,j=j_0+.5,k_0}^{n+.5,\omega}$, and the normalized error as

$$\|R(\omega, \theta, \phi)\|_2 = \sqrt{\frac{|H_{xs}|_{i=0,j_0+.5,k_0+.5}^{n+.5,\omega}|^2 + |H_{ys}|_{i=.5,j_0,k_0+.5}^{n+.5,\omega}|^2 + |H_{zs}|_{i=.5,j=j_0+.5,k_0}^{n+.5,\omega}|^2}{|H_{xi}|_{i=0,j_0+.5,k_0+.5}^{n+.5,\omega}|^2 + |H_{yi}|_{i=.5,j_0,k_0+.5}^{n+.5,\omega}|^2 + |H_{zi}|_{i=.5,j=j_0+.5,k_0}^{n+.5,\omega}|^2}} \quad (2.18)$$

which is simply the normalized Euclidean norm of the scattered magnetic field due to the PML, i.e., the magnitude of the numerical reflection coefficient. For ease of presentation we refer to $\|R(\omega, \theta, \phi)\|_2$ as the numerical reflection coefficient due to the PML for a given frequency and angle of incidence. We can therefore adjust the CCO-PML coefficients, $b_{xn}(i)$ and $\alpha_{xn}(i)$ until $\|R(\omega, \theta, \phi)\|_2$ is minimized over the

frequencies and incident angles of interest. Figure 2.3 displays a plot of $\|R(\omega, \theta, \phi)\|_2$ versus frequency, for a wave in free space incident onto the PML at 30 degrees, i.e. $\theta = \pi/2, \phi = \pi/6$. We can improve $\|R(\omega, \theta, \phi)\|_2$ by setting a band of minimum reflection, $0 < \omega < \omega_c$. We would require $\|R(\omega, \theta, \phi)\|_2 < \alpha_c$ for $0 < \omega < \omega_c$. Or we could require $\overline{\|R(\omega, \theta, \phi)\|_2} < \alpha_c$ for $0 < \omega < \omega_c$, which is the average reflection coefficient. Another requirement would be to have $\|R(\omega, \theta, \phi)\|_2 < \alpha_p = 1.0$ for $\omega > \omega_c$. This condition forces the boundary condition to be stable over all frequencies. We would minimize α_c for a given ω_c by iteratively adjusting the CCO-PML coefficients, given an initial starting value for the coefficients, until α_c reaches a minimum. In most cases we would minimize over a range of incident angles as well. This is the procedure used in this chapter for improving the PML to match particular media, the results of which are presented in the numerical results of section 2.5.

2.5 Numerical Tests

In this section we present numerical results obtained by the application of the frequency domain numerical reflection coefficient calculation derived in Chapter 4 to specific types of media matched by the CCO-PML. To validate the reflection coefficient method, we also calculate the reflection coefficient from time domain simulations of the plane wave incident problem as shown in Figure 2.2, by selecting a portion of the space as illustrated in Figure 2.4a. This selected portion is an FDTD grid, displayed as an orthographic projection representation in Figures 2.4b, 2.4c and 2.4d. The grid is a $3 \times 3 \times (T + 1)$ cell space where the center front cell represents the $(i = 0, j = j_0, k = k_0)$ cell, where our choice of j_0 and k_0 is arbitrary. Note that we could have used any $M \times N \times (T + 1)$ cell space, where $M, N > 2$. In order for the fields within the FDTD grid to represent an incident plane wave being scattered from the PML, we must properly specify the grid's surface boundary fields over time, at the boundaries indicated by the bold black line segments. The method for calculating the numerical reflection coefficient discussed in Chapter 4 also allows us to calculate *all* fields within the PML, and within the entire space of Figure 2.2 for that matter, as a function of frequency, incident angle, and the input incident fields. In other words,

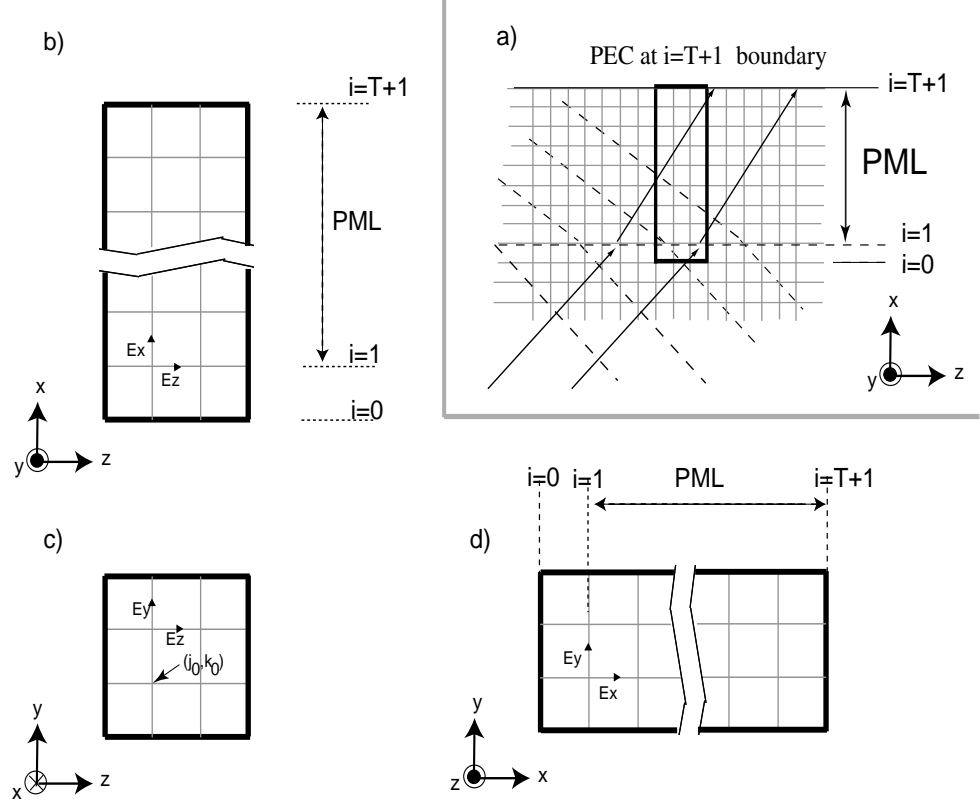


Figure 2.4: Orthographic projection representation of the $3 \times 3 \times (T + 1)$ cell FDTD space used to calculate the PML reflection coefficient in the time domain numerical experiments.

we know the quantities $E_{xt}|_{i+.5, j_0, k_0}^{n=0, \omega}$, $E_{yt}|_{i, j_0+.5, k_0}^{n=0, \omega}$, and $E_{zt}|_{i, j_0, k_0+.5}^{n=0, \omega}$ for $i = 0$ through $i = T + 1$. For a given angle of incidence, we apply the plane wave relations in the y and z directions

$$\widetilde{E}_{xt}|_{i+.5, j_0+m, k_0+p}^{\omega} = E_{xt}|_{i+.5, j_0, k_0}^{n=0, \omega} e^{-j(k_y m \Delta y + k_z p \Delta z)} \quad (2.19)$$

$$\widetilde{E}_{yt}|_{i, j_0+.5+m, k_0+p}^{\omega} = E_{yt}|_{i, j_0+.5, k_0}^{n=0, \omega} e^{-j(k_y m \Delta y + k_z p \Delta z)} \quad (2.20)$$

$$\widetilde{E}_{zt}|_{i, j_0+m, k_0+.5+p}^{\omega} = E_{zt}|_{i, j_0, k_0+.5}^{n=0, \omega} e^{-j(k_y m \Delta y + k_z p \Delta z)} \quad (2.21)$$

to calculate the grid surface boundary fields as a function of frequency, where m and p are integers whose allowed values correspond to all fields located on the grid surface. Note that the " \sim " symbol above the field variables associates these fields with the $3 \times 3 \times (T + 1)$ cell space. For waves in anisotropic materials, such as a magnetized plasma (discussed in Section 2.5.2 and elsewhere in this dissertation), we also need to specify $\widetilde{J}_{xt}|_{i+.5, j_0+m, k_0+p}^\omega$, $\widetilde{J}_{yt}|_{i, j_0+.5+m, k_0+p}^\omega$, and $\widetilde{J}_{zt}|_{i, j_0+m, k_0+.5+p}^\omega$, which are found in the same manner as the electric fields. These specified fields provide enough information to carry out the simulations.

Our general procedure for calculating the reflection coefficient using the time domain simulation can be described as follows:

- 1) We multiply grid surface boundary fields by the input spectrum of the incident wave, $S(\omega)$, and compute the inverse FFT of these fields to obtain the time domain boundary fields as follows:

$$\begin{aligned} \widetilde{E}_{xt}|_{i+.5, j_0+m, k_0+p}^n &= FFT^{-1}(\widetilde{E}_{xt}|_{i+.5, j_0+m, k_0+p}^\omega) \\ &= FFT^{-1}(E_{xt}|_{i-.5, j_0, k_0}^{n=0, \omega} e^{-j(k_y m \Delta y + k_z p \Delta z)} S(\omega)) \end{aligned} \quad (2.22)$$

$$\begin{aligned} \widetilde{E}_{yt}|_{i, j_0+.5+m, k_0+p}^n &= FFT^{-1}(\widetilde{E}_{yt}|_{i, j_0+.5+m, k_0+p}^\omega) \\ &= FFT^{-1}(E_{yt}|_{i, j_0+.5, k_0}^{n=0, \omega} e^{-j(k_y m \Delta y + k_z p \Delta z)} S(\omega)) \end{aligned} \quad (2.23)$$

$$\begin{aligned} \widetilde{E}_{zt}|_{i, j_0+m, k_0+.5+p}^n &= FFT^{-1}(\widetilde{E}_{zt}|_{i, j_0+m, k_0+.5+p}^\omega) \\ &= FFT^{-1}(E_{zt}|_{i, j_0, k_0+.5}^{n=0, \omega} e^{-j(k_y m \Delta y + k_z p \Delta z)} S(\omega)) \end{aligned} \quad (2.24)$$

where for anisotropic materials, the boundary fields $\widetilde{J}_{xt}|_{i+.5, j_0+m, k_0+p}^n$,

$\widetilde{J}_{yt}|_{i, j_0+.5+m, k_0+p}^n$, and $\widetilde{J}_{zt}|_{i, j_0+m, k_0+.5+p}^n$ are found in the same manner.

- 2) We run the FDTD equations within the space coupled with the grid surface

boundary fields while saving $\widehat{H}_{xt}|_{i=0,j_0+.5,k_0+.5}^{n+.5}$, $\widehat{H}_{yt}|_{i=+.5,j_0,k_0+.5}^{n+.5}$ and $\widehat{H}_{zt}|_{i=+.5,j_0+.5,k_0}^{n+.5}$ over time.

- 3) We compute the FFT of these field values and divide by the input spectrum to normalize the fields as follows:

$$\widehat{H}_{xt}|_{i=0,j_0+.5,k_0+.5}^{\omega} = FFT(\widehat{H}_{xt}|_{i=0,j_0+.5,k_0+.5}^{n+.5})/S(\omega) \quad (2.25)$$

$$\widehat{H}_{yt}|_{i=+.5,j_0,k_0+.5}^{\omega} = FFT(\widehat{H}_{yt}|_{i=+.5,j_0,k_0+.5}^{n+.5})/S(\omega) \quad (2.26)$$

$$\widehat{H}_{zt}|_{i=+.5,j_0+.5,k_0}^{\omega} = FFT(\widehat{H}_{zt}|_{i=+.5,j_0+.5,k_0}^{n+.5})/S(\omega) \quad (2.27)$$

- 4) We calculate the reflection coefficient with the following equation.

$$\begin{aligned} \|\widehat{R}(\omega, \theta, \phi)\|_2 &= \\ &\sqrt{\frac{|\widehat{H}_{xs}|_{i=0,j_0+.5,k_0+.5}^{\omega}|^2 + |\widehat{H}_{ys}|_{i=+.5,j_0,k_0+.5}^{\omega}|^2 + |\widehat{H}_{zs}|_{i=+.5,j=j_0+.5,k_0}^{\omega}|^2}{|H_{xi}|_{i=0,j_0+.5,k_0+.5}^{n+.5,\omega}|^2 + |H_{yi}|_{i=+.5,j_0,k_0+.5}^{n+.5,\omega}|^2 + |H_{zi}|_{i=+.5,j=j_0+.5,k_0}^{n+.5,\omega}|^2}} \end{aligned} \quad (2.28)$$

This time domain method for calculating the numerical reflection coefficient is equivalent to the frequency domain derivation discussed in Chapter 4. Mathematically, they must yield the same results over the spectral energy range of $S(\omega)$ because both methods originate from the same difference equations. Any differences between the results of the two methods must thus be due to numerical error.

Table 2.1: Numerical values of the CCO-PML coefficient profile, Profile A.

i	$b_{x1}(i)$	$e^{\alpha_{x1}(i)\Delta t}$	i	$b_{x1}(i)$	$e^{\alpha_{x1}(i)\Delta t}$
1.0	1.0	0.9997	6.0	1.0	0.8012
1.5	1.0	0.9984	6.5	1.0	0.7421
2.0	1.0	0.9953	7.0	1.0	0.6730
2.5	1.0	0.9897	7.5	1.0	0.5941
3.0	1.0	0.9807	8.0	1.0	0.5062
3.5	1.0	0.9674	8.5	1.0	0.4115
4.0	1.0	0.9487	9.0	1.0	0.3142
4.5	1.0	0.9237	9.5	1.0	0.2203
5.0	1.0	0.8914	10.0	1.0	0.1379
5.5	1.0	0.8508	10.5	1.0	0.0741

We present three numerical experiments below in Sections 2.5.1, 2.5.2, and 2.5.3. Each numerical experiment involves calculating the reflection coefficient of a plane wave incident onto the PML at various angles of incidence (or various modes for the case of waveguides). For all numerical experiments the incident wave time domain input pulse at $\widetilde{E}_{zi}|_{i=0,j_0,k_0+.5}^n$ is a modulated Gaussian with a full-width half-maximum of $45\Delta t$ for the Gaussian envelope and a modulation angular frequency of $2\pi/12.5\Delta t$. Table 2.5 shows the numerical values of the CCO-PML coefficient profile, denoted Profile A. In all numerical tests we apply Profile A, which is an order N=1 CCO-PML and has only real coefficients. In all the numerical tests we also show results for an optimized profile obtained by adjustment of coefficients to minimize error. In this context, note that Profile A is the initial profile given to the optimizer for every optimized profile presented in the numerical experiments. For the optimization we use gradient methods which yield a local minimum, but not necessarily a global minimum, to optimize $||\overline{R(\omega, \theta, \phi)}||_2$ for our frequency range of interest.

2.5.1 Plane Waves Incident onto the PML from Free Space

Our first experiment compares the calculation of the reflection coefficient for a free space plane wave incident on the PML for both the frequency and time domain

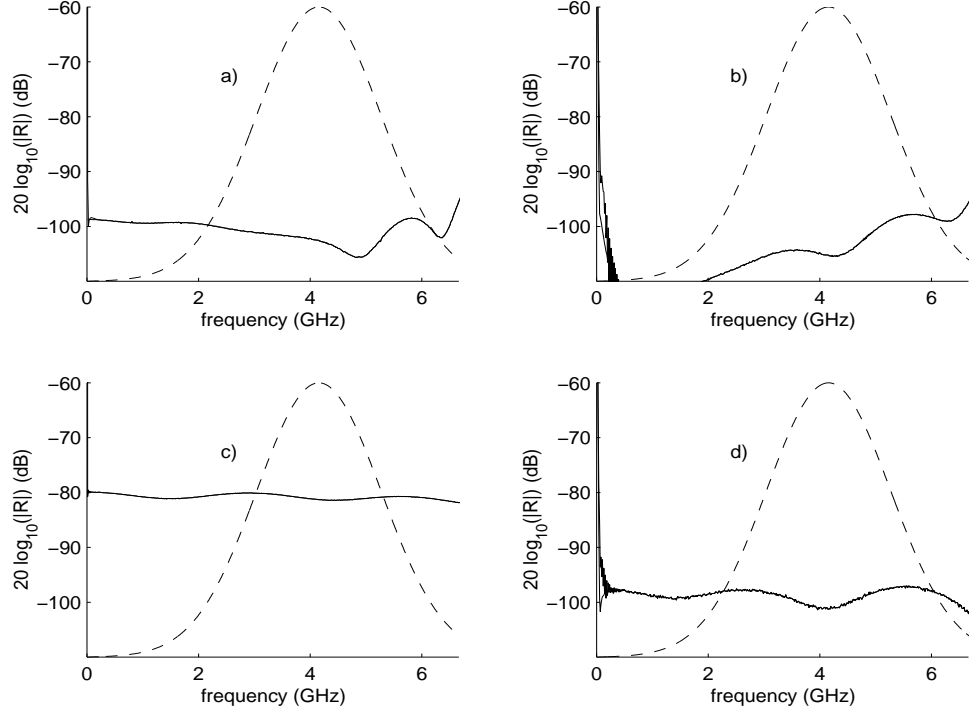


Figure 2.5: Refection coefficient for the frequency and time domain methods ($S(\omega)$ also plotted) for various angles of incidence (free space). a) Profile A, ($\theta = \pi/3$, $\phi = \pi/10$). b) Profile B, ($\theta = \pi/3$, $\phi = \pi/10$). c) Profile A, ($\theta = \pi/2$, $\phi = \pi/2.9$). d) Profile B, ($\theta = \pi/2$, $\phi = \pi/2.9$).

methods. This comparison is provided for two different incident angles, ($\theta = \pi/3$, $\phi = \pi/10$) and ($\theta = \pi/2$, $\phi = \pi/2.9$). The cell size of our space is, $\Delta x = \Delta y = \Delta z = .01$ m. The time domain method was run for 4000 timesteps with $\Delta t = \Delta x / (\sqrt{3}c)$. We ran the optimization scheme described in Section 2.4, optimizing $\|R(\omega, \theta, \phi)\|_2$, using profile A as the initial profile of an order $N=1$ CCO-PML profile with complex coefficients. The resulting optimized profile, so determined by locally minimizing error, is termed 'Profile B'. The reflection coefficients using Profile A for the two different angles of incidence are respectively shown in Figure 2.5a and 2.5c. The reflection coefficients using Profile B for the two different angles of incidence are respectively shown in Figure 2.5b and 2.5d. In each case, the frequency and time domain methods are identical for the spectral energy range of $S(\omega)$ (also plotted), except in Figure 2.5b and

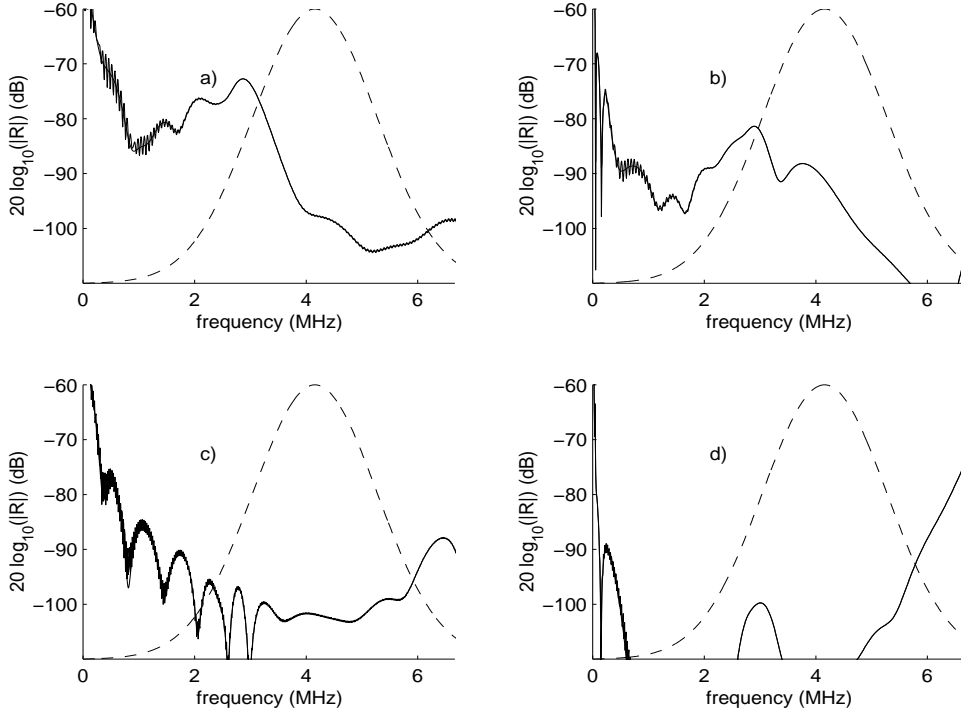


Figure 2.6: Refection coefficient for the frequency and time domain methods ($S(\omega)$ also plotted) for various angles of incidence (magnetoplasma). a) Profile A, ($\theta = \pi/3$, $\phi = \pi/10$). b) Profile C, ($\theta = \pi/3$, $\phi = \pi/10$). c) Profile A, ($\theta = \pi/2$, $\phi = 0$). d) Profile C, ($\theta = \pi/2$, $\phi = 0$).

2.5d where there is some noise in the time domain method at the lowest frequencies. This is due to the fact that the 4000 timesteps used are not long enough for the time domain method at low frequencies so that results have not properly converged. For the incidence angle ($\theta = \pi/3$, $\phi = \pi/10$), the reflection coefficients for Profile A and Profile B are quite similar. For incidence angle ($\theta = \pi/2$, $\phi = \pi/2.9$) the reflection coefficient for Profile B is about 18 dB better on the average. At the lowest frequencies, the reflection coefficients for Profile B have a poorer response. The maximum frequency plotted in Figure 2.5 corresponds to 4.5 cells per free space wavelength.

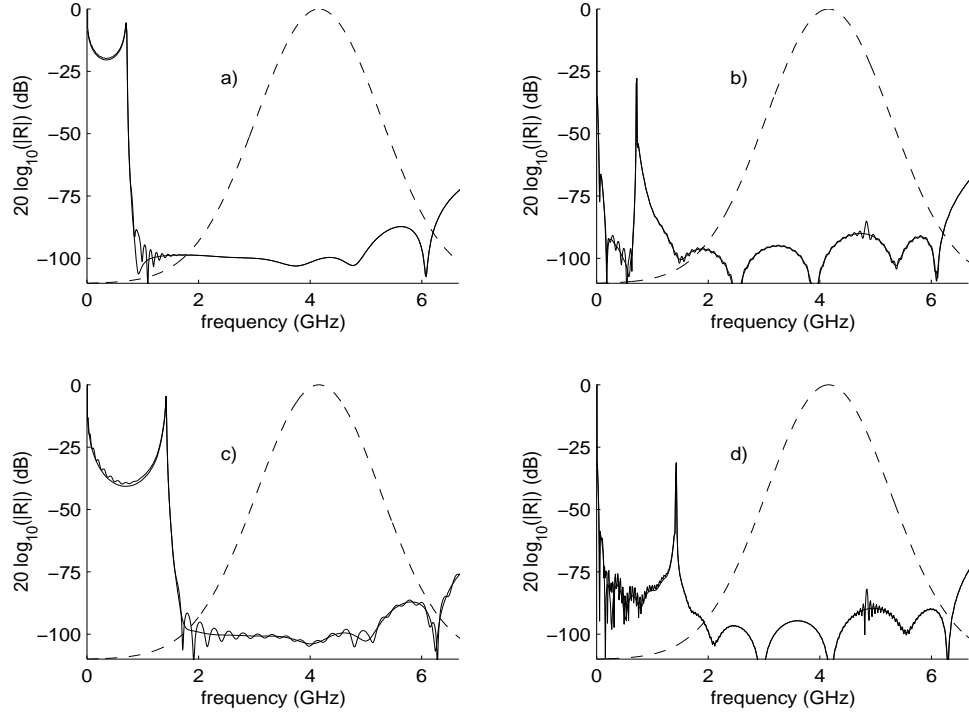


Figure 2.7: Refection coefficient for the frequency and time domain methods ($S(\omega)$ also plotted) for various incident modes (free space waveguide). a) Profile A, $n = 1$ mode. b) Profile D, $n = 1$ mode. c) Profile A, $n = 2$ mode. d) Profile D, $n = 2$ mode.

2.5.2 Plane Waves Incident onto the PML from a Magneto-plasma

Our second experiment compares the calculated reflection coefficients for a right-hand elliptically polarized plane wave in an anisotropic magnetoplasma incident on the PML for both the frequency and time domain methods. To model the plasma we apply the method of *Lee and Kalluri* (1999) except for the fact that in our grid we collocate the vector electric currents with the vector electric fields instead of locating the vector electric currents on the Yee cell vertices. The update equations for the anisotropic current tensor, $\vec{J} = \sigma \vec{E}$ derived by the *Lee and Kalluri* (1999) method are (A.7)-(A.9) in Appendix A.

Results are calculated for two different incident angles, $(\theta = \pi/3, \phi = \pi/10)$ and

($\theta = \pi/2$, $\phi = 0$). The cell size of our space is $\Delta x = \Delta y = \Delta z = 10$ m. The parameters of the magnetoplasma are the ambient magnetic field, $\vec{B}_0 = 1 \times 10^{-5} \hat{a}_x$ Tesla, the electron density $N_e = 1 \times 10^{11}$ el/m³, and the collision frequency $\nu = 5 \times 10^6$ s⁻¹. The time domain method was run for 8000 timesteps with $\Delta t = \Delta x / (\sqrt{3}c)$. We ran the optimization scheme described in Section 2.4, using Profile A as the input profile. Our optimized profile is an order N=2 CCO-PML profile with complex coefficients which we refer to as 'Profile C'. The reflection coefficients using profile A for the two different angles of incidence are respectively shown in Figure 2.6a and Figure 2.6c while those for Profile C are respectively shown in Figure 2.6b and 2.6d. In each case, the frequency and time domain methods are identical for the spectral energy range of $S(\omega)$ (also plotted), except for some noise in the lower and higher frequencies in the time domain method curve due to the fact that 8000 timesteps is not quite enough for the time domain method. Figure 2.6a shows a peak between 1.8 and 3.8 MHz. We see that in Figure 2.6b, the use of Profile C leads to a reduction of this peak. We had originally tried optimizing an order N=1 CCO-PML profile, but that resulting optimized profile was not able to remove the peak. The lower frequency responses are also better for Profile B as well. The maximum frequency plotted in Figure 2.6 corresponds to 4.5 cells per free space wavelength.

2.5.3 Waveguide Modes Incident onto the PML

Our final numerical experiment examines the performance of the optimized PML for TM_z free space waveguide modes, propagating and evanescent. The dispersion relationship for the modes are

$$\begin{aligned} \varepsilon_0 \mu_0 \left[\frac{2j \sin \frac{\omega \Delta t}{2}}{\Delta t} \right]^2 &= \left[\frac{2j \sin \frac{k \sin(\theta) \cos(\phi) \Delta x}{2}}{\Delta x} \right]^2 \\ &+ \left[\frac{2j \sin \frac{k \sin(\theta) \sin(\phi) \Delta y}{2}}{\Delta y} \right]^2 \\ &+ \left[\frac{2j \sin \frac{k \cos(\theta) \Delta z}{2}}{\Delta z} \right]^2 \end{aligned}$$

$$(2.29)$$

$$k \sin(\theta) \sin(\phi) \Delta y = \frac{n\pi}{N_{\text{cells}} + 1}$$

$$(2.30)$$

where $\theta = \pi/2$. The wave number k and the complex angle ϕ are obtained from the two equations above. N_{cells} is the cellular width of the waveguide with n being the mode number. Our FDTD space has $\Delta x = \Delta y = \Delta z = .01$ m and solutions are calculated for modes $n=1$ and 2. Again we apply the method since we still have an incident plane wave, albeit evanescent or propagating. The time domain method in this case was run for 6000 timesteps with $\Delta t = \Delta x / (\sqrt{3}c)$. The optimization scheme described in Section 2.4 was applied using Profile A as the starting profile. Our optimized profile is an order $N=1$ CCO-PML profile with complex coefficients which we refer to as 'Profile D'. The reflection coefficients using Profile A for the two different modes are respectively shown in Figure 2.7a and 2.7c while those for Profile D are respectively shown in Figure 2.7b and 2.7d. In each case, the frequency and time domain methods are identical for the spectral energy range of $S(\omega)$ (also plotted), except for some noise in the time domain curve due to 6000 timesteps not being quite long enough for the time domain method. For both modes, the evanescent regions of the reflection coefficient are much improved using Profile D. The reflection coefficients are similar within the propagating regions for the two profiles. The maximum frequency plotted in Figure 2.7 corresponds to 4.5 cells per free space wavelength.

Chapter 3

A PML Utilizing k-Vector Information

The original PMLs introduced by *Berenger* (1994) and *Chew and Weedon* (1994) work well when the group and phase velocities of the incident wave are in the same direction. However, if these directions differ, as is the case for negative refractive index materials (NIMs) [*Veselago*, 1968; *Eleftheriades and Balmain*, 2005] and some anisotropic materials, such as certain electromagnetic propagation modes in magnetized plasmas, the regular PML ceases to attenuate the field and can in fact act as an amplifier. *Becache et al.* (2003) confirm this behavior with a theoretical analysis of PMLs for anisotropic media including acoustic waves in elastic materials as well as electromagnetic waves. Their work is based on the split-field formulation of *Berenger* (1994). *Cummer* (2005) discusses the PML amplification phenomenon for NIMs which exhibit both positive and negative refractive indexes over a range of frequencies. He then derives a frequency dependent solution referred to as the NIMPML which is an adaptation of the previously introduced NPML [*Cummer*, 2003].

Chevalier et al. (2006a) encounter the problems discussed in *Becache et al.* (2003) when modeling the performance of an antenna in a magnetized plasma for whistler-mode plasma waves. In this paper, we discuss a PML which can be adapted to the direction of the group velocity as a function of frequency and k-vector direction. We then explicitly derive the PML equations for the whistler-mode in a magnetized

plasma with the ambient magnetic field perpendicular to the direction of the PML as discussed in *Chevalier et al.* (2006a). We also derive expressions for the reflection coefficient and present numerical results for reflection coefficient calculations as well as for time domain simulations.

3.1 Derivation of k-Vector Dependent PML

We start with a brief review of the results of *Becache et al.* (2003) and *Cummer* (2005). We discuss 2D wave propagation in the xy plane only, and assume a k-vector of $\vec{k} = k_x \hat{x} + k_y \hat{y}$ and a group velocity of $\vec{v}_g = v_{gx} \hat{x} + v_{gy} \hat{y}$, where \vec{k} is the k-vector and \vec{v}_g is the group velocity. Our concern here is with the dot product of the \hat{x} -directed components of \vec{v}_g and \vec{k} , namely $v_{gx}k_x$. Figure 3.1a displays two index of refraction surfaces [*Helliwell*, 1965, p. 200] each at some chosen frequency. The direction of the vector from the origin to a given point on the index of refraction surface is the k-vector direction, i.e. the direction of the phase velocity. The magnitude of the same vector is the wave number $|\vec{k}|$ for that particular angle θ between the k-vector and the magnetic field \vec{B}_0 . The direction of the vector that is normal to the index of refraction surface at the tip of the k-vector is the group velocity direction. The surface on the left is for a positive index of refraction, isotropic material, for which $v_{gx}k_x > 0$ always holds true. For the surface on the right hand side, which represents the whistler mode in a magnetized plasma, we see that $v_{gx1}k_{x1} > 0$ but $v_{gx2}k_{x2} < 0$. The so-called ‘Gendrin’ angle [*Gendrin*, 1961], labeled θ_g in Figure 3.1a, is the angle at which the product $n \cos \theta$, where n is the whistler-mode index of refraction, exhibits a minimum along the x-axis at two locations. The Gendrin angle is also the non-zero k-vector angle at which the group velocity is (anti)parallel to the ambient magnetic field and is the transition angle at which $v_{gx}k_x$ changes sign. The relationship for the Gendrin angle in a dense magnetized plasma is $\cos(\theta_g) \simeq 2\omega/\omega_c$, where ω_c is the local electron gyrofrequency. By a dense plasma, we mean $\omega_c \ll \omega_p$, where ω_p is the local electron plasma frequency. In the rest of this chapter we consider an x -directed PML only, unless otherwise noted. Figure 3.1b shows an x -directed PML, i.e., only PML attenuation in the x -direction, where the two examples $[\vec{v}_{g1}, \vec{k}_1]$ and $[\vec{v}_{g2}, \vec{k}_2]$

from the whistler index of refraction surface in Figure 3.1a have been placed incident onto the PML region. In both cases, it is the group velocity in the x -direction, ' v_{gx} ' that describes the speed in the x -direction at which the wave energy is incident on the PML, but it is the k -vector in the x -direction, ' k_x ' that determines whether the PML amplifies or attenuates the wave. The x -directed wave solution within the PML region has the form

$$e^{-jk_x x} e^{-\frac{\sigma_x k_x x}{\omega}} \quad (3.1)$$

For $v_{gx} > 0, k_x > 0$ the wave solution attenuates within the PML, i.e., the case for v_{gx1}, k_{x1} . For $v_{gx} > 0, k_x < 0$ the wave solution grows within the PML, i.e., the case for v_{gx2}, k_{x2} . We therefore need to somehow incorporate information about $v_{gx}k_x$ into the PML, or at least about the appropriate sign of $v_{gx}k_x$. We define the incident k -vector as $\vec{k}_{inc} = k_x \hat{x} + k_y \hat{y}$ and the k -vector within the PML to be $\vec{k}_{pml} = k_{x_{pml}} \hat{x} + k_y \hat{y}$. In accordance with Snell's law and for an x -directed PML, k_y is preserved through the two media. We introduce the function, $f(\omega, k_{x_{pml}}, k_y)$ as a means to introduce k -vector dependence into the PML function. The x -directed portion of the PML wave solution is taken to have the form:

$$e^{-jk_{x_{pml}} x} = e^{-j(\kappa k_x x (1 + \frac{\sigma_x f(\omega, k_{x_{pml}}, k_y)}{j\omega}))} = e^{-jk_x s_x x} \quad (3.2)$$

where $f(\omega, k_{x_{pml}}, k_y) = 1$ reduces to the original Berenger PML. The term κ is the tradition PML term for attenuating evanescent fields. In order for (3.2) to always have an attenuating solution we require that $f(\omega, k_{x_{pml}}, k_y)$ has the same sign as $v_{gx}k_x$. Equation (3.2) is similar to the formulation of *Cummer* (2005), but we have additionally included k -vector direction information by including k -dependence explicitly in our PML attenuation function. We refer to this new PML as the 'KPML', where 'K' refers to the use of k -vector information. Considering the whistler mode in a

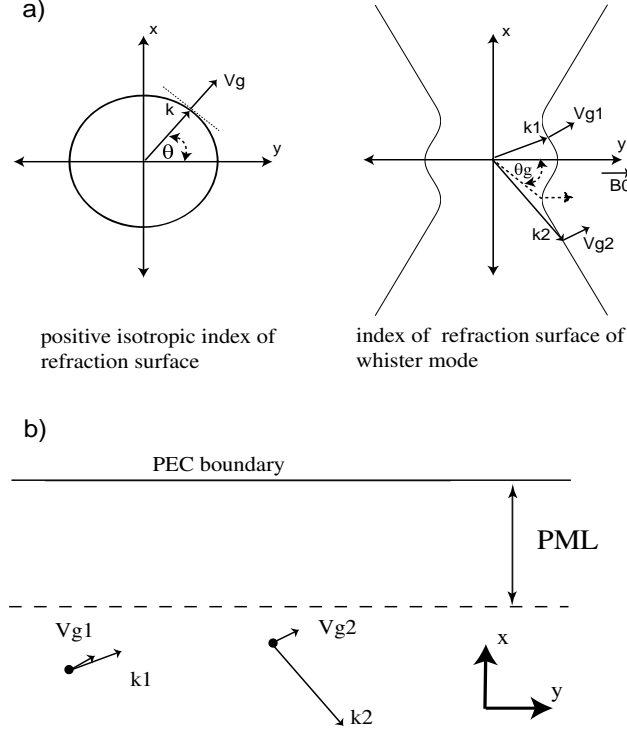


Figure 3.1: a) Index of refraction surfaces. b) Two whistler waves incident on the PML [Chevalier et al., 2006a].

magnetized plasma as an explicit example, ideally the function $f(\cdot)$ might be

$$\begin{aligned}
 f_{\text{ideal}}(\omega, k_x, k_y) &= k^2 \left[\cos^2(\theta) - \cos^2(\theta_g) \right] \frac{1}{1 - \omega^2/\omega_0^2} \\
 &= \left(k_y^2 - \frac{4\omega^2}{\omega_c^2} [k_x^2 + k_y^2] \right) \frac{1}{1 - \omega^2/\omega_0^2}
 \end{aligned} \tag{3.3}$$

where we define θ as the angle with respect to the y -axis as well as the static magnetic field as in Figure 3.1a. The function $f_{\text{ideal}}(\cdot)$ has perfect transition through the Gendrin angle from positive to negative values following the sign of the quantity $v_{gx}k_x$. The term $1/(1 - \omega^2/\omega_0^2)$ is applied from Cummer (2005) for generality and changes sign at $\omega = \omega_0$, where ω_0 is a user-adjustable parameter. To ensure that

$1/(1 - \omega^2/\omega_0^2)$ is positive over the frequency range of the whistler mode we require that $\omega_0 > \omega_c$. For actual implementation, $f(\cdot)$ must have the form

$$f(\omega, k_{x_{\text{pml}}}, k_y) = \left\{ k_y^2 - \frac{4\omega^2}{\omega_c^2} \left(\left[\frac{k_{x_{\text{pml}}}}{\kappa} \right]^2 + k_y^2 \right) \right\} \frac{1}{1 - \omega^2/\omega_0^2} \quad (3.4)$$

where we have simply replaced k_x , the x -component of the \mathbf{k} -vector in the magnetized plasma, from (3.3) with $k_{x_{\text{pml}}}/\kappa$, the x -component of the \mathbf{k} -vector within the PML. The reason that $f(\cdot)$ must necessarily be of the form in (3.4) is the fact that (3.4) can be implemented using linear differential equations, as show below. On the other hand, it is not apparent how this can be done within the PML for the ideal function, given by (3.3). Note that $k_{x_{\text{pml}}}$ is in general complex since it includes the PML losses as well as information about the incident wave k_x . From (3.2) it can be shown that $k_{x_{\text{pml}}} = \kappa k_x [1 + \sigma_x f(\omega, k_{x_{\text{pml}}}, k_y)/j\omega]$. As a result, $f(\cdot)$ is complex, and we therefore must apply it with care. Also, to clarify, in (3.4), the term $(k_{x_{\text{pml}}}/\kappa)^2$ is this way because it removes the evanescent scaling factor κ from $k_{x_{\text{pml}}}$ so that $k_{x_{\text{pml}}}/\kappa$ more closely maps to k_x , especially as $\sigma_x \rightarrow 0$.

In the following, we derive the update equations for the implementation of (3.4), by applying the stretched coordinate form of [Chew and Weedon (1994)] on our x -directed PML spatial operator to obtain the form:

$$\frac{1}{s_x} \frac{\partial}{\partial x} = \frac{1/\kappa}{1 + \sigma_x f(\omega, k_{x_{\text{pml}}}, k_y)/j\omega} \frac{\partial}{\partial x} \quad (3.5)$$

Assuming $f(\omega, k_{x_{\text{pml}}}, k_y)$ takes the form of (3.4), the PML spatial operator then becomes

$$\frac{1}{s_x} \frac{\partial}{\partial x} = \frac{(j\omega + [j\omega]^3/\omega_0^2)/\kappa}{j\omega + (j\omega)^3/\omega_0^2 + \sigma_x \left(k_y^2 - \frac{4\omega^2}{\omega_c^2} \left[\left(\frac{k_{x_{\text{pml}}}}{\kappa} \right)^2 + k_y^2 \right] \right)} \frac{\partial}{\partial x} \quad (3.6)$$

Since we exclusively consider plane wave analysis we have $\partial/\partial x \rightarrow -jk_{x_{\text{pml}}}$. If we assume to operate on H_z and introduce the auxiliary variable, $\Psi_{H_z}^x$, we can rewrite equation (3.6) as

$$\frac{-jk_{x_{\text{pml}}}(j\omega + [j\omega]^3/\omega_0^2)/\kappa}{j\omega + (j\omega)^3/\omega_0^2 + \sigma_x \left(k_y^2 - \frac{4\omega^2}{\omega_c^2} \left[\left(\frac{k_{x_{\text{pml}}}}{\kappa} \right)^2 + k_y^2 \right] \right)} H_z = \Psi_{H_z}^x \quad (3.7)$$

for which the most natural method of solution would be an auxiliary differential equation. After some manipulation and inverse transformation from k space we obtain

$$\begin{aligned} j\omega \frac{\partial H_z}{\kappa \partial x} + \frac{[j\omega]^3}{\omega_0^2} \frac{\partial H_z}{\kappa \partial x} &= j\omega \Psi_{H_z}^x + \frac{[j\omega]^3}{\omega_0^2} \Psi_{H_z}^x - \sigma_x \frac{\partial^2}{\partial y^2} \Psi_{H_z}^x \\ &\quad - \sigma_x \frac{4[j\omega]^2}{\omega_c^2} \left(\frac{\partial^2}{\kappa^2 \partial x^2} \Psi_{H_z}^x + \frac{\partial^2}{\partial y^2} \Psi_{H_z}^x \right) \end{aligned} \quad (3.8)$$

we then apply the inverse Fourier transform to yield the the time domain equation

$$\begin{aligned} \frac{\partial}{\partial t} \frac{\partial H_z}{\kappa \partial x} + \frac{1}{\omega_0^2} \frac{\partial^3}{\partial t^3} \frac{\partial H_z}{\kappa \partial x} &= \frac{\partial}{\partial t} \Psi_{H_z}^x + \frac{1}{\omega_0^2} \frac{\partial^3}{\partial t^3} \Psi_{H_z}^x - \sigma_x \frac{\partial^2}{\partial y^2} \Psi_{H_z}^x \\ &\quad - \sigma_x \frac{4}{\omega_c^2} \left(\frac{\partial^4}{\partial t^2 \kappa^2 \partial x^2} \Psi_{H_z}^x + \frac{\partial^4}{\partial t^2 \partial y^2} \Psi_{H_z}^x \right) \end{aligned} \quad (3.9)$$

The important result in (3.8) and (3.9) is the use of spatial derivatives to gain information about the waves in the PML region, where we have tailored $f(\omega, k_{x_{\text{pml}}}, k_y)$ such that it follows the sign of $v_{gx}k_x$. This procedure ensures that the PML attenuates all whistler-mode waves within it, regardless of the sign of $v_{gx}k_x$.

Applying finite differences to the y -dependent spatial derivative terms yields

$$\frac{\partial^2}{\partial y^2} \Psi_{H_z}^x \Rightarrow \frac{\Psi_{H_z}^x|_{i,j+1.5,k}^{n+.5} - 2\Psi_{H_z}^x|_{i,j+.5,k}^{n+.5} + \Psi_{H_z}^x|_{i,j-.5,k}^{n+.5}}{(\Delta y)^2} \quad (3.10)$$

and

$$\begin{aligned}
\frac{\partial^4}{\partial t^2 \partial y^2} \Psi_{H_z}^x &\Rightarrow \frac{\Psi_{H_z}^x|_{i,j+1.5,k}^{n+.5} - 2\Psi_{H_z}^x|_{i,j+.5,k}^{n+.5} + \Psi_{H_z}^x|_{i,j-.5,k}^{n+.5}}{(\Delta t)^2(\Delta y)^2} \\
&- 2\frac{\Psi_{H_z}^x|_{i,j+1.5,k}^{n-.5} - 2\Psi_{H_z}^x|_{i,j+.5,k}^{n-.5} + \Psi_{H_z}^x|_{i,j-.5,k}^{n-.5}}{(\Delta t)^2(\Delta y)^2} \\
&+ \frac{\Psi_{H_z}^x|_{i,j+1.5,k}^{n-1.5} - 2\Psi_{H_z}^x|_{i,j+.5,k}^{n-1.5} + \Psi_{H_z}^x|_{i,j-.5,k}^{n-1.5}}{(\Delta t)^2(\Delta y)^2}
\end{aligned} \tag{3.11}$$

where we would apply finite differences to the x -dependent derivative terms in the same manner. Note that since the $\Psi_{H_z}^x$ variables are updated to $n + .5$ the terms in (3.10) and (3.11) are implicit because to update $\Psi_{H_z}^x$ at the timestep $n + .5$ requires information of its nearest $\Psi_{H_z}^x$ neighbors at the timestep $n + .5$. The solution of the implicit equations is not difficult, but is computationally more demanding. Note that the electric and magnetic fields can still be updated using explicit leap-frog equations. For algorithmic speed, we therefore seek an explicit method for updating this equation. We can approximate (3.10) and (3.11) by shifting the $\Psi_{H_z}^x$ terms located at $i, j + 1.5, k$ and $i, j - .5, k$ back one timestep yielding

$$\frac{\partial^2}{\partial y^2} \Psi_{H_z}^x \simeq \frac{\Psi_{H_z}^x|_{i,j+1.5,k}^{n-.5} - 2\Psi_{H_z}^x|_{i,j+.5,k}^{n+.5} + \Psi_{H_z}^x|_{i,j-.5,k}^{n-.5}}{(\Delta y)^2} \tag{3.12}$$

and

$$\begin{aligned}
\frac{\partial^4}{\partial t^2 \partial y^2} \Psi_{H_z}^x &\simeq \frac{\Psi_{H_z}^x|_{i,j+1.5,k}^{n-.5} - 2\Psi_{H_z}^x|_{i,j+.5,k}^{n+.5} + \Psi_{H_z}^x|_{i,j-.5,k}^{n-.5}}{(\Delta t)^2(\Delta y)^2} \\
&- 2\frac{\Psi_{H_z}^x|_{i,j+1.5,k}^{n-1.5} - 2\Psi_{H_z}^x|_{i,j+.5,k}^{n-.5} + \Psi_{H_z}^x|_{i,j-.5,k}^{n-1.5}}{(\Delta t)^2(\Delta y)^2} \\
&+ \frac{\Psi_{H_z}^x|_{i,j+1.5,k}^{n-2.5} - 2\Psi_{H_z}^x|_{i,j+.5,k}^{n-1.5} + \Psi_{H_z}^x|_{i,j-.5,k}^{n-2.5}}{(\Delta t)^2(\Delta y)^2}
\end{aligned} \tag{3.13}$$

This method would also be applied to the x -dependent derivative terms. Solving (3.9) in this manner produces an explicit update equation with the only unknown variable being the $\Psi_{H_z}^x$ term located at $i, j + .5, k$ and at timestep $n + .5$. We examine results of both explicit and implicit time domain simulations in Section 3.2. Also, one can use (3.8) with the Finite-Difference Frequency-Domain (FDFD) method, although, numerical results for this are not presented in this dissertation.

3.2 Numerical Results

In this section we present results from time domain simulations as well as numerical reflection coefficient calculations for the KPML. The derivation of the numerical reflection coefficient is presented in Chapter 4. For some numerical tests we represent the PML attenuation factor $\sigma_x(i)$ as

$$\sigma_x(i)\Delta t = \sigma_{\max}\Delta t \left(\frac{i - .5}{T} \right)^m \quad (3.14)$$

where T is the PML thickness in number of cells and $\sigma_x(i)$ is nonzero for $i \geq 1$, i.e., the PML exists at $i \geq 1$. We define $D = [\sigma_{\max}\Delta t, m]$ so that $D = [1.5, 2]$ simply means that $\sigma_x(i)\Delta t = 1.5 ([i - .5]/T)^2$. For some numerical tests we use a Gaussian PML attenuation profile defined as

$$\sigma_x(i)\Delta t = \sigma_{\max}\Delta t e^{-\left(b \frac{(i-T-1)}{4T}\right)^2} \quad (3.15)$$

where the Gaussian profile is represented as $G = [\sigma_{\max}\Delta t, b]$. When specifying the evanescent term $\kappa(i)$ for ease of implementation, from *Chevalier and Inan* (2004) we have $1/\kappa(i) = 1 - b_0(i)$ where

$$b_0(i) = b_{0\max} \left(\frac{i - .5}{T} \right)^p \quad (3.16)$$

where the evanescent profile is simply represented by $B_0 = [b_{0\max}, p]$.

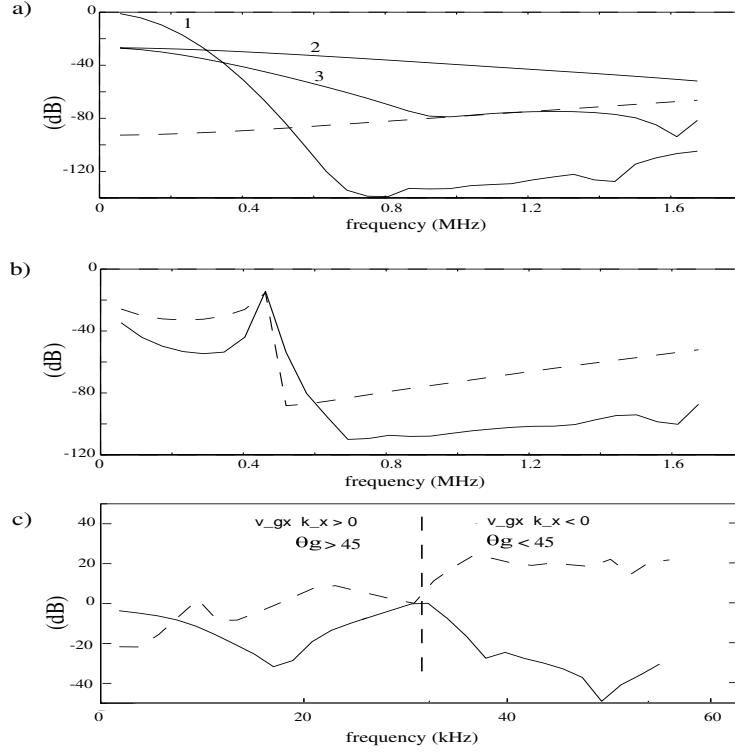


Figure 3.2: a) freespace reflection coefficients: curve 1: $f(\omega, k_{x_{\text{pml}}}, k_y) = k_y^2$, curve 2: $f(\omega, k_{x_{\text{pml}}}, k_y) = k_{x_{\text{pml}}}^2$, curve 3: $f(\omega, k_{x_{\text{pml}}}, k_y) = k_{x_{\text{pml}}}^2 + k_y^2$, dashed curve: convolutional PML. b) freespace waveguide reflection coefficients (N=2 mode); solid curve: KPML, dashed curve: convolutional PML. c) magnetized plasma reflection coefficients for incident angle of 45 degrees; solid curve: KPML, dashed curve: convolutional PML.

3.2.1 Free space and free space waveguide

We first apply the KPML to familiar situations, i.e., free-space propagation and the free-space-filled waveguide, as a reality check before we apply it to a magnetized plasma. For both cases the FDTD spaces have $\Delta x = \Delta y = \Delta z = 30 \text{ m}$ and $\Delta t = \Delta x / \sqrt{3}c$. For a given PML attenuation profile we calculate the numerical reflection coefficient. For both the free-space and the free-space-filled waveguide, we use profile $D = [15.5, 2.0]$, which is not an optimized attenuation profile and is in fact not meant to be. We apply no evanescent attenuation, i.e., $\kappa(i) = 1.0$, $B_0 = [0, 0]$. The PML thickness is $T = 15$ cells. Figure 3.2a plots the reflection coefficient for a few

different functions of $f(\omega, k_{x_{\text{pml}}}, k_y)$. For $f(\omega, k_{x_{\text{pml}}}, k_y) = k_y^2$, i.e., the curve labeled 1, we have poor low frequency response and excellent response at higher frequencies, as expected mathematically since k_y is always real and increases with frequency. For $f(\omega, k_{x_{\text{pml}}}, k_y) = k_{x_{\text{pml}}}^2$, i.e., the curve labeled 2, the reflection coefficient ranges between -30 to -50 dB. This performance is not very good, but since we know that $k_{x_{\text{pml}}}$ is complex within the PML we do not expect outstanding performance; nevertheless, we see that the formulation does work. For $f(\omega, k_{x_{\text{pml}}}, k_y) = k_{x_{\text{pml}}}^2 + k_y^2$, we find results to be about the average of the two previous ones. Finally, the dashed line represents the traditional PML, $f(\omega, k_{x_{\text{pml}}}, k_y) = 1.0$, using the same attenuation profile and calculated using the convolutional PML method. The convolutional PML performs the best overall.

We next calculate the reflection coefficient for the $N = 2$ mode of a 2D free-space-filled waveguide whose width is 20 cells. Figure 3.2b plots the reflection coefficient for the convolutional PML (dashed line) and for $f(\omega, k_{x_{\text{pml}}}, k_y) = k_y^2 = \sin^2(2\pi/20)$ (solid line). The KPML and the convolutional PML perform in a similar manner.

In addition, we obtained numerical results from both explicit and implicit time domain simulations. For the explicit simulations we apply standard Yee cell FDTD with the explicit implementation of (3.9). For the implicit time domain simulations we use a 2D fully implicit FDTD electromagnetic solver that applies the Single Diagonally Implicit Runge Kutta Methods (SDIRK) [Hairer *et al.* (2000, 2002)]. These fully implicit methods are unconditionally stable and provide accurate integration for stiff systems of equations, i.e, there is an at least an order of magnitude difference between the smallest and largest eigenvalues. We performed time domain tests with both the KPML and the convolutional PML coexisting within the space for a free-space grid and found the simulations to be stable, i.e., no numerical instabilities nor amplification of waves by the PML, over time for 20,000 timesteps for both the explicit and implicit simulations. Results of our tests indicate that these KPML functions work as absorbing boundary conditions, not as well for open free-space problems as the traditional PML, but reasonably well for the free-space-filled waveguide.

3.2.2 Magnetized plasma

We now apply the KPML to whistler mode waves in a magnetized plasma for which we expect it to perform better than the convolutional PML. For the reflection coefficient calculations and the explicit simulation we use an adapted version of *Lee and Kalluri* (1999) with the only modification being that we co-locate the vector electric currents with the electric fields on the FDTD grid instead of at the Yee cell vertices. The properties of the magnetoplasma considered herein are the electron density, $N_e = 2 \times 10^9$ el/m³, and the ambient magnetic field, $\hat{B}_0 = 3 \times 10^{-6} \hat{y}$ Tesla. The FDTD spaces have $\Delta x = \Delta y = \Delta z = 20$ m and $\Delta t = \Delta x / (\sqrt{3}c)$. The PML attenuation profile is gaussian with $G = [.15, 6.0]$ with a thickness of $T = 20$ cells. For the KPML we also apply an evanescent attenuation profile where $B_0 = [0.9, 3]$.

Figure 3.2c plots the numerical reflection coefficient for the convolutional PML (dashed line) and the KPML upon application of (3.4). The incident angle of the wave is 45 degrees for $v_{gx}k_x > 0$ and 45+180 degrees for $v_{gx}k_x < 0$. The incident power and reflected power are used to calculate the numerical reflection coefficient, typically considering just the reflected magnetic field component. We use power (instead of field components) for the magnetized plasma since Snell's law requires two reflected waves (with different phase velocities) and that therefore the power of each of the two reflected wave must be calculated and summed for a true representation of the reflected wave energy. The region to the left of the vertical dashed line in the plot (Figure 3.2c) is where the incident wave has $v_{gx}k_x > 0$, while to the right is where $v_{gx}k_x < 0$. It is on the right side where we expect the KPML to outperform the convolutional PML and we see that it does indeed do substantially better. As expected, the wave energy grows within the PML region for the case of the convolutional PML while the KPML attenuates the waves up to -40 dB. Even at the lower frequencies, where the incident wave has $v_{gx}k_x > 0$, the KPML performs better and attenuates all waves while the convolutional PML exhibits some amplification. This result is due to the fact that even for an incident wave with, $v_{gx}k_x > 0$, one of the two reflected waves at the PEC boundary can have $v_{gx}k_x < 0$ and thus would amplify within the convolutional PML. Also, one sees that the KPML reflection coefficient goes to zero at the frequency corresponding to $\theta_g = 45$ degrees, i.e., when the incident wave angle

equals θ_g . This result is realized by design since $f(\cdot) \rightarrow 0$ under this condition. That the reflection coefficient goes to zero at this angle does not cause a practical problem since there is no energy entering the PML at this angle; instead the wave energy is directed in the \hat{y} direction along the ambient magnetic field.

Next we perform time domain FDTD simulations for the space shown in Figure 3.3a. Once again we apply the explicit and implicit codes described in Section 3.2.1. We use a 20x20 cell space adjacent to a 20 cell PML and excite the fields with a single cell E_x source in the center of the space using a modulated Gaussian centered at 40 kHz with a bandwidth of 20 kHz. From (3.9) we set our adjustable parameter $\omega_0 = \sqrt{\omega_c \omega_p}$. Additionally, another mode near the plasma frequency of the system is amplified by the convolutional PML in the \hat{y} -direction [Chevalier et al., 2006a]. We apply a first order lowpass filter [Sarto and Scarlatti, 2001] to the electric and magnetic fields to remove the wave energy near and above the plasma frequency to suppress the artificial growth of wave energy. The lowpass filter does little to the whistler mode since its frequencies are at least an order of magnitude below the plasma frequency for the parameters chosen here. We compare results for three different simulations; Run 1: with the convolutional PML in the \hat{x} -direction and PEC in the \hat{y} -direction, and Run 2: with the KPML in the \hat{x} -direction and PEC in the \hat{y} -direction, and Run 3: with the KPML in the \hat{x} -direction and the convolutional PML in the \hat{y} -direction. For all three simulations we measured the \hat{x} -directed electric field at point ‘A’ in the grid over time. The results of Run 1 are plotted in Figure 3.3b; we see reflected waves amplified due to the convolutional PML as expected. For Run 2, results for which are plotted in Figure 3.3c, we see that the KPML remains stable. However there is still energy that is ringing around due to wave power that is directed in the \hat{y} -direction which the KPML is not designed to absorb. Run 3 has both the KPML and the convolutional PML coexisting in the grid. The results for Run 3 are plotted in Figure 3.3d. Here we see the field converges toward zero, as a function of time, as all waves are now being absorbed by both PMLs. Just as important is that the system remain stable for having both types of PMLs within the space. Simulations were run for 12,000 timesteps at the Courant condition, i.e., $\Delta t = \Delta x / (\sqrt{3}c)$, for the implicit code, while for the explicit FDTD code it was run for 16,000 timesteps at .7 of the Courant

condition. Both codes yield similar results. However, only the results for the explicit code are plotted. It should be noted, at least in the case of the explicit code, that for this simulation the KPML becomes unstable for $\sigma_{\max}\Delta t > 5.0$, absorbing the short wavelength incident whistler waves but exhibiting growth in long wavelength waves of the same frequency and eventually saturating the entire space. Therefore, in this case, the KPML breaks down as an absorbing boundary condition and consequently one must be careful in their choice of $\sigma_{\max}\Delta t$. However, for the free space case of Section 3.2.1, we found the KPML to be stable for all values of $\sigma_{\max}\Delta t$ so that the stability of the method does depend on the medium that the KPML is designed to match.

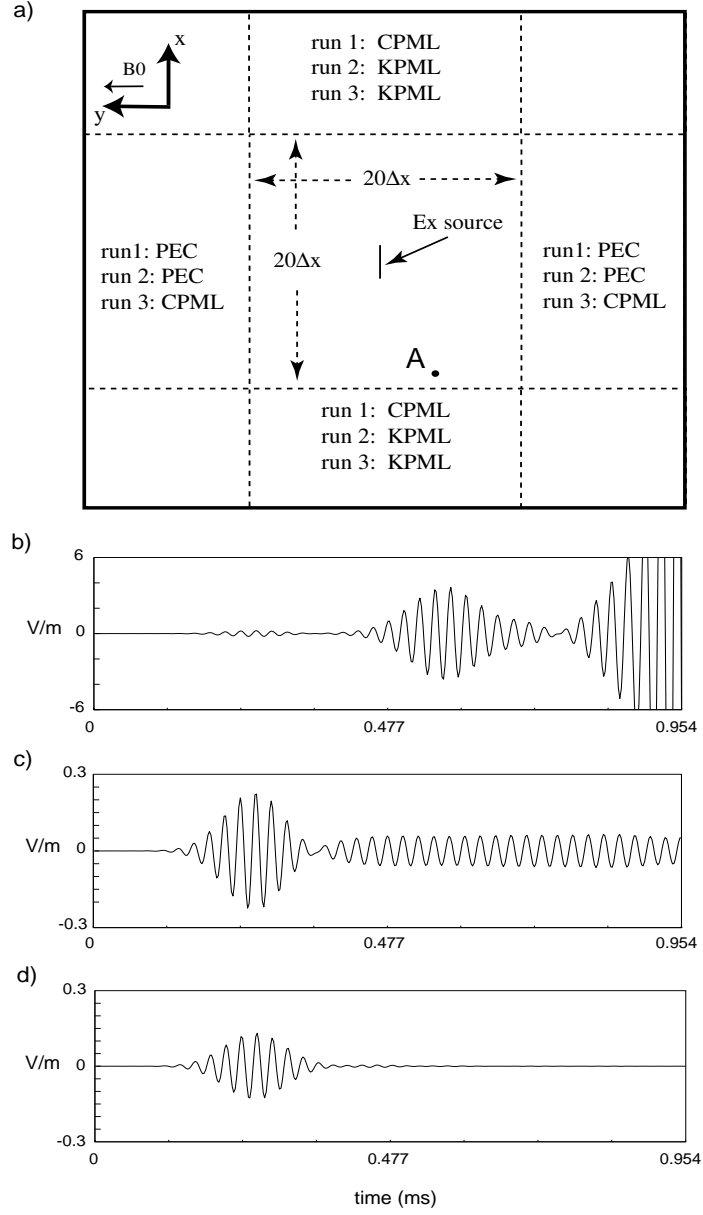


Figure 3.3: a) FDTD space for the magnetized plasma. b)-d) \hat{x} directed electric field at point 'A' over time for Run 1, Run 2, and Run 3, respectively.

Chapter 4

General Numerical Reflection Coefficient

In this Chapter, we develop a method for calculating the numerical reflection coefficient for a plane wave incident onto the PML. Numerical reflection coefficient calculations have been done previously. These include *Chew and Jin* (1996), *Fang and Wu* (1996), and *Berenger* (1999), all of which have all developed reflection calculations from a multi-layered split field PML. *Berenger* (2002a) develops and investigates the numerical reflection coefficients for particular cases of non-lossy isotropic media for various PML's, including split field, unsplit field, and complex frequency shifted PML (CFS-PML). *Berenger* (2002b) investigates the optimization of numerical reflection coefficients for evanescent and propagating waves for the CFS-PML in waveguides. We build upon this past work by deriving the numerical reflection coefficient for general linear media, including anisotropic media, for the CCO-PML as described in *Chevalier and Inan* (2004) and for the KPML as described in *Chevalier et al.* (2006). In addition, our approach to derivation of the numerical reflection coefficient is different than previous work. All the referenced work extends the work by *Chew and Jin* (1996), which derives an expression of the numerical reflection coefficient for one cell and then extends it to a T cell PML system and only deriving it for PML's truncating the domains of isotropic media. We simply set up the system with all the field variables, their governing equations and boundary conditions, which lends itself to a

straight forward extension to anisotropic media.

We now develop the method for calculating the numerical reflection coefficient for a plane wave, in a general linear medium, incident onto the Nth order CCO-PML or KPML for a given set of PML coefficients for a given PML cell thickness, T . The incident plane wave is written out explicitly as a function of incident angle (including complex angles), frequency, and polarization (important for anisotropic media) so that the dependence on each of these parameters can be studied. The reflection coefficient calculation quantifies the time-harmonic scattered plane wave fields, i.e., the numerical error due to the PML. The motivation for this calculation is to quantitatively determine the efficiency of the PML. The method is quite general, since any general electromagnetic field can be described by a linear superposition of both evanescent and propagating plane waves over incident angle and frequency. The notation for the time-harmonic fields within the finite difference grid, taking E_y for example is, $E_{yt}|_{i=0,j_0+.5,k_0}^{n,\omega}$, where n is the timestep, ω is radial frequency, and i, j, k is the grid node. Ultimately, we solve the total fields, i.e., incident plus scattered, for the incidence geometry in Figure 4.1b for $i \geq 0$.

4.1 Incident/Scattered Fields at $i=0$ Boundary

For the boundary condition at $i=0$ in Figure 4.1b, we must specify the total electric tangential fields and total electric tangential currents which can be decomposed into incident and scattered fields:

$$E_{yt}|_{i=0,j_0+.5,k_0}^{n,\omega} = E_{yi}|_{i=0,j_0+.5,k_0}^{n,\omega} + E_{ys}|_{i=0,j_0+.5,k_0}^{n,\omega} \quad (4.1)$$

$$E_{zt}|_{i=0,j_0,k_0+.5}^{n,\omega} = E_{zi}|_{i=0,j_0,k_0+.5}^{n,\omega} + E_{zs}|_{i=0,j_0,k_0+.5}^{n,\omega} \quad (4.2)$$

In addition, for an anisotropic plasma, the tangential electric currents must also be specified,

$$J_{yt} \big|_{i=0,j_0+.5,k_0}^{n+.5,\omega} = J_{yi} \big|_{i=0,j_0+.5,k_0}^{n+.5,\omega} + J_{ys} \big|_{i=0,j_0+.5,k_0}^{n+.5,\omega} \quad (4.3)$$

$$J_{zt} \big|_{i=0,j_0,k_0+.5}^{n+.5,\omega} = J_{zi} \big|_{i=0,j_0,k_0+.5}^{n+.5,\omega} + J_{zs} \big|_{i=0,j_0,k_0+.5}^{n+.5,\omega} \quad (4.4)$$

In the next section we develop a method for calculating the incident fields, while Section 4.1.2 we illustrate the representation of the scattered boundary fields $E_{ys} \big|_{i=0,j_0+.5,k_0}^{n,\omega}$, $E_{zs} \big|_{i=0,j_0,k_0+.5}^{n,\omega}$, $J_{ys} \big|_{i=0,j_0+.5,k_0}^{n+.5,\omega}$, and $J_{zs} \big|_{i=0,j_0,k_0+.5}^{n+.5,\omega}$ at $i = 0$ in terms of the scattered magnetic fields, $H_{ys} \big|_{i=.5,j_0,k_0+.5}^{n+.5,\omega}$, $H_{zs} \big|_{i=.5,j_0+.5,k_0}^{n+.5,\omega}$, which are given by

$$H_{ys} \big|_{i=.5,j_0,k_0+.5}^{n+.5,\omega} = H_{yt} \big|_{i=.5,j_0,k_0+.5}^{n+.5,\omega} - H_{yi} \big|_{i=.5,j_0,k_0+.5}^{n+.5,\omega} \quad (4.5)$$

$$H_{zs} \big|_{i=.5,j_0+.5,k_0}^{n+.5,\omega} = H_{zt} \big|_{i=.5,j_0+.5,k_0}^{n+.5,\omega} - H_{zi} \big|_{i=.5,j_0+.5,k_0}^{n+.5,\omega} \quad (4.6)$$

By doing so, we arrive at a closed system since boundary conditions are now specified by our incident fields and the total magnetic fields just inside the boundary from which we can uniquely solve the fields everywhere. We now discuss the calculation of the properties of the incident and scattered fields.

4.1.1 Incident fields

In this section we present the calculation of the properties of the incident plane wave (pictorially depicted in Figure 4.1a). We assume the wave is in an infinite homogeneous medium, i.e. without the PML. As in *Chew and Jin* (1996), *Fang and Wu* (1996), and *Berenger* (1999), we assume single frequency and plane wave fields. The incident wave has the form:

$$e^{j\omega n \Delta t} e^{-j(k_x i_x \Delta x + k_y i_y \Delta y + k_z i_z \Delta z)} = e^{j\omega n \Delta t} e^{-j(k \sin(\theta) \cos(\phi) i_x \Delta x + k \sin(\theta) \sin(\phi) i_y \Delta y + k \cos(\theta) i_z \Delta z)}$$

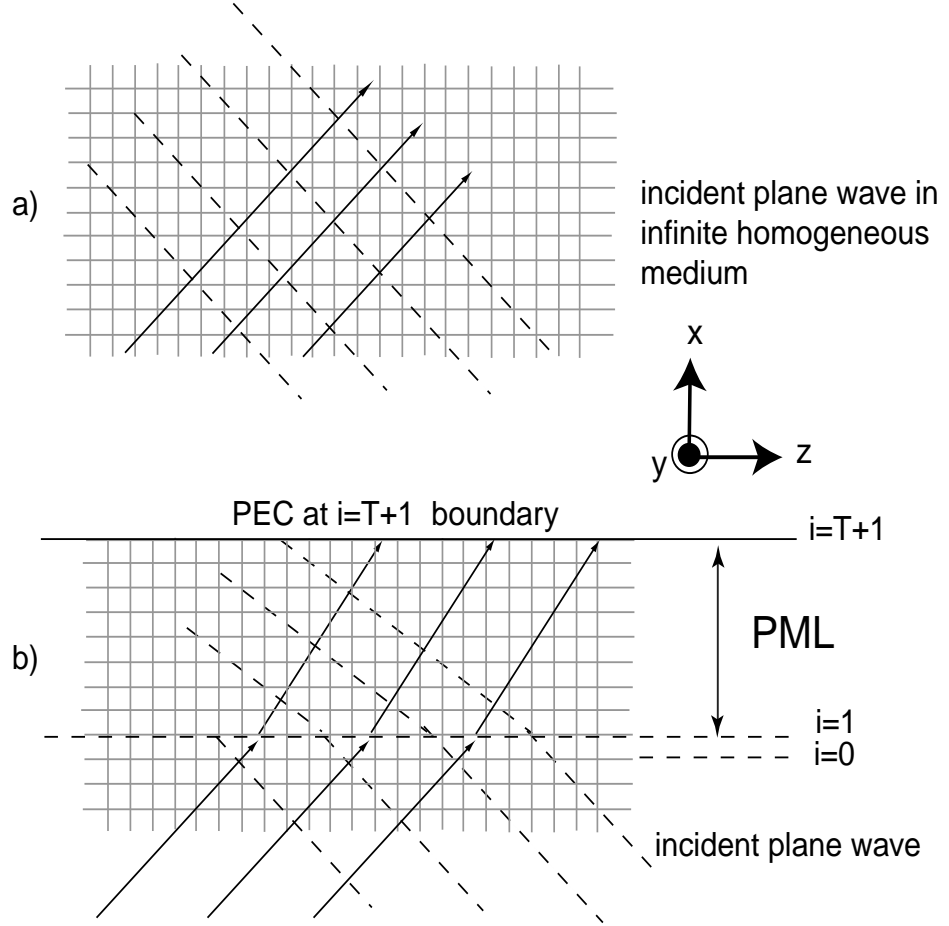


Figure 4.1: Illustration of plane waves travelling within an FDTD grid. a) An infinite grid of a homogeneous medium. b) A semi-infinite grid of a homogeneous medium with a matching PML. Scattered fields are present but are not explicitly shown.

(4.7)

where i_x, i_y, i_z are all integer indices. The indices i_x, i_y, i_z are heretofore replaced with the indices i, j, k . The $j = \sqrt{-1}$ term is also used in the equations but the indices i, j, k always appear together so there should be no confusion. We also have $k_x = k \sin(\theta) \cos(\phi), k_y = k \sin(\theta) \sin(\phi)$, and $k_z = k \cos(\theta)$. The wave number k is the actual wave number in the FDTD grid for a given frequency and propagation

angle. As a preview, it can be shown [Taflove and Hagness, 2000] that the dispersion characteristics for the plane wave in an FDTD space of a homogeneous isotropic medium is described by the equation

$$\left[\bar{\epsilon} \frac{2j \sin \frac{\omega \Delta t}{2}}{\Delta t} + \sigma \cos \frac{\omega \Delta t}{2} \right] \mu_0 \frac{2j \sin \frac{\omega \Delta t}{2}}{\Delta t} = \left[\frac{2j \sin \frac{k \sin(\theta) \cos(\phi) \Delta x}{2}}{\Delta x} \right]^2 + \left[\frac{2j \sin \frac{k \sin(\theta) \sin(\phi) \Delta y}{2}}{\Delta y} \right]^2 + \left[\frac{2j \sin \frac{k \cos(\theta) \Delta z}{2}}{\Delta z} \right]^2 \quad (4.8)$$

which allows one to solve for k for any given propagation angle and frequency. For anisotropic media, the dispersion relationship is not so simple but can nevertheless be calculated. In the following we discuss our method of iterative numerical solution for k for the media considered here. Note that we treat the electrical polarization currents \vec{J} in the following analysis. For ease of presentation, the magnetic polarization currents \vec{M} are set to zero since they are unnecessary in the media discussed in this dissertation. In applications when such currents are present they are present, they would be treated in the same manner as we treat \vec{J} . The spatial relationships for the fields E_x and H_y are:

$$E_x|_{i+.5 \pm 1, j \pm 1, k \pm 1}^{n, \omega} = E_x|_{i+.5, j, k}^{n, \omega} e^{\mp j k_x \Delta x} e^{\mp j k_y \Delta y} e^{\mp j k_z \Delta z} \quad (4.9a)$$

$$H_y|_{i+.5 \pm 1, j \pm 1, k+.5 \pm 1}^{n+.5, \omega} = H_y|_{i+.5, j, k+.5}^{n+.5, \omega} e^{\mp j k_x \Delta x} e^{\mp j k_y \Delta y} e^{\mp j k_z \Delta z} \quad (4.9b)$$

The above examples are directly applicable to the derivation of the spatial relationships for other field components E_y , E_z , H_x , H_z , etc. We also assume the following time relationships for E_x and H_y

$$E_x|_{i+.5, j, k}^{n \pm 1, \omega} = E_x|_{i+.5, j, k}^{n, \omega} e^{\pm j \omega \Delta t} \quad (4.10a)$$

$$H_y |_{i+.5,j,k+.5}^{n+.5\pm 1,\omega} = H_y |_{i+.5,j,k+.5}^{n+.5,\omega} e^{\pm j\omega\Delta t} \quad (4.10b)$$

and their forms are directly applicable to the derivation of the time relationships for the other field components. The following set of equations define plane wave propagation in our medium. Note that we use the field variables E_{xi} , E_{yi} , E_{zi} , H_{xi} , H_{yi} , H_{zi} , etc., where the 'i' is simply an indication that the quantity is the incident field. The general form of the time, spatial harmonic form the FDTD Maxwell update equations for the incident wave are

$$\begin{aligned} \bar{\epsilon} \frac{e^{j\omega\Delta t} - 1}{\Delta t} E_{xi} |_{i+.5,j,k}^{n,\omega} + J_{xi} |_{i+.5,j,k}^{n+.5,\omega} &= -\frac{1 - e^{jk_z\Delta z}}{\Delta z} H_{yi} |_{i+.5,j,k+.5}^{n+.5,\omega} \\ &+ \frac{1 - e^{jk_y\Delta y}}{\Delta y} H_{zi} |_{i+.5,j+.5,k}^{n+.5,\omega} \end{aligned} \quad (4.11)$$

$$\begin{aligned} \bar{\epsilon} \frac{e^{j\omega\Delta t} - 1}{\Delta t} E_{yi} |_{i,j+.5,k}^{n,\omega} + J_{yi} |_{i,j+.5,k}^{n+.5,\omega} &= \frac{1 - e^{jk_z\Delta z}}{\Delta z} H_{xi} |_{i,j+.5,k+.5}^{n+.5,\omega} \\ &- \frac{1 - e^{jk_x\Delta x}}{\Delta x} H_{zi} |_{i+.5,j+.5,k}^{n+.5,\omega} \end{aligned} \quad (4.12)$$

$$\begin{aligned} \bar{\epsilon} \frac{e^{j\omega\Delta t} - 1}{\Delta t} E_{zi} |_{i,j,k+.5}^{n,\omega} + J_{zi} |_{i,j,k+.5}^{n+.5,\omega} &= -\frac{1 - e^{jk_y\Delta y}}{\Delta y} H_{xi} |_{i,j+.5,k+.5}^{n+.5,\omega} \\ &+ \frac{1 - e^{jk_x\Delta x}}{\Delta x} H_{yi} |_{i+.5,j,k+.5}^{n+.5,\omega} \end{aligned} \quad (4.13)$$

$$\mu_0 \frac{1 - e^{-j\omega\Delta t}}{\Delta t} H_{xi} |_{i,j+.5,k+.5}^{n+.5,\omega} = \frac{e^{-jk_z\Delta z} - 1}{\Delta z} E_{yi} |_{i,j+.5,k}^{n,\omega} - \frac{e^{-jk_y\Delta y} - 1}{\Delta y} E_{zi} |_{i,j,k+.5}^{n,\omega}$$

(4.14)

$$\mu_0 \frac{1 - e^{-j\omega\Delta t}}{\Delta t} H_{yi} |_{i+.5,j,k+.5}^{n+.5,\omega} = -\frac{e^{-jk_z\Delta z} - 1}{\Delta z} E_{xi} |_{i+.5,j,k}^{n,\omega} + \frac{1 - e^{jk_x\Delta x}}{\Delta x} E_{zi} |_{i,j,k+.5}^{n,\omega} \quad (4.15)$$

$$\mu_0 \frac{1 - e^{-j\omega\Delta t}}{\Delta t} H_{zi} |_{i+.5,j+.5,k}^{n+.5,\omega} = \frac{e^{-jk_y\Delta y} - 1}{\Delta y} E_{xi} |_{i+.5,j,k}^{n,\omega} - \frac{1 - e^{jk_x\Delta x}}{\Delta x} E_{yi} |_{i,j+.5,k}^{n,\omega} \quad (4.16)$$

$J_{xi} |_{i+.5,j,k}^{n+.5,\omega}$, $J_{yi} |_{i,j+.5,k}^{n+.5,\omega}$, and $J_{zi} |_{i,j,k+.5}^{n+.5,\omega}$ are the polarization currents and are, in general, frequency dependent and anisotropic. Their update equations can be written out as complicated averages in time and space of the surrounding electric fields and electric currents which we apply from the work of *Lee and Kalluri* (1999) differing only in that we co-locate the vector electric currents with the vector electric fields, e.g. \vec{J}_x is collocated with \vec{E}_x , as mentioned prior. The time, spatial harmonic form of the FDTD equations are

$$\begin{aligned} J_{xi} |_{i+.5,j,k}^{n+.5,\omega} = & e^{-j\omega\Delta t} a_{11} J_{xi} |_{i+.5,j,k}^{n+.5,\omega} + e^{-j\omega\Delta t} a_{12} \frac{1 + e^{jk_y\Delta y}}{2} \frac{e^{-jk_x\Delta x} + 1}{2} J_{yi} |_{i,j+.5,k}^{n+.5,\omega} \\ & + e^{-j\omega\Delta t} a_{13} \frac{1 + e^{jk_z\Delta z}}{2} \frac{e^{-jk_x\Delta x} + 1}{2} J_{zi} |_{i,j,k+.5}^{n+.5,\omega} \\ & + k_{11} E_{xi} |_{i+.5,j,k}^{n,\omega} + k_{12} \frac{1 + e^{jk_y\Delta y}}{2} \frac{e^{-jk_x\Delta x} + 1}{2} E_{yi} |_{i,j+.5,k}^{n,\omega} \\ & + k_{13} \frac{1 + e^{jk_z\Delta z}}{2} \frac{e^{-jk_x\Delta x} + 1}{2} E_{zi} |_{i,j,k+.5}^{n,\omega} \end{aligned} \quad (4.17)$$

$$J_{yi} |_{i,j+.5,k}^{n+.5,\omega} = e^{-j\omega\Delta t} a_{21} \frac{e^{-jk_y\Delta y} + 1}{2} \frac{1 + e^{jk_x\Delta x}}{2} J_{xi} |_{i+.5,j,k}^{n+.5,\omega} + e^{-j\omega\Delta t} a_{22} J_{yi} |_{i,j+.5,k}^{n+.5,\omega}$$

$$\begin{aligned}
& + e^{-j\omega\Delta t} a_{23} \frac{1 + e^{jk_z\Delta z}}{2} \frac{e^{-jk_y\Delta y} + 1}{2} J_{zi} |_{i,j,k+.5}^{n+.5,\omega} \\
& k_{21} \frac{e^{-jk_y\Delta y} + 1}{2} \frac{1 + e^{jk_x\Delta x}}{2} E_{xi} |_{i+.5,j,k}^{n,\omega} + k_{22} E_{yi} |_{i,j+.5,k}^{n,\omega} \\
& + k_{23} \frac{1 + e^{jk_z\Delta z}}{2} \frac{e^{-jk_y\Delta y} + 1}{2} E_{zi} |_{i,j,k+.5}^{n,\omega}
\end{aligned} \tag{4.18}$$

$$\begin{aligned}
J_{zi} |_{i,j,k+.5}^{n+.5,\omega} = & e^{-j\omega\Delta t} a_{31} \frac{e^{-jk_z\Delta z} + 1}{2} \frac{1 + e^{jk_x\Delta x}}{2} J_{xi} |_{i+.5,j,k}^{n+.5,\omega} \\
& + e^{-j\omega\Delta t} a_{32} \frac{1 + e^{jk_y\Delta y}}{2} \frac{e^{-jk_z\Delta z} + 1}{2} J_{yi} |_{i,j+.5,k}^{n+.5,\omega} + e^{-j\omega\Delta t} a_{33} J_{zi} |_{i,j,k+.5}^{n+.5,\omega} \\
& k_{31} \frac{e^{-jk_z\Delta z} + 1}{2} \frac{1 + e^{jk_x\Delta x}}{2} E_{xi} |_{i+.5,j,k}^{n,\omega} \\
& + k_{32} \frac{1 + e^{jk_y\Delta y}}{2} \frac{e^{-jk_z\Delta z} + 1}{2} E_{yi} |_{i,j+.5,k}^{n,\omega} + k_{33} E_{zi} |_{i,j,k+.5}^{n,\omega}
\end{aligned} \tag{4.19}$$

The medium considered here could range from free space ($J=0$) to a linear magnetized plasma. Instead of deriving some general expression, such as (4.8), we solve for the wave number k by setting the determinant of the above system to zero for a given frequency and incident angle. We iteratively adjust k until the equality is satisfied. Isotropic media generally have two solutions for k , both of which are either propagating or evanescent. We choose the solution which, if propagating, has its Poynting vector into the PML or if evanescent, is decaying into the PML. The anisotropic medium we consider, a magnetized plasma, generally has four solutions for k , for which there are two solutions of k that each satisfy the constraint that its Poynting vector into the PML, if propagating, or is decaying into the PML, if evanescent. We must choose one of these solutions as our incident wave. This procedure is followed for each frequency, ω , and incident angle, θ and ϕ of interest.

We solve for the incident fields about the timestep, n , and grid node, $i=0, j=j_0, k=k_0$, which other than $i=0$ are arbitrary choices since we solve for the steady state field amplitudes. For isotropic media we set $E_{zi} |_{0,j_0,k_0+.5}^{n,\omega} = 1.0$ and

$H_{zi}|_{.5,j_0+.5,k_0}^{n+.5,\omega} = 0.0$; both of these fields values are arbitrary but both must be assigned values to uniquely define the incident wave. We can then explicitly solve for the other field components of the system $E_{yi}|_{0,j_0+.5,k_0}^{n,\omega} = E_{yi0}$, $E_{xi}|_{.5,j_0,k_0}^{n,\omega} = E_{xi0}$, $H_{xi}|_{0,j_0+.5,k_0+.5}^{n+.5,\omega} = H_{xi0}$, $H_{yi}|_{.5,j_0,k_0+.5}^{n+.5,\omega} = H_{yi0}$, etc. For the magnetized plasma we set $E_{zi}|_{i=0,j,k+.5}^{n,\omega} = 1.0$; this field value is arbitrary but must be assigned a value to uniquely define our incident wave. We can then explicitly solve for the other field components of the system. With our incident fields now defined, we next develop expressions for the scattered tangential boundary fields.

4.1.2 Scattered fields

To specify the scattered boundary fields we observe the following rules:

1. For the isotropic case, Snell's law requires that the reflected wave number is preserved and the reflected angle equals the incident angle.

- (a) We use equations 4.11-4.19, replacing the subscript 'i' for 'incident' with 's' for 'scattered', e.g.,

$E_{xi}|_{.5,j_0,k_0}^{n,\omega} \rightarrow E_{xs}|_{.5,j_0,k_0}^{n,\omega}$, etc., and replacing k_x , k_y , k_z with k_{xs} , k_{ys} , k_{zs} where from snell's law, $k_x = -k_{xs}$, $k_y = k_{ys}$, $k_z = k_{zs}$. We then let $H_{ys}|_{.5,j_0,k_0+.5}^{n+.5,\omega} = 1.0$. Also, since the incident field $H_{zi}|_{.5,j_0+.5,k_0}^{n+.5,\omega} = 0.0$ we have $H_{zs}|_{.5,j_0+.5,k_0}^{n+.5,\omega} = 0.0$ as well, for the isotropic case. Solving the system yields the field values for $E_{ys0}|_{0,j_0+.5,k_0}^{n,\omega}$, $E_{zs0}|_{0,j_0,k_0+.5}^{n,\omega}$ which are denoted as \overline{E}_{ys0} , \overline{E}_{zs0} . And since in general $H_{ys1}|_{.5,j_0,k_0+.5}^{n+.5,\omega} \neq 1.0$ we obtain

$$E_{ys}|_{0,j_0+.5,k_0}^{n,\omega} = \overline{E}_{ys0} H_{ys}|_{.5,j_0,k_0+.5}^{n+.5,\omega}$$

$$E_{zs}|_{0,j_0,k_0+.5}^{n,\omega} = \overline{E}_{zs0} H_{ys}|_{.5,j_0,k_0+.5}^{n+.5,\omega}$$

It is then easy to show that the total electric fields can be written as

$$E_{yt}|_{0,j_0+.5,k_0}^{n,\omega} = E_{yi}|_{0,j_0+.5,k_0}^{n,\omega} + \overline{E}_{ys0} \left[H_{yt}|_{.5,j_0,k_0+.5}^{n+.5,\omega} - H_{yi}|_{i=.5,j_0,k_0+.5}^{n+.5,\omega} \right]$$

Similar expressions are trivially obtained for $E_{zt} |_{0,j_0,k_0+.5}^{n,\omega}$, $J_{yt} |_{0,j_0+.5,k_0}^{n+.5,\omega}$, and $J_{zt} |_{0,j_0,k_0+.5}^{n+.5,\omega}$.

2. The magnetized plasma case is more complicated. When reflected from the PML, the single mode incident wave, be it a Right-Hand Elliptically Polarized (RHEP) or Left-Hand Elliptically Polarized (LHEP) wave, can couple into both the LHEP and RHEP reflected modes [Ratcliffe, 1959]. Also, because this is an anisotropic medium, even though Snell's law is satisfied, the angle of incidence does not necessarily equal the angle of reflection. This is because the reflected wave number k is a function of propagation direction, θ and ϕ , and wave polarization.

- (a) For the two scattered modes, with k -vectors, \vec{k}_{s1} and \vec{k}_{s2} , Snell's law requires $k_y = k_{ys1} = k_{ys2}$, $k_z = k_{zs2} = k_{zs1}$. This allows us to determine, k_{xs1} , and k_{xs2} . To calculate k_{xs1} we use equations 4.11-4.19, replacing k_x , k_y , k_z with k_{xs1} , k_{ys1} , k_{zs1} , and set the determinant of the system to zero. We solve for k_{xs1} with the constraints that the polarization of the resultant wave is RHEP and the wave energy is either directed out of the PML if propagating or decaying out of the PML if evanescent. We do the same for solving k_{xs2} with constraints that the polarization of the resultant wave is LHEP and the wave energy is directed out of the PML if propagating or decaying out of the PML if evanescent.

- (b) We use equations 4.11-4.19, replacing the subscript 'i' for 'incident' with 's1' for 'scattered 1' (RHEP), e.g. $E_{xi} |_{.5,j_0,k_0}^{n,\omega} \rightarrow E_{xs1} |_{.5,j_0,k_0}^{n,\omega}$, etc, and replacing k_x , k_y , k_z with k_{xs1} , k_{ys1} , k_{zs1} . If we assume that $H_{ys1} |_{.5,j_0,k_0+.5}^{n+.5,\omega} = 1.0$, solving the system yields the field values for

$$H_{zs1} |_{.5,j_0+.5,k_0}^{n+.5,\omega}, E_{ys1} |_{0,j_0+.5,k_0}^{n,\omega}, E_{zs1} |_{0,j_0,k_0+.5}^{n,\omega}, J_{ys1} |_{0,j_0+.5,k_0}^{n+.5,\omega}, J_{zs1} |_{0,j_0,k_0+.5}^{n+.5,\omega} \text{ we'll denote as } \overline{H}_{zs10}, \overline{E}_{ys10}, \overline{E}_{zs10}, \overline{J}_{ys10}, \overline{J}_{zs10}$$

and since in general $H_{ys1} |_{.5,j_0,k_0+.5}^{n+.5,\omega} \neq 1.0$ we obtain

$$H_{zs1} |_{.5,j_0+.5,k_0}^{n+.5,\omega} = \overline{H}_{zs10} H_{ys1} |_{.5,j_0,k_0+.5}^{n+.5,\omega}$$

$$E_{ys1} \big|_{0,j_0+.5,k_0}^{n,\omega} = \overline{E}_{ys10} H_{ys1} \big|_{.5,j_0,k_0+.5}^{n+.5,\omega}$$

$$E_{zs1} \big|_{0,j_0,k_0+.5}^{n,\omega} = \overline{E}_{zs10} H_{ys1} \big|_{.5,j_0,k_0+.5}^{n+.5,\omega}$$

$$J_{ys1} \big|_{0,j_0+.5,k_0}^{n+.5,\omega} = \overline{J}_{ys10} H_{ys1} \big|_{.5,j_0,k_0+.5}^{n+.5,\omega}$$

$$J_{zs1} \big|_{0,j_0,k_0+.5}^{n+.5,\omega} = \overline{J}_{zs10} H_{ys1} \big|_{.5,j_0,k_0+.5}^{n+.5,\omega}$$

- (c) Once again, using equations 4.11-4.19, replacing the subscript 'i' for 'incident' with 's2' for 'scattered 2' (LHEP), e.g., $E_{xi} \big|_{.5,j_0,k_0}^{n,\omega} \rightarrow E_{xs2} \big|_{.5,j_0,k_0}^{n,\omega}$, etc, and replacing k_x , k_y , k_z with k_{xs2} , k_{ys2} , k_{zs2} . Continuing the same procedure as (b) we obtain

$$H_{zs2} \big|_{.5,j_0+.5,k_0}^{n+.5,\omega} = \overline{H}_{zs20} H_{ys2} \big|_{.5,j_0,k_0+.5}^{n+.5,\omega}$$

$$E_{ys2} \big|_{0,j_0+.5,k_0}^{n,\omega} = \overline{E}_{ys20} H_{ys2} \big|_{.5,j_0,k_0+.5}^{n+.5,\omega}$$

$$E_{zs2} \big|_{0,j_0,k_0+.5}^{n,\omega} = \overline{E}_{zs20} H_{ys2} \big|_{.5,j_0,k_0+.5}^{n+.5,\omega}$$

$$J_{ys2} \big|_{0,j_0+.5,k_0}^{n+.5,\omega} = \overline{J}_{ys20} H_{ys2} \big|_{.5,j_0,k_0+.5}^{n+.5,\omega}$$

$$J_{zs2} \big|_{0,j_0,k_0+.5}^{n+.5,\omega} = \overline{J}_{zs20} H_{ys2} \big|_{.5,j_0,k_0+.5}^{n+.5,\omega}$$

- (d) The scattered magnetic fields are the sum of the magnetic fields of the two scattered waves

$$\begin{pmatrix} H_{zs} \big|_{.5,j_0+.5,k_0}^{n+.5,\omega} \\ H_{ys} \big|_{.5,j_0,k_0+.5}^{n+.5,\omega} \end{pmatrix} = \begin{pmatrix} H_{zs1} \big|_{.5,j_0+.5,k_0}^{n+.5,\omega} + H_{zs2} \big|_{.5,j_0+.5,k_0}^{n+.5,\omega} \\ H_{ys1} \big|_{.5,j_0,k_0+.5}^{n+.5,\omega} + H_{ys2} \big|_{.5,j_0,k_0+.5}^{n+.5,\omega} \end{pmatrix}$$

$$\begin{aligned}
&= \begin{pmatrix} \overline{H}_{zs10} & \overline{H}_{zs20} \\ 1 & 1 \end{pmatrix} \begin{pmatrix} H_{ys1} |_{.5,j_0,k_0+.5}^{n+.5,\omega} \\ H_{ys2} |_{.5,j_0,k_0+.5}^{n+.5,\omega} \end{pmatrix} \\
&= T^{-1} \begin{pmatrix} H_{ys1} |_{.5,j_0,k_0+.5}^{n+.5,\omega} \\ H_{ys2} |_{.5,j_0,k_0+.5}^{n+.5,\omega} \end{pmatrix} \quad (4.20)
\end{aligned}$$

Therefore

$$\begin{aligned}
\begin{pmatrix} H_{ys1} |_{.5,j_0,k_0+.5}^{n+.5,\omega} \\ H_{ys2} |_{.5,j_0,k_0+.5}^{n+.5,\omega} \end{pmatrix} &= T \begin{pmatrix} H_{zs} |_{.5,j_0+.5,k_0}^{n+.5,\omega} \\ H_{ys} |_{.5,j_0,k_0+.5}^{n+.5,\omega} \end{pmatrix} \\
&= \begin{pmatrix} t_{11} & t_{12} \\ t_{21} & t_{22} \end{pmatrix} \begin{pmatrix} H_{zs} |_{.5,j_0+.5,k_0}^{n+.5,\omega} \\ H_{ys} |_{.5,j_0,k_0+.5}^{n+.5,\omega} \end{pmatrix} \quad (4.21)
\end{aligned}$$

The scattered electric fields are the sum of electric fields of the two scattered waves. Starting with $E_{ys} |_{0,j_0+.5,k_0}^{n,\omega}$ we have

$$\begin{aligned}
E_{ys} |_{0,j_0+.5,k_0}^{n,\omega} &= E_{ys1} |_{0,j_0+.5,k_0}^{n,\omega} + E_{ys2} |_{0,j_0+.5,k_0}^{n,\omega} \\
&= \begin{pmatrix} \overline{E}_{ys10} & \overline{E}_{ys20} \end{pmatrix} \begin{pmatrix} H_{ys1} |_{.5,j_0,k_0+.5}^{n+.5,\omega} \\ H_{ys2} |_{.5,j_0,k_0+.5}^{n+.5,\omega} \end{pmatrix} \\
&= \begin{pmatrix} \overline{E}_{ys10} & \overline{E}_{ys20} \end{pmatrix} \begin{pmatrix} t_{11} & t_{12} \\ t_{21} & t_{22} \end{pmatrix} \begin{pmatrix} H_{zs} |_{.5,j_0+.5,k_0}^{n+.5,\omega} \\ H_{ys} |_{.5,j_0,k_0+.5}^{n+.5,\omega} \end{pmatrix} \\
&= (\overline{E}_{ys10}t_{11} + \overline{E}_{ys20}t_{21})H_{zs} |_{.5,j_0+.5,k_0}^{n+.5,\omega} \\
&\quad + (\overline{E}_{ys10}t_{12} + \overline{E}_{ys20}t_{22})H_{ys} |_{.5,j_0,k_0+.5}^{n+.5,\omega} \\
&= (\overline{E}_{ys10}t_{11} + \overline{E}_{ys20}t_{21})(H_{zt} |_{.5,j_0+.5,k_0}^{n+.5,\omega} - H_{zi} |_{.5,j_0+.5,k_0}^{n+.5,\omega}) \\
&\quad + (\overline{E}_{ys10}t_{12} + \overline{E}_{ys20}t_{22})(H_{yt} |_{.5,j_0,k_0+.5}^{n+.5,\omega} - H_{yi} |_{.5,j_0,k_0+.5}^{n+.5,\omega}) \quad (4.22)
\end{aligned}$$

Therefore we can write the total electric field as

$$\begin{aligned}
E_{yt} |_{0,j_0+.5,k_0}^{n,\omega} &= E_{yi} |_{0,j_0+.5,k_0}^{n,\omega} \\
&\quad + (\overline{E}_{ys10}t_{11} + \overline{E}_{ys20}t_{21})(H_{zt} |_{.5,j_0+.5,k_0}^{n+.5,\omega} - H_{zi} |_{.5,j_0+.5,k_0}^{n+.5,\omega}) \\
&\quad + (\overline{E}_{ys10}t_{12} + \overline{E}_{ys20}t_{22})(H_{yt} |_{.5,j_0,k_0+.5}^{n+.5,\omega} - H_{yi} |_{.5,j_0,k_0+.5}^{n+.5,\omega})
\end{aligned}$$

(4.23)

Similar expressions are trivially obtained for $E_{zt} \big|_{0,j_0,k_0+.5}^{n,\omega}$, $J_{yt} \big|_{0,j_0+.5,k_0}^{n+.5,\omega}$, and $J_{zt} \big|_{0,j_0,k_0+.5}^{n+.5,\omega}$

We have developed a procedure to fully specify the total electric field and the total electric current (anisotropic media) at the $i = 0$ boundary of Figure 4.1b by our incident fields and the total magnetic fields just inside the boundary. In Section 4.2 we specify the equations within the space of Figure 4.1b for $i > 0$ as well as the boundary conditions at the termination of the PML.

4.2 PML equations and Termination Boundary Conditions

We now construct the time harmonic equations for the total fields in the space depicted in Figure 4.1b which includes the PML. This space, for any given incident wave, produces scattered fields, and with this information a reflection coefficient can be calculated. We have specified the boundary conditions at $i = 0$. We define the PML to begin at $i = 1$, while the medium that the PML is matching exists at $i < 1$. We therefore assume non-zero PML coefficients, i.e., for $i \geq 1$, in only the \hat{x} -direction. The y and z dependence of the fields within the PML are well defined since Snell's Law requires the PML fields to share the same y and z phase variation as the incident wave. However, within the space, PML included, the x dependence of the fields cannot be explicitly specified since in the \hat{x} -direction we have reflections, decay, etc. Inserting the harmonic time and spatial relationships (excluding the x -dependent relationship) into the PML FDTD equations we obtain the set of equations displayed in Sections 4.2.1-4.2.9. Note that we use the field variables E_{xt} , E_{yt} , E_{zt} , H_{xt} , H_{yt} , H_{zt} , etc. where the 't' simply indicates that the quantities are total fields.

4.2.1 $E_x, T + 1$ equations

$$\begin{aligned} \bar{\varepsilon} \frac{e^{j\omega\Delta t} - 1}{\Delta t} E_{xt} \big|_{i+.5, j, k}^{n, \omega} + J_{xt} \big|_{i+.5, j_0, k_0}^{n+.5, \omega} &= -\frac{1 - e^{jk_z\Delta z}}{\Delta z} H_{yt} \big|_{i+.5, j_0, k_0+.5}^{n+.5, \omega} \\ &\quad + \frac{1 - e^{jk_y\Delta y}}{\Delta y} H_{zt} \big|_{i+.5, j_0+.5, k_0}^{n+.5, \omega} \end{aligned} \quad (4.24)$$

4.2.2 E_y, T equations

CCO-PML

$$\begin{aligned} \bar{\varepsilon} \frac{e^{j\omega\Delta t} - 1}{\Delta t} E_{yt} \big|_{i, j_0+.5, k_0}^{n, \omega} + J_{yt} \big|_{i, j_0+.5, k_0}^{n+.5, \omega} &= \frac{1 - e^{jk_z\Delta z}}{\Delta z} H_{xt} \big|_{i, j_0+.5, k_0+.5}^{n+.5, \omega} \\ - \left[(1 - b_{x0}(i)) \frac{H_{zt} \big|_{i+.5, j_0+.5, k_0}^{n+.5, \omega} - H_{zt} \big|_{i-.5, j_0+.5, k_0}^{n+.5, \omega}}{\Delta x} - \sum_{m=1}^M b_{xm}(i) \Psi_{H_{zt}}^{x, m} \big|_{i, j_0+.5, k_0}^{n+.5, \omega} \right] \end{aligned} \quad (4.25)$$

KPML

$$\begin{aligned} \bar{\varepsilon} \frac{e^{j\omega\Delta t} - 1}{\Delta t} E_{yt} \big|_{i, j_0+.5, k_0}^{n, \omega} + J_{yt} \big|_{i, j_0+.5, k_0}^{n+.5, \omega} &= \frac{1 - e^{jk_z\Delta z}}{\Delta z} H_{xt} \big|_{i, j_0+.5, k_0+.5}^{n+.5, \omega} \\ &\quad - (1 - b_{x0}(i)) \Psi_{H_{zt}}^x \big|_{i, j_0+.5, k_0}^{n+.5, \omega} \end{aligned} \quad (4.26)$$

4.2.3 E_z, T equations

CCO-PML

$$\begin{aligned} \bar{\varepsilon} \frac{e^{j\omega\Delta t} - 1}{\Delta t} E_{zt} \big|_{i, j_0, k_0+.5}^{n, \omega} + J_{zt} \big|_{i, j_0, k_0+.5}^{n+.5, \omega} &= -\frac{1 - e^{jk_y\Delta y}}{\Delta y} H_{xt} \big|_{i, j_0+.5, k_0+.5}^{n+.5, \omega} \\ + \left[(1 - b_{x0}(i)) \frac{H_{yt} \big|_{i+.5, j_0, k_0+.5}^{n+.5, \omega} - H_{yt} \big|_{i-.5, j_0, k_0+.5}^{n+.5, \omega}}{\Delta x} - \sum_{m=1}^M b_{xm}(i) \Psi_{H_{yt}}^{x, m} \big|_{i, j_0, k_0+.5}^{n+.5, \omega} \right] \end{aligned} \quad (4.27)$$

KPML

$$\begin{aligned} \bar{\epsilon} \frac{e^{j\omega\Delta t} - 1}{\Delta t} E_{zt} \big|_{i,j_0,k_0+.5}^{n,\omega} + J_{zt} \big|_{i,j_0,k_0+.5}^{n+.5,\omega} &= -\frac{1 - e^{jk_y\Delta y}}{\Delta y} H_{xt} \big|_{i,j_0+.5,k_0+.5}^{n+.5,\omega} \\ &\quad + (1 - b_{x0}(i)) \Psi_{H_{yt}}^x \big|_{i,j_0,k_0+.5}^{n+.5,\omega} \end{aligned} \quad (4.28)$$

4.2.4 H_x, T equations

$$\mu_0 \frac{1 - e^{-j\omega\Delta t}}{\Delta t} H_{xt} \big|_{i,j_0+.5,k_0+.5}^{n+.5,\omega} = \frac{e^{-jk_z\Delta z} - 1}{\Delta z} E_{yt} \big|_{i,j_0+.5,k_0}^{n,\omega} - \frac{e^{-jk_y\Delta y} - 1}{\Delta y} E_{zt} \big|_{i,j_0,k_0+.5}^{n,\omega} \quad (4.29)$$

4.2.5 $H_y, T + 1$ equations

For $i = 0$ (Just outside the PML)

$$\mu_0 \frac{1 - e^{-j\omega\Delta t}}{\Delta t} H_{yt} \big|_{.5,j,k+.5}^{n+.5,\omega} = -\frac{e^{-jk_z\Delta z} - 1}{\Delta z} E_{xt} \big|_{.5,j,k}^{n,\omega} + \frac{E_{zt} \big|_{1,j,k+.5}^{n,\omega} - E_{zt} \big|_{0,j,k+.5}^{n,\omega}}{\Delta x} \quad (4.30)$$

where the expression for $E_{zt} \big|_{0,j_0,k_0+.5}^{n,\omega}$ is derived in the previous section.

For $i \geq 1$ (Inside the PML)

CCO-PML

$$\begin{aligned} \mu_0 \frac{1 - e^{-j\omega\Delta t}}{\Delta t} H_{yt} \big|_{i+.5,j_0,k_0+.5}^{n+.5,\omega} &= -\frac{e^{-jk_z\Delta z} - 1}{\Delta z} E_{xt} \big|_{i+.5,j_0,k_0}^{n,\omega} \\ + \left[(1 - b_{x0}(i + .5)) \frac{E_{zt} \big|_{i+1,j_0,k_0+.5}^{n,\omega} - E_{zt} \big|_{i,j_0,k_0+.5}^{n,\omega}}{\Delta x} - \sum_{m=1}^M b_{xm}(i + .5) \Psi_{E_{zt}}^{x,m} \big|_{i+.5,j_0,k_0+.5}^{n,\omega} \right] \end{aligned} \quad (4.31)$$

KPML

$$\begin{aligned} \mu_0 \frac{1 - e^{-j\omega\Delta t}}{\Delta t} H_{yt} \big|_{i+.5, j_0, k_0+.5}^{n+.5, \omega} &= -\frac{e^{-jk_z\Delta z} - 1}{\Delta z} E_{xt} \big|_{i+.5, j_0, k_0}^{n, \omega} \\ &\quad + (1 - b_{x0}(i + .5)) \Psi_{E_{zt}}^x \big|_{i+.5, j_0, k_0+.5}^{n, \omega} \end{aligned} \quad (4.32)$$

Since we have PEC for $i \geq T + 1$ all tangential electric fields at $i = T + 1$ are zero, thus $E_{zt} \big|_{T+1, j_0, k_0+.5}^{n, \omega} = 0.0$

4.2.6 H_z , $T + 1$ equations

For $i = 0$ (Just outside the PML)

$$\mu_0 \frac{1 - e^{-j\omega\Delta t}}{\Delta t} H_{zt} \big|_{.5, j_0+.5, k_0}^{n+.5, \omega} = \frac{e^{-jk_y\Delta y} - 1}{\Delta y} E_{xt} \big|_{.5, j_0, k_0}^{n, \omega} - \frac{E_{yt} \big|_{1, j_0+.5, k_0}^{n, \omega} - E_{yt} \big|_{0, j_0+.5, k_0}^{n, \omega}}{\Delta x} \quad (4.33)$$

where the expression for the boundary field $E_{yt} \big|_{0, j_0+.5, k_0}^{n, \omega}$ is derived in the previous section.

For $i \geq 1$ (Inside the PML)

CCO-PML

$$\begin{aligned} \mu_0 \frac{1 - e^{-j\omega\Delta t}}{\Delta t} H_{zt} \big|_{i+.5, j_0+.5, k_0}^{n+.5, \omega} &= \frac{e^{-jk_y\Delta y} - 1}{\Delta y} E_{xt} \big|_{i+.5, j_0, k_0}^{n, \omega} \\ &\quad - \left[(1 - b_{x0}(i + .5)) \frac{E_{yt} \big|_{i+1, j_0+.5, k_0}^{n, \omega} - E_{yt} \big|_{i, j_0+.5, k_0}^{n, \omega}}{\Delta x} - \sum_{m=1}^M b_{xm}(i + .5) \Psi_{E_{yt}}^{x, m} \big|_{i+.5, j_0+.5, k_0}^{n, \omega} \right] \end{aligned} \quad (4.34)$$

KPML

$$\mu_0 \frac{1 - e^{-j\omega\Delta t}}{\Delta t} H_{zt} \big|_{i+.5, j_0+.5, k_0}^{n+.5, \omega} = \frac{e^{-jk_y\Delta y} - 1}{\Delta y} E_{xt} \big|_{i+.5, j_0, k_0}^{n, \omega}$$

$$-(1 - b_{x0}(i + .5))\Psi_{E_{yt}}^x \big|_{i+.5, j_0+.5, k_0}^{n, \omega} \quad (4.35)$$

Since we have PEC for $i \geq T + 1$ all tangential electric fields at $i = T + 1$ are zero, thus $E_{yt} \big|_{T+1, j_0+.5, k_0}^{n, \omega} = 0.0$.

4.2.7 J_x , $T+1$ equations

The general equation used is

$$\begin{aligned} J_{xt} \big|_{i+.5, j_0, k_0}^{n+.5, \omega} = & e^{-j\omega\Delta t} a_{11} J_{xt} \big|_{i+.5, j_0, k_0}^{n+.5, \omega} \\ & + e^{-j\omega\Delta t} a_{12} \frac{1 + e^{jk_y\Delta y}}{2} \frac{(J_{yt} \big|_{i, j_0+.5, k_0}^{n+.5, \omega} + J_{yt} \big|_{i+1, j_0+.5, k_0}^{n+.5, \omega})}{2} \\ & + e^{-j\omega\Delta t} a_{13} \frac{1 + e^{jk_z\Delta z}}{2} \frac{(J_{zt} \big|_{i, j_0, k_0+.5}^{n+.5, \omega} + J_{zt} \big|_{i+1, j_0, k_0+.5}^{n+.5, \omega})}{2} \\ & + k_{11} E_{xt} \big|_{i+.5, j_0, k_0}^{n, \omega} \\ & + k_{12} \frac{1 + e^{jk_y\Delta y}}{2} \frac{(E_{yt} \big|_{i, j_0+.5, k_0}^{n, \omega} + E_{yt} \big|_{i+1, j_0+.5, k_0}^{n, \omega})}{2} \\ & + k_{13} \frac{1 + e^{jk_z\Delta z}}{2} \frac{(E_{zt} \big|_{i, j_0, k_0+.5}^{0, \omega} + E_{zt} \big|_{i+1, j_0, k_0+.5}^{0, \omega})}{2} \end{aligned} \quad (4.36)$$

To solve $J_{xt} \big|_{.5, j_0, k_0}^{n+.5, \omega}$ requires the boundary fields at $i=0$, $E_{yt} \big|_{0, j_0+.5, k_0}^{n, \omega}$, $E_{zt} \big|_{0, j_0, k_0+.5}^{n, \omega}$, $J_{yt} \big|_{0, j_0+.5, k_0}^{n+.5, \omega}$, $J_{zt} \big|_{0, j_0, k_0+.5}^{n+.5, \omega}$. The boundary conditions at $i = T + 1$ are those of PEC, all tangential electric fields are zero, thus $E_{yt} \big|_{T+1, j_0+.5, k_0}^{n, \omega} = E_{zt} \big|_{T+1, j_0, k_0+.5}^{n, \omega} = 0.0$. In addition, we'll enforce $J_{yt} \big|_{T+1, j_0+.5, k_0}^{n+.5, \omega} = J_{zt} \big|_{T+1, j_0, k_0+.5}^{n+.5, \omega} = 0.0$

4.2.8 J_y , T equations

The general equation used is

$$J_{yt} \big|_{i, j_0+.5, k_0}^{n+.5, \omega} = e^{-j\omega\Delta t} a_{21} \frac{e^{-jk_y\Delta y} + 1}{2} \frac{(J_{xt} \big|_{i+.5, j_0, k_0}^{n+.5, \omega} + J_{xt} \big|_{i-.5, j_0, k_0}^{n+.5, \omega})}{2}$$

$$\begin{aligned}
& +e^{-j\omega\Delta t}a_{22}J_{yt}|_{i,j_0+.5,k_0}^{n+.5,\omega} \\
& +e^{-j\omega\Delta t}a_{23}\frac{1+e^{jk_z\Delta z}}{2}\frac{e^{-jk_y\Delta y}+1}{2}J_{zt}|_{i,j_0,k_0+.5}^{n+.5,\omega} \\
& +k_{21}\frac{e^{-jk_y\Delta y}+1}{2}\frac{(E_{xt}|_{i+.5,j_0,k_0}^{n,\omega}+E_{xt}|_{i-.5,j_0,k_0}^{n,\omega})}{2} \\
& +k_{22}E_{yt}|_{i,j_0+.5,k_0}^{n,\omega} \\
& +k_{23}\frac{1+e^{jk_z\Delta z}}{2}\frac{e^{-jk_y\Delta y}+1}{2}E_{zt}|_{i,j_0,k_0+.5}^{n,\omega}
\end{aligned} \tag{4.37}$$

4.2.9 J_z , T equations

The general equation used is

$$\begin{aligned}
J_{zt}|_{i,j_0,k_0+.5}^{n+.5,\omega} = & e^{-j\omega\Delta t}a_{31}\frac{e^{-jk_z\Delta z}+1}{2}\frac{(J_{xt}|_{i+.5,j_0,k_0}^{n+.5,\omega}+J_{xt}|_{i-.5,j_0,k_0}^{n+.5,\omega})}{2} \\
& +e^{-j\omega\Delta t}a_{32}\frac{1+e^{jk_y\Delta y}}{2}\frac{e^{-jk_z\Delta z}+1}{2}J_{yt}|_{i,j_0+.5,k_0}^{n+.5,\omega} \\
& +e^{-j\omega\Delta t}a_{33}J_{zt}|_{i,j_0,k_0+.5}^{n+.5,\omega} \\
& +k_{31}\frac{e^{-jk_z\Delta z}+1}{2}\frac{(E_{xt}|_{i+.5,j_0,k_0}^{n,\omega}+E_{xt}|_{i-.5,j_0,k_0}^{n,\omega})}{2} \\
& +k_{32}\frac{1+e^{jk_y\Delta y}}{2}\frac{e^{-jk_z\Delta z}+1}{2}E_{yt}|_{i,j_0+.5,k_0}^{n,\omega} \\
& +k_{33}E_{zt}|_{i,j_0,k_0+.5}^{n,\omega}
\end{aligned} \tag{4.38}$$

4.2.10 $\Psi_{Eyt}^{x,m}, \Psi_{Ezt}^{x,m}, \Psi_{Hyt}^{x,m}, \Psi_{Hzt}^{x,m}$ for CCO-PML

For the CCO-PML the time harmonic expression for the difference equation of $\Psi = u(t)\alpha e^{-\alpha t} * F$ is

$$|\Psi|^n - e^{-\alpha\Delta t}|\Psi|^{n-1} = |F|^n [1 - e^{-\alpha\Delta t}] \tag{4.39}$$

whose time harmonic expression is then

$$\Psi|^n [1 - e^{-\alpha\Delta t} e^{-i\omega\Delta t}] = F|^n [1 - e^{-\alpha\Delta t}] \quad (4.40)$$

where F is any time domain function, e.g., $\partial H_{zt}/\partial x$. In our case, aside from different complex amplitude valued fields, the time domain function is $F = e^{-j\omega t}$, since we are assuming single frequency fields. The quantity

$$\Psi_{H_{zt}}^{x,m} = u(t)\alpha_{xm}(i)e^{-\alpha_{xm}(i)t} * \frac{\partial H_{zt}}{\partial x} \quad (4.41)$$

is therefore

$$\begin{aligned} & \Psi_{H_{zt}}^{x,m} |_{i,j_0+.5,k_0}^{n+.5,\omega} [1 - e^{-\alpha_{xm}(i)\Delta t} e^{-i\omega\Delta t}] = \\ & \frac{H_{zt} |_{i+.5,j_0+.5,k_0}^{n+.5,\omega} - H_{zt} |_{i-.5,j_0+.5,k_0}^{n+.5,\omega}}{\Delta x} [1 - e^{-\alpha_{xm}(i)\Delta t}] \end{aligned} \quad (4.42)$$

The quantities $\Psi_{E_{yt}}^{x,m} |_{i+.5,j_0+.5,k_0}^{n,\omega}$, $\Psi_{E_{zt}}^{x,m} |_{i+.5,j_0,k_0+.5}^{n,\omega}$, and $\Psi_{H_{yt}}^{x,m} |_{i,j_0,k_0+.5}^{n+.5,\omega}$ all have a similar form.

4.2.11 $\Psi_{E_{yt}}^x, \Psi_{E_{zt}}^x, \Psi_{H_{yt}}^x, \Psi_{H_{zt}}^x$ for KPML

For the KPML the finite-difference time-domain form of (3.9) for $\Psi_{H_{zt}}^x$ would be

$$\begin{aligned} & \frac{1 - e^{-j\omega\Delta t}}{\Delta t} \left[1 + \frac{1 + e^{-i2\omega\Delta t} - 2e^{-i\omega\Delta t}}{\omega_0^2(\Delta t)^2} \right] \\ & \frac{H_{zt} |_{i+.5,j_0+.5,k_0}^{n+.5,\omega} - H_{zt} |_{i-.5,j_0+.5,k_0}^{n+.5,\omega}}{\Delta x} = \frac{1 - e^{-j\omega\Delta t}}{\Delta t} \\ & \left[1 + \frac{1 + e^{-i2\omega\Delta t} - 2e^{-i\omega\Delta t}}{\omega_0^2(\Delta t)^2} \right] \Psi_{H_{zt}}^x |_{i,j_0+.5,k_0}^{n+.5,\omega} \\ & - \sigma_x(i)(\Delta r)^2 \left(\frac{e^{-jk_y\Delta y} e^{-i\omega\Delta t} + e^{jk_y\Delta y} e^{-i\omega\Delta t} - 2}{(\Delta y)^2} \right) \end{aligned}$$

$$\begin{aligned}
& \Psi_{H_{zt}}^x |_{i,j_0+.5,k_0}^{n+.5,\omega} + 4 \frac{1 + e^{-i2\omega\Delta t} - 2e^{-i\omega\Delta t}}{\omega_c^2(\Delta t)^2} \\
& \left[\frac{\Psi_{H_{zt}}^x |_{i+1,j_0+.5,k_0}^{n+.5,\omega} e^{-i\omega\Delta t}}{\left(\frac{1}{1-b_{x0}(i)}\right)^2(\Delta x)^2} + \right. \\
& \frac{\Psi_{H_{zt}}^x |_{i-1,j_0+.5,k_0}^{n+.5,\omega} e^{-i\omega\Delta t} - 2\Psi_{H_{zt}}^x |_{i,j_0+.5,k_0}^{n+.5,\omega}}{\left(\frac{1}{1-b_{x0}(i)}\right)^2(\Delta x)^2} \\
& \left. + \frac{e^{-jk_y\Delta y} e^{-i\omega\Delta t} + e^{jk_y\Delta y} e^{-i\omega\Delta t} - 2\Psi_{H_{zt}}^x |_{i,j_0+.5,k_0}^{n+.5,\omega}}{(\Delta y)^2} \right] \Bigg)
\end{aligned} \tag{4.43}$$

The quantities $\Psi_{E_{yt}}^x |_{i+.5,j_0+.5,k_0}^{n,\omega}$, $\Psi_{E_{zt}}^x |_{i+.5,j_0,k_0+.5}^{n,\omega}$, and $\Psi_{H_{yt}}^x |_{i,j_0,k_0+.5}^{n+.5,\omega}$ all have a similar form. With the KPML, we actually must specify a few more boundary conditions at $i=0$. Because of the Laplacian in the \hat{x} -direction, the calculation for $\Psi_{H_{zt}}^x |_{1,j_0+.5,k_0}^{n+.5,\omega}$ requires $\Psi_{H_{zt}}^x |_{0,j_0+.5,k_0}^{n+.5,\omega}$ which is outside the PML at $i = 0$ and has the form

$$\Psi_{H_{zt}}^x |_{0,j_0+.5,k_0}^{n+.5,\omega} = \frac{H_{zt} |_{.5,j_0+.5,k_0}^{n+.5,\omega} - H_{zt} |_{-.5,j_0+.5,k_0}^{n+.5,\omega}}{\Delta x} \tag{4.44}$$

$H_{zt} |_{-.5,j_0+.5,k_0}^{n+.5,\omega}$ is outside our space so we must specify it in terms of incident and scattered fields inside our space

$$\begin{aligned}
H_{zt} |_{-.5,j_0+.5,k_0}^{n+.5,\omega} &= H_{zi} |_{.5,j_0+.5,k_0}^{n+.5,\omega} e^{jk_x\Delta x} \\
&+ \left[\overline{H}_{zs10} e^{jk_{xs1}\Delta x} t_{11} + \overline{H}_{zs20} e^{jk_{xs2}\Delta x} t_{21} \right] \left[H_{zt} |_{i=.5,j_0+.5,k_0}^{n+.5,\omega} - H_{zi} |_{i=.5,j_0+.5,k_0}^{n+.5,\omega} \right] \\
&+ \left[\overline{H}_{zs10} e^{jk_{xs1}\Delta x} t_{12} + \overline{H}_{zs20} e^{jk_{xs2}\Delta x} t_{22} \right] \left[H_{yt} |_{i=.5,j_0,k_0+.5}^{n+.5,\omega} - H_{yi} |_{i=.5,j_0,k_0+.5}^{n+.5,\omega} \right]
\end{aligned} \tag{4.45}$$

and similarly for $\Psi_{H_{yt}}^x |_{1,j_0,k_0+.5}^{n+.5,\omega}$, $\Psi_{E_{zt}}^x |_{1.5,j_0+.5,k_0}^{n,\omega}$, and $\Psi_{E_{yt}}^x |_{1.5,j_0,k_0+.5}^{n,\omega}$ whose expressions respectively require $\Psi_{H_{yt}}^x |_{0,j_0,k_0+.5}^{n+.5,\omega}$, $\Psi_{E_{zt}}^x |_{.5,j_0+.5,k_0}^{n,\omega}$, and $\Psi_{E_{yt}}^x |_{.5,j_0,k_0+.5}^{n,\omega}$ can be handled in the same manner.

This completes our derivation of the necessary equations and boundary conditions to describe the scattered fields from the PML, CCO-PML or KPML, for a given incident plane wave. The method allows one to solve for all fields in the

space and for most problems, i.e., when there is only one propagating reflected wave, we define the reflection coefficient using the scattered and incident magnetic fields $H_{xs}|_{i=0,j_0+.5,k_0+.5}^{n+.5,\omega}$, $H_{ys}|_{i=.5,j_0,k_0+.5}^{n+.5,\omega}$, $H_{zs}|_{i=.5,j=j_0+.5,k_0}^{n+.5,\omega}$, $H_{xi}|_{i=0,j_0+.5,k_0+.5}^{n+.5,\omega}$, $H_{yi}|_{i=.5,j_0,k_0+.5}^{n+.5,\omega}$ and $H_{zi}|_{i=.5,j=j_0+.5,k_0}^{n+.5,\omega}$ just outside the PML. We define the normalized error as

$$\begin{aligned} ||R(\omega, \theta, \phi)||_2 &= \\ \sqrt{\frac{\left|H_{xs}|_{i=0,j_0+.5,k_0+.5}^{n+.5,\omega}\right|^2 + \left|H_{ys}|_{i=.5,j_0,k_0+.5}^{n+.5,\omega}\right|^2 + \left|H_{zs}|_{i=.5,j=j_0+.5,k_0}^{n+.5,\omega}\right|^2}{\left|H_{xi}|_{i=0,j_0+.5,k_0+.5}^{n+.5,\omega}\right|^2 + \left|H_{yi}|_{i=.5,j_0,k_0+.5}^{n+.5,\omega}\right|^2 + \left|H_{zi}|_{i=.5,j=j_0+.5,k_0}^{n+.5,\omega}\right|^2}} & \quad (4.46) \end{aligned}$$

which is simply the normalized Euclidean norm of the scattered magnetic field due to the PML, i.e., the magnitude of the reflection coefficient. But for some cases, as in the magnetized plasma from Chapter 3, when there are two propagating reflected waves, we must define the reflection coefficient, $||R(\omega, \theta, \phi)||_2$, as the total reflected power over the incident power, both in the \hat{x} -direction. In either case, we can adjust the PML coefficients $[b_{x0}(i), b_{xn}(i), \alpha_{xn}(i)]$ for the CCO-PML or $[b_{x0}(i), \sigma_x(i)]$ for the KPML) until $||R(\omega, \theta, \phi)||_2$ is minimized over the frequencies, incident polarizations, and incident angles of interest. We show in Appendix C that in general $||R(\omega, \theta, \phi)||_2$ is not a convex function, meaning it has local minima, and finding a global minimum is a difficult task. We therefore, in general, minimize $||R(\omega, \theta, \phi)||_2$ over a limited parameter space.

Chapter 5

Modeling Long Path Propagation

Modeling the electromagnetic fields over a long (typically hundreds of λ) propagation path where the entire path is represented by a single static grid can be computationally prohibitive (in terms of RAM and/or CPU hours), as well as unnecessary. For the case of a transient pulse propagating along a path within a Finite-Difference Time-Domain (FDTD) grid, ahead of the transient the fields are zero, and behind the transient the fields are typically small as well. Much of the fields within the space are therefore being unnecessarily computed. The same holds true for the problem of starting up a single frequency signal (e.g., that from a radio transmitter) in an FDTD grid. Ahead of the startup transient are zero fields and behind the transient are steady-state fields, where the continuous computation of either is unnecessary. *Thevenot et al.* (1999) addressed this problem by developing a moving window technique to reduce the computational domain which captures the moving transient field region along the path. Their motivation was for modeling Very Low Frequency (VLF) propagation in the Earth-ionosphere waveguide. Typically they achieved a grid reduction factor of 10 or so. However, their window size must accommodate all significantly contributing waveguide modes which, in the extreme, can force the window to be as large as the original space. A moving window technique was also developed by *Akleman and Sevgi* (2000) at a similar time with similar computational efficiency and accuracy.

In this chapter, based on work from *Chevalier and Inan* (2007), we develop a technique in which we break up the path into segments and through the use of the

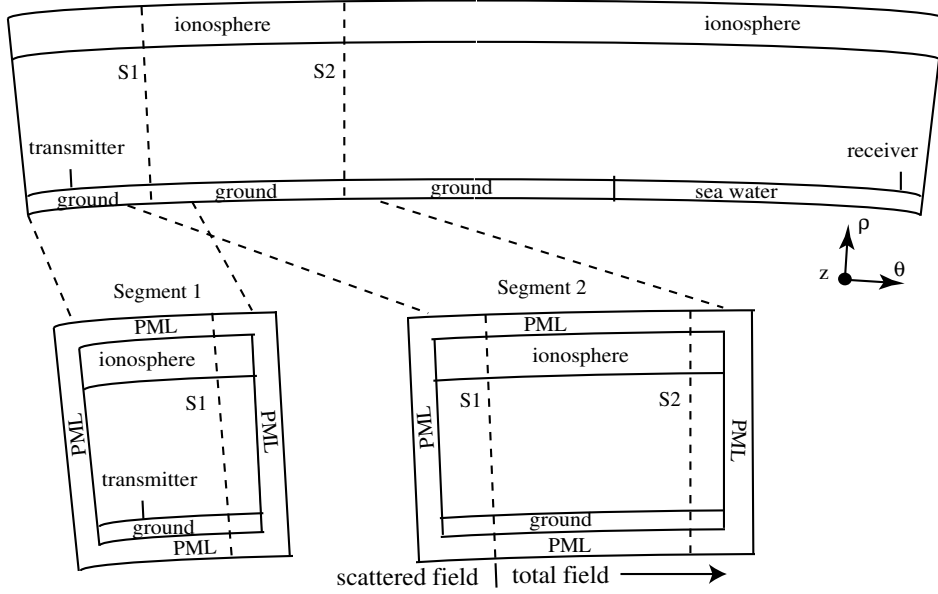


Figure 5.1: Earth-ionosphere waveguide. Segments 1 and 2 represent sequential Finite-Difference spaces in which Maxwell's equations are solved to calculate the electromagnetic fields from the transmitter to the receiver. The fields from surface ' S_1 ' are saved from Segment 1 and used as input fields to Segment 2. The fields from surface ' S_2 ' would then be used for Segment 3 (not shown), etc.

PML and the Total-field/Scattered-field technique we solve each segment sequentially. The modeling of VLF propagation in the Earth-ionosphere waveguide is used as an example to develop the idea, but the concept is general and can be applied to propagation over any long path. It turns out that any segment size, in the absence of scattering objects, will naturally accommodate all the forward propagating energy of the waves. This technique is directly applicable to FDTD and Finite-Difference Frequency-Domain (FDFD) simulations.

5.1 A Segmented Long Path Propagation Technique

Figure 5.1 represents a 2D space within which there exists a transmitter on one end and a receiver on the other. We assume the space to be 200×5000 cells, where our cell size is 500 m (30 cells per wavelength at 20 kHz). For this particular space, the ionosphere and the ground act as the reflecting boundaries of a lossy waveguide for frequencies in the VLF range (~ 20 kHz) and it is known as the Earth-ionosphere waveguide. In the past, modeling of the Earth-ionosphere waveguide was done by *Budden* (1961) using mode-theory within a uniform waveguide. *Ferguson et al.* (1989) later developed a mode-theory based computer algorithm that allowed for waveguide nonuniformities, but did not apply to scattering objects with dimensions comparable to a wavelength. The FDTD and FDFD methods, discussed below are more robust because of their ability to model inhomogeneities within the waveguide with greater ease than mode theory does. However, if we apply the FDTD technique to this waveguide space it could take more than 15,000 timesteps for all the energy of a transient pulse, originating at the transmitter, to pass through the space. Due to higher order waveguide modes it could take a similar amount of time for the space to reach steady state from the transient startup of the transmitter radiating at a single frequency in FDTD. Also for the single-frequency case, we could apply the FDFD technique, which requires an implicit solve, whose matrix solution requires 100's of GBs of RAM for a fast direct solver or up to 10's of GB's of RAM for slower iterative solvers that require preconditioning matrices to condition the system. Due to resource constraints, either in terms of RAM and/or CPU time it would be beneficial not to have to solve the whole space at once.

In order to overcome these problems, we break up the space into overlapping segments, an example of which is shown in Segment 1 and Segment 2 from Figure 5.1. Each segment is surrounded with the Perfectly Matched Layer (PML) boundary condition [*Berenger* (1994); *Chew and Weedon* (1994); *Chevalier and Inan* (2004)] to absorb outgoing waves. The idea here is to solve for the fields radiated from the transmitter in Segment 1 while saving the fields over the surface labeled ' S_1 '; over

time for FDTD or the solved complex fields for FDFD. These fields would be saved in a file on the hard disk, not in RAM. Segment 2 overlaps Segment 1 such that ' S_1 ' represents the same region in space. The fields from surface ' S_1 ' in Segment 1 then become the input source fields on the surface ' S_1 ' in Segment 2. Now in Segment 2, to the right of the input source fields at ' S_1 ', we calculate the total field while to the left we calculate only the scattered fields. The surface at ' S_1 ' in Segment 2 is known as a Total-field/Scattered-field Boundary [Taflove and Hagness, 2000]. This formulation is adapted so that any backscatter due to spatial changes in the ionospheric and/or ground parameters within the local segment are absorbed by the PML in the scattered field region. We then calculate the fields within Segment 2 using the input source fields at ' S_1 ' and save the output fields at ' S_2 '. This process is repeated for all subsequent segments until the receiver. This method is thus termed the 'Segmented Long Path' (SLP) technique.

By breaking our space up into segments we necessarily neglect interactions between scattering regions in different segments. It is thus important that a scattering region is entirely contained within a segment so that the scattering is entirely solved for within the segment. And by scattering region, we mean anything that causes backscatter, e.g. inhomogeneities in material or terrain, etc. In this context, it is important to note that the segments along the path can all be differing lengths.

In this paper we apply the SLP method to perform FDFD and pulsed FDTD simulations. To reiterate, for the FDFD SLP runs the general algorithm is

- 1) Solve fields in Segment N ; save the electric and magnetic fields and currents over the surface ' S_N '. In Segment $N + 1$ apply these fields as the incident fields at the total-field/scattered-field boundary, i.e., surface ' S_N ' in Segment $N + 1$.
- 2) Let $N = N + 1$, repeat procedure by going back to 1).

Likewise, for the pulsed FDTD SLP runs the general algorithm is

- 1) Solve fields over time in Segment N ; when the fields at ' S_N ' exceed some threshold (set by user) save the electric and magnetic fields and currents over the surface ' S_N ' (in a file on hard disk) over the remaining duration of the run. In Segment $N + 1$ apply these fields as the incident fields at the total-field/scattered-field boundary, i.e., surface ' S_N ' in Segment $N + 1$.
- 2) Let $N = N + 1$, repeat procedure by going back to 1).

These are general algorithms independent of the order and the type of finite-difference methods being applied. To properly solve the particular finite-difference equations at the total-field/scattered-field boundary at the surface ' S_N ' in Segment $N + 1$, then one must save all the fields necessary in the prior Segment N , at surface ' S_N ' to fully specify the incident fields. The fields at surface ' S_N ' must be saved over a volume of space which encompasses the cross section of the space and typically a few cells of thickness along the path direction (e.g. 2 cells for 2nd order spatial differencing, 4 cells for 4th order spatial differencing, etc).

Each segment, because there is overlap between segments, has extra RAM overhead proportional to the total length, in cells, of the overlap regions, $L_{overlap}$. For cases in this chapter $L_{overlap} = 40$ cells. For our larger numerical tests, we will have each segment be 1000 cells long and thus the percentage of extra RAM from overlap is typically small.

5.2 Numerical Results and Discussion

We now present some numerical simulations of the SLP technique for both the FDTD and the FDFD techniques applied to the same propagation path in the Earth-ionosphere waveguide. Our space consists of a 2D grid in cylindrical coordinates, which takes into account the curvature of the Earth from the transmitter to the receiver as depicted in Figure 5.1. The ionosphere is modeled as a cold magnetized collisional electron plasma. The input parameters into the magnetized plasma equations are electron density, N_e , static magnetic field, \vec{B}_0 , and collision frequency, ν ,

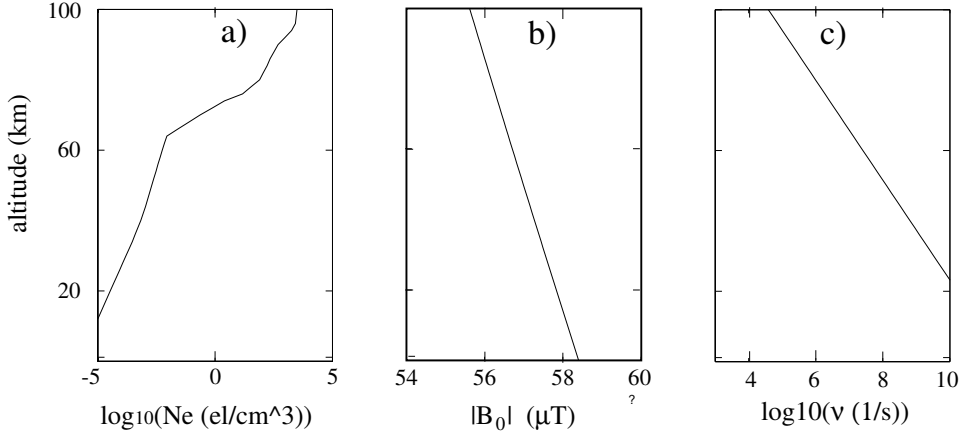


Figure 5.2: Ionospheric parameters used to model the earth-ionosphere waveguide. a) electron density vs. altitude. b) ambient magnetic field vs altitude. c) electron collision frequency vs. altitude.

all of which are functions of altitude, examples of which used in the modeling are plotted in Figure 5.2. In the simulations presented the direction of \vec{B}_0 is taken to be about 12 degrees with respect to the radial (ρ) axis in the $\rho - \theta$ plane; the 12 degree orientation is representative of an equatorward mid-latitude VLF propagation path. The specific profiles we use are those of an ambient nighttime mid-latitude ionosphere from *Johnson et al. (1999)* for which the reflection height of 20 kHz radio waves are typically in the range of 80-90 km. The magnetized plasma equations for the ionosphere are implemented in FDTD using equation (9) from *Lee and Kalluri (1999)* and for FDFD using equation (6) from *Lee and Kalluri (1999)*. However, our grid implementation is slightly different only in that the cited authors located their vector electric currents, \vec{J} at the grid nodes, while we co-locate each vector electric current component together with its corresponding vector electric field component, i.e., \vec{E}_x and \vec{J}_x are collocated, etc. We refer the reader to Appendix A for the form of the explicit equations used. For the ground we assume $\epsilon_r = 10.0, \sigma = 10^{-3} \text{ S/m}$, and for sea-water we assume, $\epsilon_r = 81.0, \sigma = 4.0 \text{ S/m}$, where ϵ_r is the relative permittivity and σ is the electrical conductivity. The transmitter is a short electric monopole pointed in the $\hat{\rho}$ -direction located 1-km above the ground and 20 km into the space.

We model the numerical space with approximately 500 m cells to properly sample the free space wavelength of a 19.4 kHz wave with about 30 cells. All PML's used are 10 cells thick. All FDTD simulations were run at .7 of the Courant condition.

Two tests were run for both the FDFD and FDTD techniques. In Test 1 we model the space from Figure 5.1 along the first 500 km of the path. For Run 1 of Test 1 we model the entire 500 km path in a single grid. For Run 2 of Test 1 we apply the SLP technique using the following sequence L of segment lengths (in km) where $L = (100, 100, 100, 100, 100, 100)$ and thus a total of 6 segments are used. Each successive segment overlaps the prior segment for 20 km, i.e, the total/scattered boundary occurs at 10 km into the space and the fields saved near the end of the segment occurs at 10 km before the end of the space.

Test 1 was run by first applying the FDFD technique at 19.4 kHz (which is the frequency of operation of a Stanford University VLF transmitter located at South Pole [Chevalier *et al.*, 2006b]), extracting the ρ -directed electric fields along the ground and then plotting the amplitude of E_ρ and E_θ versus distance. The results are plotted in Figure 5.3a and show excellent agreement between Runs 1 and 2 (i.e., between single grid and segmented path models). Figure 5.3b shows a zoom-in on the E_θ field plot to display the slight error due to the SLP technique. For the FDTD technique, the source used was a modulated Gaussian pulse centered at 19.4 kHz with a 10 kHz bandwidth. For Run 1 the FDTD simulation was continued for 5000 timesteps. For Run 2a the SLP simulation used the following sequence T of timesteps where $T = (3500, 3500, 3500, 3500, 3500, 3500)$ and T_i , the i th timestep entry, corresponds to the amount of timesteps that i th segment runs for. For FDTD, in addition to the RAM savings, we can calculate percentage savings of CPU hours for the SLP technique relative to the full grid technique and is given by the formula.

$$\text{percentage of CPU hour savings} = \left(1 - \frac{\sum_i T_i L_i}{T_f L_f}\right) \times 100 \quad (5.1)$$

where T_i is the number of timesteps run in the i th segment and L_i is the length of the i th segment. L_f is the full grid length (in km) and T_f is the number of timesteps the full grid ran. Applying (5.1) results in a CPU hour savings of about 14 percent.

For Run 2b the SLP simulation used the following sequence T of timesteps where $T = (1500, 1500, 1750, 2000, 2250, 2500)$. In this particular sequence T the number of timesteps for each successive segment is increased to account for the dispersion of the fields. Applying (5.1) results in a CPU hour savings of about 54 percent. Figure 5.3c and 5.3d shows plots of E_ρ and E_z over time, respectively, just above the ground at a distance of 480 km along the path. In Figure 5.3c the agreement is very good between Runs 1 and 2a,b. Figure 5.3d is more interesting, showing that the field levels are smaller and exhibiting a train of pulses for the different waveguide modes. For Run 2a the agreement is again excellent with Run 1 for the entire duration. For Run 2b, which ends at about 4100 timesteps, the results capture up to just past the 4th pulse-train. Error is evident in Run 2a beginning near timestep 3400. Figure 5.3e shows a zoom-in of the E_z field to better illustrate the error that is introduced by the SLP technique in Run 2b. The solution of Run 2b rings about the solutions of Run 1 and Run 2a. To explain this error we notice that for both Run 2a and Run 2b the input fields into each segment are truncated in time when they are saved from the prior segment. The FDTD spaces are then run past the truncation, in time, of the input source fields. This truncation is a discontinuity in the source fields which can then propagate through the space. The sequence of timesteps for Run 2a is such that these 'discontinuity' fields, say in Segment ' N ', never reach the surface ' S_N ' of Segment ' N ' and, therefore, are not saved as input fields into the next segment. However, for Run 2b, the sequence of timesteps are successively increasing in the number of timesteps and the 'discontinuity' fields do reach surface ' S_N ' of segment ' N ' to be saved as input fields, thereby propagating through succeeding segments. Even though Run 2b introduces nonphysical waves into the system, it still matches Run 1 and Run 2a until timestep 3400 and reasonably captures the pulse up to timestep 4000. One possible fix for this truncation error might be to decay the source fields, say starting 100 timesteps before the truncation, to reduce the effects of this discontinuity. This a topic of current and future research is not explored in this dissertation. An important conclusion regarding differences in simulation results between Run 2a and 2b is that one must be careful with the SLP technique when trying to attain significant CPU hour savings especially with an extremely dispersive

path medium such as a waveguide.

For Test 2, we model the entire space in Figure 5.1, which is about 2500 km in length. For the SLP technique, the sequence of segment lengths L (in km) where $L = (100, 500, 500, 500, 500, 500)$, 6 segments in all, with 20 km overlap as in Test 1. For FDFD, our resources only allow us to run up to 500 km segments. We therefore must apply the SLP technique. The results are plotted in Figure 5.4a for only the SLP technique. Based on the excellent agreement between the standard FDFD and the SLP technique from Test 1, we expect these results to be accurate. For FDTD, in Run 1 we run the entire grid for 14000 timesteps. For Run 2 we have the the following sequence of time steps for the sequence T of timesteps where $T = (8000, 8000, 8000, 8000, 8000, 8000)$ and T_i , the i th timestep entry, corresponds to the amount of timesteps that i th segment runs for. Applying (5.1) results in a CPU hour savings of about 40 percent. Figure 5.4b and 5.4c plot E_ρ and E_z over time, respectively, just above the ground at a distance of 2480 km along the path. Figure 5.4d shows a zoom-in of E_z . As expected the SLP technique, to the plot resolution, matches with the full grid solution.

For the SLP tests, close examination of all of our calculations in this chapter indicates that the backscattered fields are always negligible in magnitude (typically smaller by a factor of > 50 dB) compared to the forward propagating fields. This result is primarily due to the fact that other than the ground-to-sea transition (which is a 1 cell transition) no scattering objects, e.g., regions of ionospheric conductivity change, were placed along the path. The numerical results above were designed to validate the SLP technique along a homogeneous ionospheric path. However, as mentioned before based on purely theoretical arguments, by breaking our space up into segments we neglect interactions between scattering regions from different segments. To minimize effects of such error a scattering region should be entirely contained within a segment so that the scattering is entirely solved for within the segment.

In FDTD, the SLP technique as it relates to the moving-window technique of *Thevenot et al.* (1999), requires more computation. This requirement arises because the moving window technique moves with the pulse, while the SLP technique requires

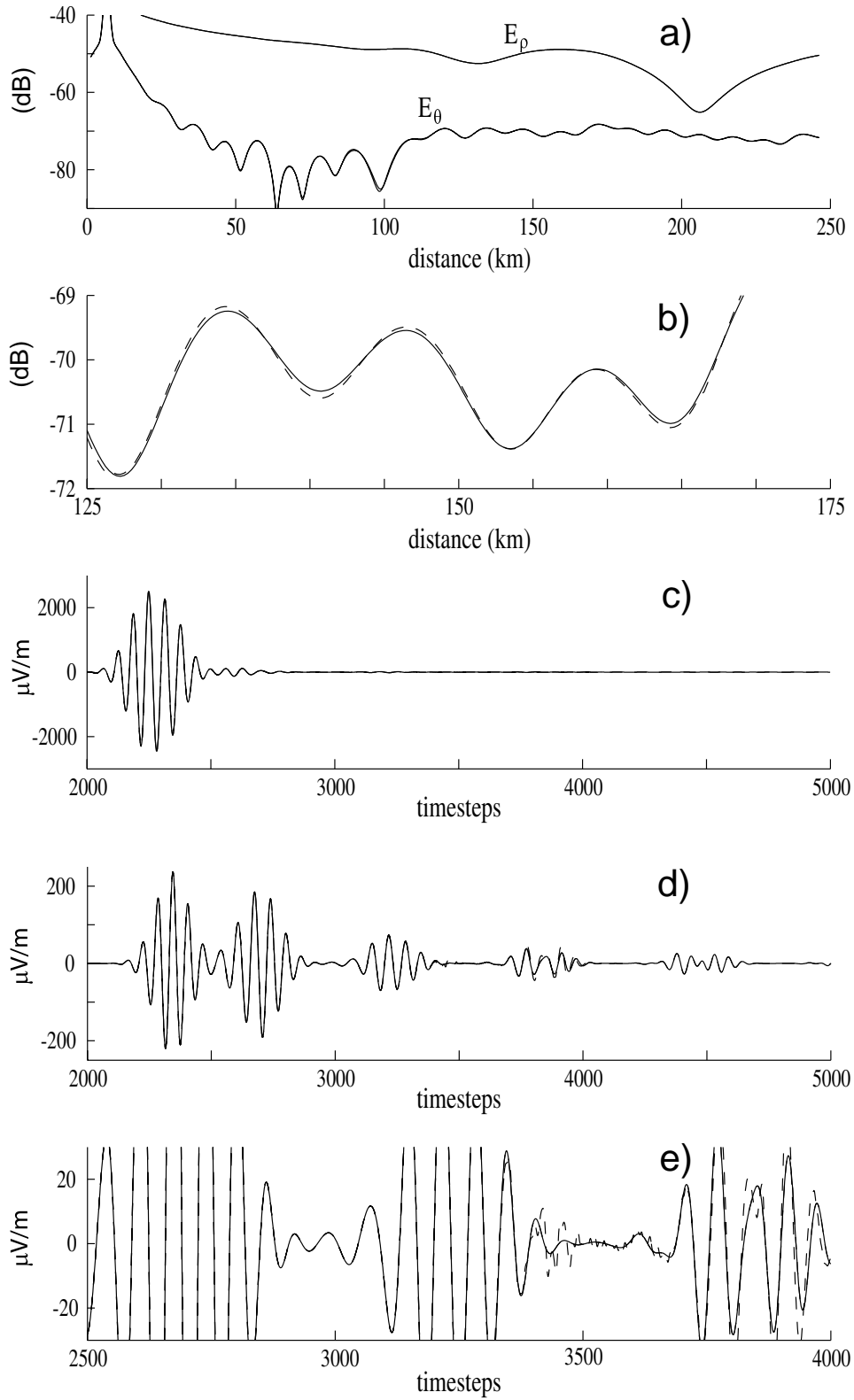


Figure 5.3: Test 1 results. All plots: full grid-solid line, SLP - dashed line. a) FDFD plots of E_ρ and E_θ just above ground vs. distance. b) FDFD plot: zoom in of E_θ . c)-e) to the resolution of the plot, results from run 1 match results from run 2a. c) FDTD plot of time domain pulse of E_ρ just above ground at 480 km distance. d) FDTD plot of time domain pulse of E_z just above ground at 480 km distance. e) FDTD plot: zoom in of E_z .

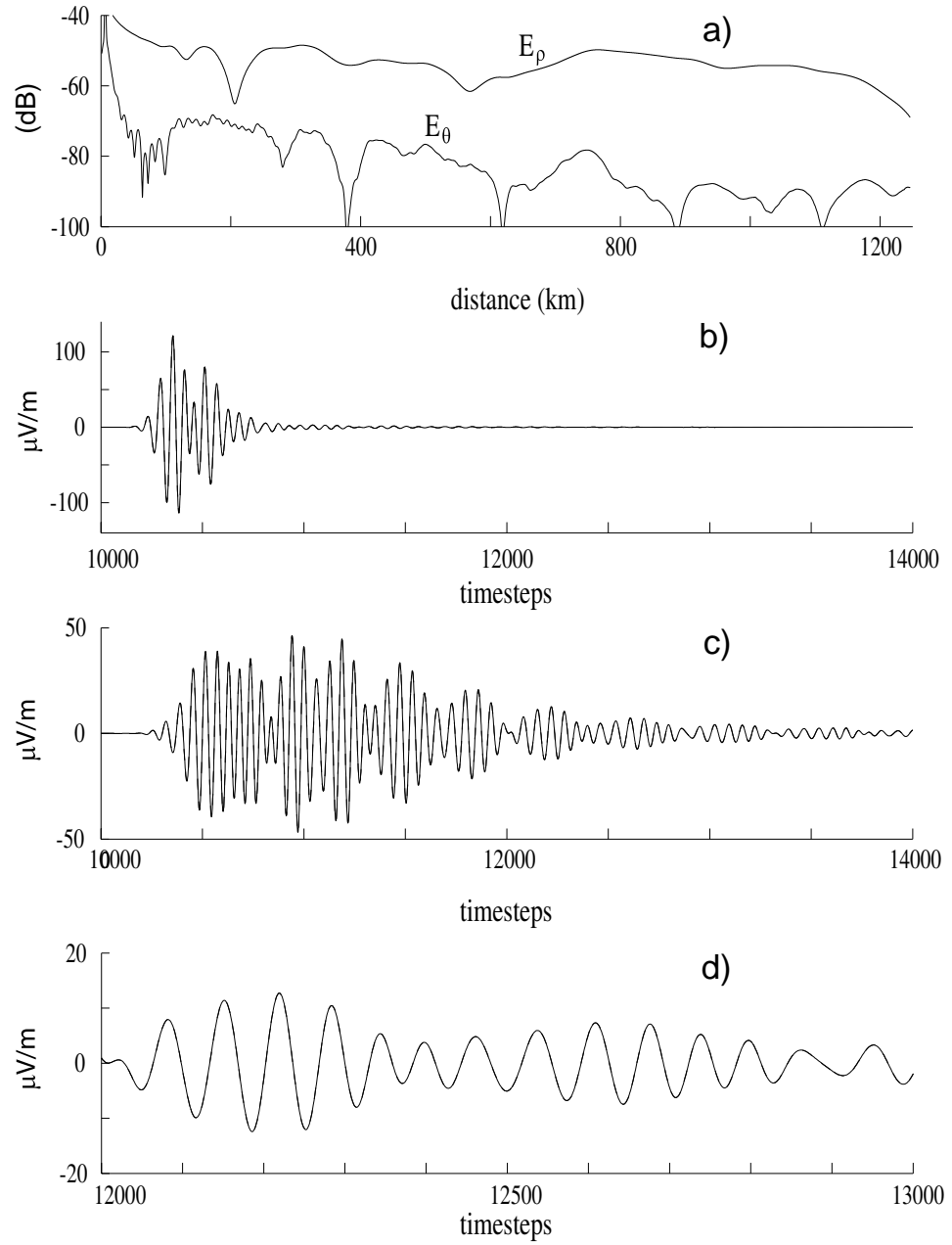


Figure 5.4: Test 2 results. All plots: full grid-solid line, SLP - dashed line. a) FDFD plots of E_ρ and E_θ just above ground vs. distance. The full grid solution was not computed due to unavailable resources. b) FDTD plot of time domain pulse of E_ρ just above ground at 2480 km distance. c) FDTD plot of time domain pulse of E_z just above ground at 2480 km distance. d) FDTD plot: zoom in of E_z .

the pulse to pass through each segment. However, the SLP technique is more versatile, as it is capable of capturing the entire dispersion of the pulse where a static sized moving-window, in general, cannot. Especially for propagation in waveguides, where the dispersion can be very large, the SLP is thus better suited. Also, for the SLP technique the segment sizes and the number of timesteps run for each segment can be varied throughout the space. For FDFD one cannot apply the moving window techniques at all since it is specifically designed for the time-domain. The SLP technique is thus the only option for FDFD and performs quite well.

Chapter 6

Summary and Suggested Future Work

In this dissertation, we addressed two important issues concerning the application of finite-difference methods (FDTD and FDFD) for the solution of electromagnetic problems, namely Perfectly Matched Layer boundary conditions for general media and modeling of propagation on long paths.

6.1 Summary of PML work

In Chapter 2 we described a new time domain representation, the Nth order CCO-PML, which proves to be simple to implement for any linear medium. Time domain and frequency domain experiments were performed to validate the new method. The N convolutions allow one to design a more robust PML over a desired frequency range through the use of the numerical reflection coefficient calculation derived in Chapter 4.

In Chapter 3 we described a new PML formulation, referred to as the KPML, which explicitly takes into account information on the k-vector direction of incident waves. The use of the KPML method is necessitated for media in which the k-vector and group velocity vector components normal to the PML are antiparallel, in which case the traditional PML algorithms result in the growth of the waves (rather

than their attenuation) within the PML region. We applied the KPML method to the specific case of whistler-mode waves in a magnetized plasma and quantified its effectiveness with both reflection coefficient calculations as well as demonstrating the stability of the formulation with both implicit and explicit time domain simulations. As was shown for the whistler-mode, even at a single frequency, the group velocity and k-vector can have parallel or anti-parallel components with respect to the vector normal to the PML, depending on the incident wave angle. In such cases the KPML also becomes necessary for FDFD simulations.

In Chapter 4 we derive the numerical reflection coefficient for any plane wave incident onto the PML, propagating or evanescent. This derivation was done for both the Nth order CCO-PML and the KPML. The importance of this calculation is that it quantifies the error from the PML within a finite-difference grid, thus providing a quantifiable bound to how much we can trust the results of the simulations. We can then apply various optimization techniques to reduce the error over our desired range of frequencies and incident angles.

6.1.1 Suggested Future Work for PML

The KPML represents a solution to a shortcoming of the original PML, namely providing a k-vector dependent operation to still attenuate the waves when the group velocity vector and k-vector differ in direction. The KPML and the CCO-PML seem to complete the possible operations that the PML can perform on the waves propagating within it, namely frequency and k-vector dependent operations. A next step would be to develop a general recipe to derive a PML for any medium, using the index of refraction surface(s) for that medium. This derivation would involve the application of the KPML and/or the CCO-PML.

We show that, in general, the numerical reflection coefficient Γ is not a convex function, therefore making it more difficult to optimize. The better the KPML and CCO-PML are optimized for a given simulation, the more confidently we can trust our solution. To better optimize Γ requires a better understanding of the mathematical properties of it in relation to the PML coefficients. It would therefore be beneficial to

better understand Γ to find the best way to optimize it. Currently, genetic algorithms represent a popular method for optimizing non-convex functions, and thus represent a possible method for optimizing Γ .

6.2 Summary of SLP work

In Chapter 5 we developed a new technique, called the Segmented Long Path (SLP) technique, for efficiently modeling long propagation paths for use in both FDFD and FDTD. The technique makes use of the total-field/scattered-field boundary technique as well as the PML. For FDTD, the SLP technique is well suited for capturing both fast and slow modes while providing both RAM and CPU hour savings. For FDFD, the SLP technique is currently the only method for efficiently solving propagation on long paths.

6.2.1 Future Work for SLP technique

Applying the SLP technique to model multiple scattering regions along the path was discussed theoretically but was not numerically tested and is a topic of current research. Further suggested applications of the SLP technique could be applying the method to long path propagation within periodic structures or the modeling of whistler-mode coupling, propagation, and exiting through magnetospheric ducts.

Appendix A

Finite Difference Equations

Presented below are the field equations for the both the Finite-Difference Time-Domain [Taflove (1995); Taflove and Hagness (2000)] and the Finite-Difference Frequency-Domain techniques [Zhao *et al.* (2002)] that are used in this thesis. For FDTD, the notation for the fields, taking E_y for example is, $E_{yt}|_{i,j+.5,k}^n$, where n is the timestep, and i, j, k is the grid node location. For FDFD, the notation for the fields, taking E_y for example is, $E_{yt}|_{i,j+.5,k}^\omega$, where ω is the radial frequency, and i, j, k is the grid node location. The equations assume a constant permittivity ε and permeability μ_0 .

A.1 Finite-Difference Time Domain equations

$$\varepsilon \frac{E_{xt}|_{i+.5,j,k}^{n+1} - E_{xt}|_{i+.5,j,k}^n}{\Delta t} + J_{xt}|_{i+.5,j,k}^{n+.5} = - \frac{H_{yt}|_{i+.5,j,k+.5}^{n+.5} - H_{yt}|_{i+.5,j,k-.5}^{n+.5}}{\Delta z} + \frac{H_{zt}|_{i+.5,j+.5,k}^{n+.5} - H_{zt}|_{i+.5,j-.5,k}^{n+.5}}{\Delta y} \quad (\text{A.1})$$

$$\varepsilon \frac{E_{yt}|_{i,j+.5,k}^{n+1} - E_{yt}|_{i,j+.5,k}^n}{\Delta t} + J_{yt}|_{i,j+.5,k}^{n+.5} = \frac{H_{xt}|_{i,j+.5,k+.5}^{n+.5} - H_{xt}|_{i,j+.5,k-.5}^{n+.5}}{\Delta z}$$

$$-\frac{H_{zt}|_{i+.5,j+.5,k}^{n+.5} - H_{zt}|_{i-.5,j+.5,k}^{n+.5}}{\Delta x} \quad (\text{A.2})$$

$$\begin{aligned} \varepsilon \frac{E_{zt}|_{i,j,k+.5}^{n+1} - E_{zt}|_{i,j,k+.5}^n}{\Delta t} + J_{zt}|_{i,j,k+.5}^{n+.5} &= -\frac{H_{xt}|_{i,j+.5,k+.5}^{n+.5} - H_{xt}|_{i,j-.5,k+.5}^{n+.5}}{\Delta y} \\ &+ \frac{H_{yt}|_{i+.5,j,k+.5}^{n+.5} - H_{yt}|_{i-.5,j,k+.5}^{n+.5}}{\Delta x} \end{aligned} \quad (\text{A.3})$$

$$\begin{aligned} \mu_0 \frac{H_{xt}|_{i,j+.5,k+.5}^{n+.5} - H_{xt}|_{i,j+.5,k+.5}^{n-.5}}{\Delta t} &= \frac{E_{yt}|_{i,j+.5,k+1}^n - E_{yt}|_{i,j+.5,k}^n}{\Delta z} \\ &- \frac{E_{zt}|_{i,j+1,k+.5}^n - E_{zt}|_{i,j,k+.5}^n}{\Delta y} \end{aligned} \quad (\text{A.4})$$

$$\begin{aligned} \mu_0 \frac{H_{yt}|_{i+.5,j,k+.5}^{n+.5} - H_{yt}|_{i+.5,j,k+.5}^{n-.5}}{\Delta t} &= -\frac{E_{xt}|_{i+.5,j,k+1}^n - E_{xt}|_{i+.5,j,k}^n}{\Delta z} \\ &+ \frac{E_{zt}|_{i+1,j,k+.5}^n - E_{zt}|_{i,j,k+.5}^n}{\Delta x} \end{aligned} \quad (\text{A.5})$$

$$\begin{aligned} \mu_0 \frac{H_{zt}|_{i+.5,j+.5,k}^{n+.5} - H_{zt}|_{i+.5,j+.5,k}^{n-.5}}{\Delta t} &= \frac{E_{xt}|_{i+.5,j+1,k}^n - E_{xt}|_{i+.5,j,k}^n}{\Delta y} \\ &- \frac{E_{yt}|_{i+1,j+.5,k}^n - E_{yt}|_{i,j+.5,k}^n}{\Delta x} \end{aligned} \quad (\text{A.6})$$

$$\begin{aligned}
J_{xt} \big|_{(i+.5,j,k)}^{n+.5} &= a_{12} J_{xt} \big|_{(i+.5,j,k)}^{n-.5} \\
&+ a_{12} \frac{(J_{yt} \big|_{i,j+.5,k}^{n-.5} + J_{yt} \big|_{i+1,j+.5,k}^{n-.5} + J_{yt} \big|_{i,j-.5,k}^{n-.5} + J_{yt} \big|_{i+1,j-.5,k}^{n-.5})}{4} \\
&+ a_{13} \frac{(J_{zt} \big|_{i,j,k+.5}^{n-.5} + J_{zt} \big|_{i+1,j,k+.5}^{n-.5} + J_{zt} \big|_{i,j,k-.5}^{n-.5} + J_{zt} \big|_{i+1,j,k-.5}^{n-.5})}{4} \\
&+ k_{11} E_{xt} \big|_{i+.5,j,k}^n \\
&+ k_{12} \frac{(E_{yt} \big|_{i,j+.5,k}^n + E_{yt} \big|_{i+1,j+.5,k}^n + E_{yt} \big|_{i,j-.5,k}^n + E_{yt} \big|_{i+1,j-.5,k}^n)}{4} \\
&+ k_{13} \frac{(E_{zt} \big|_{i,j,k+.5}^n + E_{zt} \big|_{i+1,j,k+.5}^n + E_{zt} \big|_{i,j,k-.5}^n + E_{zt} \big|_{i+1,j,k-.5}^n)}{4}
\end{aligned} \tag{A.7}$$

$$\begin{aligned}
J_{yt} \big|_{i,j+.5,k}^{n+.5} &= a_{21} \frac{(J_{xt} \big|_{i+.5,j,k}^{n-.5} + J_{xt} \big|_{i-.5,j,k}^{n-.5} + J_{xt} \big|_{i+.5,j+1,k}^{n-.5} + J_{xt} \big|_{i-.5,j+1,k}^{n-.5})}{4} \\
&+ a_{22} J_{yt} \big|_{i,j+.5,k}^n \\
&+ a_{23} \frac{J_{zt} \big|_{i,j,k-.5}^{n-.5} + J_{zt} \big|_{i,j,k+.5}^{n-.5} + J_{zt} \big|_{i,j+1,k-.5}^{n-.5} + J_{zt} \big|_{i,j+1,k+.5}^{n-.5}}{4} \\
&+ k_{21} \frac{(E_{xt} \big|_{i+.5,j,k}^n + E_{xt} \big|_{i-.5,j,k}^n + E_{xt} \big|_{i+.5,j+1,k}^n + E_{xt} \big|_{i-.5,j+1,k}^n)}{4} \\
&+ k_{22} E_{yt} \big|_{i,j+.5,k}^n \\
&+ k_{23} \frac{E_{zt} \big|_{i,j,k-.5}^n + E_{zt} \big|_{i,j,k+.5}^n + E_{zt} \big|_{i,j+1,k-.5}^n + E_{zt} \big|_{i,j+1,k+.5}^n}{4}
\end{aligned} \tag{A.8}$$

$$\begin{aligned}
J_{zt} \big|_{i,j,k+.5}^{n+.5} &= a_{31} \frac{(J_{xt} \big|_{i+.5,j,k}^{n-.5} J_{xt} \big|_{i-.5,j,k}^{n-.5} + J_{xt} \big|_{i+.5,j,k+1}^{n-.5} J_{xt} \big|_{i-.5,j,k+1}^{n-.5})}{4} \\
&+ a_{32} \frac{J_{yt} \big|_{i,j-.5,k}^{n-.5} + J_{yt} \big|_{i,j+.5,k}^{n-.5} + J_{yt} \big|_{i,j-.5,k+1}^{n-.5} + J_{yt} \big|_{i,j+.5,k+1}^{n-.5}}{4} \\
&+ a_{33} J_{zt} \big|_{i,j,k+.5}^{n-.5}
\end{aligned}$$

$$\begin{aligned}
& +k_{31} \frac{(E_{xt}|_{i+.5,j,k}^n E_{xt}|_{i-.5,j,k}^n + E_{xt}|_{i+.5,j,k+1}^n E_{xt}|_{i-.5,j,k+1}^n)}{4} \\
& +k_{32} \frac{E_{yt}|_{i,j-.5,k}^n + E_{yt}|_{i,j+.5,k}^n + E_{yt}|_{i,j-.5,k+1}^n + E_{yt}|_{i,j+.5,k+1}^n}{4} \\
& +k_{33} E_{zt}|_{i,j,k+.5}^n
\end{aligned} \tag{A.9}$$

A.2 Finite-Difference Frequency Domain equations

$$\begin{aligned}
j\omega\varepsilon E_{xt}|_{i+.5,j,k}^\omega + J_{xt}|_{i+.5,j,k}^\omega &= -\frac{H_{yt}|_{i+.5,j,k+.5}^\omega - H_{yt}|_{i+.5,j,k-.5}^\omega \Delta z}{\Delta y} \\
&+ \frac{H_{zt}|_{i+.5,j+.5,k}^\omega - H_{zt}|_{i+.5,j-.5,k}^\omega}{\Delta y}
\end{aligned} \tag{A.10}$$

$$\begin{aligned}
j\omega\varepsilon E_{yt}|_{i,j+.5,k}^\omega + J_{yt}|_{i,j+.5,k}^\omega &= \frac{H_{xt}|_{i,j+.5,k+.5}^\omega - H_{xt}|_{i,j+.5,k-.5}^\omega}{\Delta z} \\
&- \frac{H_{zt}|_{i+.5,j+.5,k}^\omega - H_{zt}|_{i-.5,j+.5,k}^\omega}{\Delta x}
\end{aligned} \tag{A.11}$$

$$\begin{aligned}
j\omega\varepsilon E_{zt}|_{i,j,k+.5}^\omega + J_{zt}|_{i,j,k+.5}^\omega &= -\frac{H_{xt}|_{i,j+.5,k+.5}^\omega - H_{xt}|_{i,j-.5,k+.5}^\omega}{\Delta y} \\
&+ \frac{H_{yt}|_{i+.5,j,k+.5}^\omega - H_{yt}|_{i-.5,j,k+.5}^\omega}{\Delta x}
\end{aligned} \tag{A.12}$$

$$j\omega\mu_0 H_{xt}|_{i,j+.5,k+.5}^\omega = \frac{E_{yt}|_{i,j+.5,k+1}^\omega - E_{yt}|_{i,j+.5,k}^\omega}{\Delta z}$$

$$-\frac{E_{zt}|_{i,j+1,k+.5}^{\omega} - E_{zt}|_{i,j,k+.5}^{\omega}}{\Delta y} \quad (\text{A.13})$$

$$\begin{aligned} j\omega\mu_0 H_{yt}|_{i+.5,j,k+.5}^{\omega} = & -\frac{E_{xt}|_{i+.5,j,k+1}^{\omega} - E_{xt}|_{i+.5,j,k}^{\omega}}{\Delta z} \\ & + \frac{E_{zt}|_{i+1,j,k+.5}^{\omega} - E_{zt}|_{i,j,k+.5}^{\omega}}{\Delta x} \end{aligned} \quad (\text{A.14})$$

$$\begin{aligned} j\omega\mu_0 H_{zt}|_{i+.5,j+.5,k}^{\omega} = & \frac{E_{xt}|_{i+.5,j+1,k}^{\omega} - E_{xt}|_{i+.5,j,k}^{\omega}}{\Delta y} \\ & - \frac{E_{yt}|_{i+1,j+.5,k}^{\omega} - E_{yt}|_{i,j+.5,k}^{\omega}}{\Delta x} \end{aligned} \quad (\text{A.15})$$

$$\begin{aligned} J_{xt}|_{(i+.5,j,k)}^{\omega} = & \sigma_{11} E_{xt}|_{i+.5,j,k}^{\omega} \\ & + \sigma_{12} \frac{(E_{yt}|_{i,j+.5,k}^{\omega} + E_{yt}|_{i+1,j+.5,k}^{\omega} + E_{yt}|_{i,j-.5,k}^{\omega} + E_{yt}|_{i+1,j-.5,k}^{\omega})}{4} \\ & + \sigma_{13} \frac{(E_{zt}|_{i,j,k+.5}^{\omega} + E_{zt}|_{i+1,j,k+.5}^{\omega} + E_{zt}|_{i,j,k-.5}^{\omega} + E_{zt}|_{i+1,j,k-.5}^{\omega})}{4} \end{aligned} \quad (\text{A.16})$$

$$\begin{aligned} J_{yt}|_{i,j+.5,k}^{\omega} = & \sigma_{21} \frac{(E_{xt}|_{i+.5,j,k}^{\omega} + E_{xt}|_{i-.5,j,k}^{\omega} + E_{xt}|_{i+.5,j+1,k}^{\omega} + E_{xt}|_{i-.5,j+1,k}^{\omega})}{4} \\ & + \sigma_{22} E_{yt}|_{i,j+.5,k}^{\omega} \\ & + \sigma_{23} \frac{E_{zt}|_{i,j,k-.5}^{\omega} + E_{zt}|_{i,j,k+.5}^{\omega} + E_{zt}|_{i,j+1,k-.5}^{\omega} + E_{zt}|_{i,j+1,k+.5}^{\omega}}{4} \end{aligned} \quad (\text{A.17})$$

$$\begin{aligned}
J_{zt} \big|_{i,j,k+.5}^\omega &= \sigma_{31} \frac{(E_{xt} \big|_{i+.5,j,k}^\omega E_{xt} \big|_{i-.5,j,k}^\omega + E_{xt} \big|_{i+.5,j,k+1}^\omega E_{xt} \big|_{i-.5,j,k+1}^\omega)}{4} \\
&\quad + \sigma_{32} \frac{E_{yt} \big|_{i,j-.5,k}^\omega + E_{yt} \big|_{i,j+.5,k}^\omega + E_{yt} \big|_{i,j-.5,k+1}^\omega + E_{yt} \big|_{i,j+.5,k+1}^\omega}{4} \\
&\quad + \sigma_{33} E_{zt} \big|_{i,j,k+.5}^\omega
\end{aligned} \tag{A.18}$$

Appendix B

Proof of generality of CCO-PML equations

In this section we mathematically prove both in the continuous case and the discrete case that the Nth order CCO-PML is of a more general form than the CPML of Roden and Gedney. We start with the CPML of *Roden and Gedney* (2000) both in the frequency domain and time domain:

$$\bar{s}_i(j\omega) = \frac{1}{k_i} - \frac{\sigma_i/(k_i^2 \varepsilon_0)}{j\omega + \sigma_i/(k_i \varepsilon_0) + \alpha_i/\varepsilon_0} \quad (\text{B.1})$$

$$\bar{s}_i(t) = \frac{\delta(t)}{k_i} - \frac{\sigma_i}{k_i^2 \varepsilon_0} e^{-(\sigma_i/(k_i \varepsilon_0) + \alpha_i/\varepsilon_0)t} u(t) \quad (\text{B.2})$$

One can rewrite (2) as

$$\bar{s}_i(t) = a_i \delta(t) - b_i e^{-c_i t} u(t) \quad (\text{B.3})$$

with the constraints that $a_i = 1/k_i$, $b_i = \sigma_i/(k_i^2 \varepsilon_0)$ and $c_i = \sigma_i/(k_i \varepsilon_0) + \alpha_i/\varepsilon_0$. For an N=2 case of the CCO-PML we have the following

$$\bar{s}_i(j\omega) = \frac{1}{1 + g_x(j\omega)} = 1 - \frac{b_{x1}\alpha_{x1}}{j\omega + \alpha_{x1}} - \frac{b_{x2}\alpha_{x2}}{j\omega + \alpha_{x2}} \quad (\text{B.4})$$

$$\bar{s}_i(t) = \delta(t) - b_{x1}\alpha_{x1}e^{-\alpha_{x1}t}u(t) - b_{x2}\alpha_{x2}e^{-\alpha_{x2}t}u(t) \quad (\text{B.5})$$

In the limit as $\alpha_{x1} \rightarrow \infty$ we get

$$\lim_{\alpha_{x1} \rightarrow \infty} \alpha_{x1}e^{-\alpha_{x1}t}u(t) = \delta(t) \quad (\text{B.6})$$

We will prove this statement later. We then find

$$\bar{s}_i(t) = (1 - b_{x1})\delta(t) - b_{x2}\alpha_{x2}e^{-\alpha_{x2}t}u(t) \quad (\text{B.7})$$

where to get in the form of (3) we let $1 - b_{x1} = a_i$, $b_{x2}\alpha_{x2} = b_i$ and $\alpha_{x2} = c_i$. They are now in identical form. We have, therefore, shown that the CPML equations are a subset of the Nth order CCO-PML equations.

B.1 Proof of the delta function

It is easily shown that

$$\lim_{\alpha_{x1} \rightarrow \infty} \alpha_{x1}e^{-\alpha_{x1}t}u(t) = \delta(t) \quad (\text{B.8})$$

A delta function is defined by the following:

$$\delta(t) = \begin{cases} \infty & t = 0 \\ 0 & \text{otherwise} \end{cases} \quad (\text{B.9})$$

$$\int_{-\infty}^{\infty} \delta(t) dt = 1 \quad (\text{B.10})$$

In general we have

$$u(t)\alpha_{x1}e^{-\alpha_{x1}t} = \begin{cases} 0 & t < 0 \\ \alpha_{x1} & t = 0 \\ e^{-\alpha_{x1}t} & t > 0 \end{cases} \quad (\text{B.11})$$

and

$$\int_{-\infty}^{\infty} u(t)\alpha_{x1}e^{-\alpha_{x1}t} dt = 1 \quad (\text{B.12})$$

In the limiting case we get

$$\lim_{\alpha_{x1} \rightarrow \infty} u(t)\alpha_{x1}e^{-\alpha_{x1}t} = \begin{cases} 0 & t < 0 \\ \infty & t = 0 \\ 0 & t > 0 \end{cases} \quad (\text{B.13})$$

Therefore

$$\lim_{\alpha_{x1} \rightarrow \infty} u(t)\alpha_{x1}e^{-\alpha_{x1}t} = \delta(t)$$

$$(B.14)$$

Frequency domain analysis shows that the term

$$\lim_{\alpha_{x1} \rightarrow \infty} \frac{\alpha_{x1}}{j\omega + \alpha_{x1}} = 1 \quad \text{for } \alpha_{xi} \gg j\omega \quad (B.15)$$

We can always make α_{x1} much larger than our frequency range of interest. And when you take the inverse fourier transform of unity, you get $\delta(t)$. As a third and final proof, and perhaps the most relevant, let us look at the discretized version of $\Psi(t) = u(t)\alpha_{x1}e^{-\alpha_{x1}t} * F(t)$, where $F(t)$ is any time domain function. We'll start with the the Piecewise Constant Recursive Convolution (PCRC) formulation

$$\Psi|{}^n = \Psi|{}^{n-1}e^{-\alpha_{x1}\Delta t} + F|{}^n[1 - e^{-\alpha_{x1}\Delta t}] \quad (B.16)$$

which as $\lim_{\alpha_{x1} \rightarrow \infty}$ we get $\Psi|{}^n = F|{}^n$. This is the discretized version of $\Psi(t) = \delta(t) * F(t) = F(t)$. Similarly for the piecewise linear recursive convolution (PLRC) formulation

$$\begin{aligned} \Psi|{}^n = & \Psi|{}^{n-1}e^{-\alpha_{x1}\Delta t} + F|{}^n \left[1 - e^{-\alpha_{x1}\Delta t} - \frac{1 - e^{-\alpha_{x1}\Delta t} - \alpha_{x1}\Delta te^{-\alpha_{x1}\Delta t}}{\alpha_{x1}\Delta t} \right] \\ & + F|{}^{n-1} \left[\frac{1 - e^{-\alpha_{x1}\Delta t} - \alpha_{x1}\Delta te^{-\alpha_{x1}\Delta t}}{\alpha_{x1}\Delta t} \right] \end{aligned} \quad (B.17)$$

we have as $\lim_{\alpha_{x1} \rightarrow \infty}$ that $\Psi|{}^n = F|{}^n$ which is also equivalent to $\Psi(t) = \delta(t) * F(t) = F(t)$.

We have therefore shown, both in the continuous and discretized case that

$$\lim_{\alpha_{x1} \rightarrow \infty} u(t) \alpha_{x1} e^{-\alpha_{x1} t} = \delta(t) \tag{B.18}$$

Appendix C

Some Mathematical Properties of Γ

To better understand, mathematically, the reflection coefficient function we will first analyze the system

$$A_m x_m = b_m \quad (\text{C.1})$$

where A_m is the matrix containing all the equations of the incident wave/PML interaction we derived in Chapter 4 and b_m are the boundary conditions derived. A_m is a function of incident angle and the PML coefficients $b_{x0}(i), \dots, b_{xn}(i), e^{\alpha_{x1}(i)\Delta t}, \dots, e^{\alpha_{xn}(i)\Delta t}$ for the CCO-PML, or $b_{x0}(i), \sigma_x(i)$ for the KPML. More importantly, entries in the matrix, A_m containing the PML coefficients are linear combinations of the PML coefficients, this will later be shown to be important.

For simplicity, from the solution x_m , we'll only concern ourselves with $H_{yt} \big|_{.5, j_0, k_0 + .5}^{n+.5, \omega}$ and $H_{zt} \big|_{.5, j_0 + .5, k_0}^{n+.5, \omega}$, the magnetic fields just outside the PML. For simplicity in notation we'll have $H_{yt0} = H_{yt} \big|_{.5, j_0, k_0 + .5}^{n+.5, \omega}$ and $H_{zt0} = H_{zt} \big|_{.5, j_0 + .5, k_0}^{n+.5, \omega}$. The reflection coefficient for the \hat{y} -directed and \hat{z} -directed magnetic fields is

$$\Gamma = \frac{|H_{yt0} - H_{yi0}|^2 + |H_{zt0} - H_{zi0}|^2}{|H_{yi0}|^2 + |H_{zi0}|^2} \quad (\text{C.2})$$

where $[H_{yi0}, H_{yi0}]$ are the incident fields. We'll now convert our matrix system into an equivalent real system

$$W_m = \begin{pmatrix} \text{Re}(A_m) & -\text{Im}(A_m) \\ \text{Im}(A_m) & \text{Re}(A_m) \end{pmatrix}, c_m = \begin{pmatrix} \text{Re}(b_m) \\ \text{Im}(b_m) \end{pmatrix}, y_m = \begin{pmatrix} \text{Re}(x_m) \\ \text{Im}(x_m) \end{pmatrix}$$

Where from y_m we get $\text{Re}(H_{zt} |_{.5, j_0 + .5, k_0}^{n+.5, \omega}) = H_{zt0, r}$ and $\text{Im}(H_{zt} |_{.5, j_0 + .5, k_0}^{n+.5, \omega}) = H_{zt0, i}$ and similar for H_{yt} . Cramer's rule allows us to describe these fields in terms of determinates of matrices where for $H_{yt0, r}$

$$H_{yt0, r} = \frac{|W_{H_{yt0, r}, c_m}|}{|W_m|} \quad (\text{C.3})$$

where the matrix $W_{H_{yt0, r}, c_m}$ is the matrix W_m replacing the entries in the column for $\text{Re}(H_{yt} |_{.5, j_0, k_0 + .5}^{n+.5, \omega})$ with the column c_m . Likewise

$$H_{zt0, r} = \frac{|W_{H_{zt0, r}, c_m}|}{|W_m|} \quad (\text{C.4})$$

Our reflection coefficient then looks like

$$\begin{aligned} \Gamma &= \frac{(H_{yt0, r} - H_{yi0, r})^2 + (H_{yt0, i} - H_{yi0, i})^2}{(H_{yi0, r})^2 + (H_{yi0, i})^2 + (H_{zi0, r})^2 + (H_{zi0, i})^2} \\ &\quad + \frac{(H_{zt0, r} - H_{zi0, r})^2 + (H_{zt0, i} - H_{zi0, i})^2}{(H_{yi0, r})^2 + (H_{yi0, i})^2 + (H_{zi0, r})^2 + (H_{zi0, i})^2} \\ &= \frac{(\frac{\det W_{H_{yt0, r}, c_m}}{\det W_m} - H_{yi0, r})^2 + (\frac{\det W_{H_{yt0, i}, c_m}}{\det W_m} - H_{yi0, i})^2}{(H_{yi0, r})^2 + (H_{yi0, i})^2 + (H_{zi0, r})^2 + (H_{zi0, i})^2} \\ &\quad + \frac{(\frac{\det W_{H_{zt0, r}, c_m}}{\det W_m} - H_{zi0, r})^2 + (\frac{\det W_{H_{zt0, i}, c_m}}{\det W_m} - H_{zi0, i})^2}{(H_{yi0, r})^2 + (H_{yi0, i})^2 + (H_{zi0, r})^2 + (H_{zi0, i})^2} \end{aligned} \quad (\text{C.5})$$

In relation to the optimization of the PML the most important question is how does Γ

behave as a function of the parameters $b_{x0}(i), \dots, b_{xn}(i), \alpha_{x1}(i), \dots, \alpha_{xn}(i)$ (CCO-PML). A property of a real matrix, R , with linear varying parameters is that $-\log(\det(R^2))$ is convex function of its linear varying parameters [(*Boyd and Vandenberghe*, 2004)], which means that it can be globally optimized. From Γ we have the term

$$\left(\frac{\det W_{H_{yt0,r},c_m}}{\det W_m} \right)^2 \quad (\text{C.6})$$

It should be noted that both, $W_{H_{yt0,r},c_m}$, W_m are linearly varying w.r.t the PML coefficients and that goes for all matrices in Γ . Using the fact that $\det R \det R = \det R^2$ and performing the log operation on the term (C.6) yields

$$\log(\det(W_{H_{yt0,r},c_m}^2)) - \log(\det(W_m^2)) \quad (\text{C.7})$$

Because (C.7) is the difference between two convex functions, it is in general not a convex function. Only a sum of two convex functions absolutely yields a convex function. Therefore, since at least some of the terms of Γ are non-convex functions, Γ is, in general, a non-convex function and therefore exhibits at least two local extremum. This makes the optimization of Γ much more difficult than if it were a convex function. For this thesis, we therefore psuedo-optimize within a subspace of the PML coefficients where a local minima is reached.

Bibliography

- Akleman F., and L. Sevgi, A novel finite-difference time-domain wave propagator, *IEEE Transactions on Antennas and Propagat.*, vol. AP-48, no. 5, pp. 839-841, May 2000.
- Berenger J. P., A Perfectly Matched Layer for the Absorption of Electromagnetic Waves, *J. Computational Physics*, vol. 114, pp.185-200, 1994 .
- Berenger J. P., Evanescent waves in PML's: Origin of the numerical reflection in wave-structure interaction problems, *IEEE APS*, vol. 47, pp.1497-1503, Oct 1999.
- Berenger J. P., Numerical Reflections from FDTD-PML's: A comparison of the split PML with the unsplit and CFSPMLs, *IEEE APS*, vol. 50, pp.258-265, March 2002.
- Berenger J. P., Application of the CFSPML to the absorption of evanescent waves in waveguides, *IEEE Microwave and Wireless Components Letters*, vol. 12, pp.218-220, June 2002.
- Becache E., S. Fauqueux, P. Joly, Stability of perfectly matched layers, group velocities, and anisotropic waves, *J. Computational Physics*, vol. 188, 2003, pp.399-433,
- Boyd, S., and L. Vandenberghe , *Convex Optimization*, Cambridge University Press, 2004.
- Budden, K. G., *The Wave-Guide Mode Theory of Wave Propagation*, London, Logos Press, 1961.

- Chevalier M. W., A Perfectly-Matched-Layer Boundary Condition for use in FDTD Modeling of Pulse Propagation in the Earth-Ionosphere Waveguide, URSI/Radio Science Conference Proceedings, Boulder CO, (1999).
- Chevalier, M. W., and U. S. Inan, A PML using a convolutional curl operator and a numerical reflection coefficient for general linear media, *IEEE Trans. Ant. Prop.*, vol. 2, no.7, pp. 1647-57 July 2004.
- Chevalier, M. W., T. W. Chevalier, U. S. Inan, A PML Utilizing k-Vector Information as Applied to the Whistler Mode in a Magnetized Plasma, *IEEE Trans. Ant. Prop.*, vol. 2, no.7, pp. 1647-57 July 2004.
- Chevalier, M. W., and U. S. Inan, A Technique for Efficiently Modeling Long Path Propagation for use in both FDFD and FDTD, *IEEE Ant. Wire. Prop. Lett.*, in press.
- Chevalier T. W., U. S. Inan, and T. F. Bell, Numerical Simulation of Electric Dipole Antennas in the Inner Magnetosphere, presented at URSI/Radio Science Conf., Boulder, CO, 2006.
- Chevalier, T. W., U. S. Inan, and T. F. Bell, Characterization of terminal impedance and radiation properties of a horizontal VLF antenna over Antarctic ice, *Radio Sci.*, Vol. 41, No. 6, Nov. 2006.
- Chew W. C., and W. H. Weedon , A 3-D Perfectly Matched Medium fom Modified Maxwell's Equations with Stretched Coordinates, *Micro. Opt. Tech. Lett.*, vol. 7, no.13, pp.599-604, Sept. 1994.
- Chew, W. C., and J. M. Jin , Perfectly Matched Layer in the discretized medium. An analysis and optimization, *Electromag.*, vol. 16, no.4, pp 325-340, July. 1996.
- Cummer S. A., A Simple, Nearly Perfectly Matched Layer for General Electromagnetic Media, *IEEE MWCL.*, vol. 13, no.3, pp. 128-30 Mar 2003.
- Cummer S. A., Perfectly Matched Layer Behavior in Negative Refractive Index Materials, *IEEE AWPL.*, vol. 44, no.12, pp. 1630-9 Dec 2005.

- Eleftheriades G. V., K. G. Balmain, *Negative-Refractive Metamaterials*, IEEE Press, John Wiley and Sons, Hoboken, NJ, 2005.
- J.A. Bittencourt, Ed., *Fundamentals of Plasma Physics*. Brazil: Sao Jose dos Campos, SP, 1995.
- J. Fang, Generalized Perfectly Matched Layer-An Extension of Berenger's Perfectly Matched Layer Boundary Condition, *IEEE Microwave and Guided Wave Letters* vol. 5, no. 12, pp 451-453, December 1995.
- Fang J., Z. Wu, Closed form expression of numerical reflection coefficient at PML interfaces and optimization of PML performance, *IEEE Microwave and Guided Wave Letters* vol. 6, pp 332-334, Sept 1996.
- Ferguson, J. A., F. P. Snyder, D. G. Morfitt, and C. H. Shellman, Long-wave propagation capability and documentation, *Tech. Doc. 1518*, Naval Ocean Systems Center, San Diego, 1989.
- Gedney, S. G., An Anisotropic Perfectly Matched Layer-Absorbing Medium for the Truncation of FDTD Lattices, *IEEE Trans. Ant. Prop.*, vol. 44, no.12, pp. 1630-9 Dec 1996.
- Gedney, S. D., G. Liu, J. A. Roden, A.M. Zhu Perfectly matched layer media with CFS for an unconditionally stable ADI-FDTD method, *IEEE APS*, 49, No. 11, 1554-1559 (2001).
- Gendrin R., Le guidage des whistlers par le champ magnetique, *Planet. Space Sce.*, vol. 5, pp. 274-282, 1961.
- Hairer E., S. P. Nørsett, G. Wanner, *Solving Ordinary Differential Equations I: Nonstiff Problems*, Springer-Verlag New York Inc, New York, NY, 2000.
- Hairer E., S.P. Nørsett, G. Wanner, *Solving Ordinary Differential Equations II: Stiff and Differential-Algebraic Problems*, Springer-Verlag New York Inc, New York, NY, 2002.

- Helliwell R. A., *Whistlers and Related Ionospheric Phenomena*, Stanford Univ. Press, Stanford, CA, 1965.
- Johnson, M. P., U. S. Inan, and D. S. Lauben, Subionospheric vlf signatures of oblique (nonducted) whistler-induced precipitation, *Geophys. Res. Lett.*, 26, 3569, 1999.
- Kunz, K., R. Luebbers, *The Finite Difference Time Domain Method for Electromagnetics*. CRC Press, 1993.
- Kelley, D., R. Luebbers, Piecewise Linear Recursive Convolution for Dispersive Media using FDTD, *IEEE Trans. Ant. Prop.*, vol 44, no 6, pp 792-798, June 1996.
- Lee, J. H., and D. K. Kalluri, Three-Dimensional FDTD Simulation of Electromagnetic Wave Transformation in a Dynamic Inhomogeneous Magnetized Plasma, *IEEE Trans. Ant. Prop.*, vol. 47, no. 7, pp. 1146-51, Sept 1999.
- Ramadan, O., A. Y. Oztoprak DSP techniques for the implementation of perfectly matched layer for truncating FDTD domains , *Electronic Letters*, 38, No. 5, 211-212 (2002).
- Ratcliffe, J. A., *The Magneto-Ionic Theory and its Applications to the Ionosphere* Cambridge University Press, 1959.
- Roden, J. A., S. D. Gedney, Convolutional PML (CPML): An Efficient FDTD Implementation of the CFS-PML for Arbitrary Media, *Microwave and Optical Technology Letters*, 27, No. 5, 334-339 (2000).
- Sarto M. S., A. Scarlatti, Suppression of late-time instabilities in 3-D-FDTD analyses by combining digital filtering techniques and efficient boundary conditions, *IEEE Trans. Magnetics*, 37, 3273, 2001.
- Stratton, J. A., *Electromagnetic Theory*. NY and London: McGraw-Hill Book Co., 1941
- Taflove, A., Ed., *Finite Difference Time Domain Methods for Electrodynamical Analyses*. NY: Artech House, May 1995.

- Taflove, A., and S. C. Hagness, *Computational Electrodynamics: The Finite-Difference Time-Domain Method*, 2nd ed., Artech House, Norwood, MA, 2000.
- Teixeira, F. L., A General Approach to Extend Berenger's Absorbing Boundary Condition to Anisotropic and Dispersive Media, *IEEE Trans. Ant. Prop.*, vol. 46, no. 5, pp. 1386-7, Sept 1998.
- Thevenot M., J. P. Berenger, Th. Monediere, and F. Jecko, A FDTD Scheme for the computation of VLF-LF Propagation in the Anisotropic Earth-Ionosphere Waveguide, *Annals of Telecom.*, vol. 54, pp. 297-310, 1999.
- Veselago V. G., Electrodynamics of substances with simultaneous negative values of ϵ and μ , *Sov. Phys. Usp.*, vol. 10, pp.509, 1968.
- K. S. Yee, Numerical solution of initial boundary value problems involving Maxwell's equations in isotropic media, *IEEE Trans. Antennas Propagat.* pp.302-307, 1966.
- Zhao Y. J., K. L. Wu, and K. Cheng, A compact 2-D full-wave finite-difference frequency-domain method for general guided wave structures, *IEEE Trans. Microwave Theory Tech.*, vol. 50, pp. 1844-1848, July 2002.